Synthesis and characterization of AuM (M = Fe, Co, Ni) bimetallic nanoalloys electrocatalysts for the oxygen reduction reaction in alkaline fuel cells

Francisco Jaqueline Acosta Arreazola

THÈSE

Pour obtenir le grade de

DOCTEUR DE L'UNIVERSITE GRENOBLE ALPES

préparée dans le cadre d'une cotutelle entre l'*Université Grenoble Alpes* et l'Universidad Autónoma de Nuevo León

Spécialité : **Matériaux, Mécanique, Génie civil, Electrochimie**

Arrêté ministériel du 25 mai 2016

Présentée par

Francisco Jaqueline ACOSTA ARREAZOLA

Thèse dirigée par **Professor Marian CHATENET** et **Dr Nora Aleyda GARCÍA GÓMEZ**
codirigée par **Dr Israel Alejandro LÓPEZ HERNÁNDEZ**

préparée au sein des **Laboratoire d'électrochimie et de physicochimie des matériaux et des interfaces** et **Laboratorio de Materiales II : Almacenamiento y Conversión de Energía**

dans **les Écoles Doctorales : I-*MEP2*** - Ingénierie - Matériaux, Mécanique, Environnement, Energétique, Procédés, Production ; et **PSGC UANL –** Posgrado en Ciencias

Synthèse et caractérisation d'électrocatalyseurs de nanoalliages bimétalliques AuM (M = Fe, Co, Ni) pour la réaction de réduction de l'oxygène dans les piles à combustible alcalines

Thèse soutenue publiquement le **« 28 mars 2022 »**,
devant le jury composé de :

M. Marian CHATENET
Université Grenoble Alpes, Directeur de thèse
Mme. Nora Aleyda GARCÍA GÓMEZ
Universidad Autónoma de Nuevo León, Directeur de thèse
M. Christophe COUTANCEAU
Université de Poitiers, Rapporteur
M. Rodrigo MAYÉN MONDRAGÓN
Universidad Nacional Autónoma de México, Rapporteur
Mme. Muriel VERON
SIMAP – Grenoble INP, Examinatrice-Président
Mme. Margarita SÁNCHEZ DOMÍNGUEZ
Centro de Investigación en Materiales Avanzados, Examinatrice
M. Eduardo Maximiano SANCHEZ CERVANTES
Universidad Autónoma de Nuevo León, Membre
Mme. Salomé Maribel DE LA PARRA ARCINIEGA
Universidad Autónoma de Nuevo León, Membre

ACKNOWLEDGMENT

This work was carried out thanks to the support of the National Council of Science and Technology (CONACyT) through the project SEP-CONACYT 236812, and the financial scholarship granted to me (CVU: 781349).

I thank the Facultad de Ciencias Químicas (FCQ, UANL) and the Laboratoire d'Électrochimie et de Physicochimie des Matériaux et des Interfaces (LEPMI) for the infrastructure provided to carry out this project.

I thank “La Fondation Grenoble INP” for the financial scholarship granted to me during the COVID-19 pandemic.

I would like to begin by thanking my thesis director, Dr Nora A. García Gómez for always trust, and support me. You have given to me the opportunity to get involved in different aspects of scientific research. You have given to me advice when needed, and experiences that helped me in my professional and personal development. Thank you for these six years of work, you have become someone in my family.

To my thesis director, Professor Marin Chatenet, thank you for responding to my email that October 2018, and having trusted in this project, and me, since the beginning. I would like to tell you that I greatly enjoyed the time I spent working with you and your team at LEPMI. It was a time of great professional and personal growth.

To my thesis co-advisor Dr Israel López, and tutorial committee Professor Eduardo Sánchez, Dr Salomé de la Parra, and Dr Rubí Hernández for accompanying me on this path with their invaluable contributions to my project, always with the aim of enriching it.

My greatest thank is to my family. You have always been by my side, have never let go of my hand, despite the difficulties.

Mom, you are the most important person in my life, and I thank God for having given me such a special angel like you. Thank you for always being there for me and giving me your unconditional support every step of the way. You are the engine that gives meaning to my life. Thank you for teaching me what true love is. I love you Mama.

To my dad, from whom I have learned more in life, my best teacher, an example to follow. Thank you for all your advice and lessons, thank you for making me the person I am, thank you for instilling your values in me. I love you Papa.

Thank God for having given me such a precious gift as life is and teaching me that no matter how difficult the road is, if we accompany each other for your infinite mercy, everything is better.

ABSTRACT

Francisco Jaqueline Acosta Arreazola **Date of graduation:** March, 2021

Universidad Autónoma de Nuevo León, Facultad de Ciencias Químicas

Communauté Université Grenoble Alpes, École Doctorale I-MEP2

Subject: "Synthesis and characterization of AuM (M = Fe, Co, Ni) bimetallic nanoalloys electrocatalysts for the oxygen reduction reaction in alkaline fuel cells"

Pages: 92

Candidate for the degree of Doctor of Sciences Mayor Materials Chemistry

Candidate for the degree of Doctor with specialty in Materials, Mechanics, Civil Engineering and Electrochemistry (2MGE)

Study area: Materials chemistry and Electrochemistry

Purpose and Method of the Study:

Fuel cells have become a viable alternative towards generating clean energy and reducing the use of fossil fuels. However, there is still a long way to go to commercialize them. One of the main bottlenecks is the Oxygen Reduction Reaction, ORR, the reaction that takes place at the cathode of the cell and is generally carried out at low reaction rates. To make the previous reaction more efficient, the electrodes are made of electrocatalyst materials. To date, the main electrocatalyst used for many redox reactions is platinum (Pt); however, Pt is limited in the Earth's crust, so its price is high. Furthermore, it has recently been shown that platinum, when used as carbon-supported nanoparticles, is very unstable in alkaline environment. This is why it is necessary to develop new electrocatalyst materials that can carry out the oxygen reduction reaction, that are chemically stable in the reaction electrolyte.

The present work proposes the preparation, characterization, and application as electrocatalysts of ORR, bimetallic nanoalloys:

- AuFe
- AuCo
- AuNi

supported onto carbon.

The proposed systems were prepared via four methodologies:

- Ethylene glycol stabilization
- Aqueous solution stirring at ambient temperature
- Hydrothermal
- Reverse micelle microemulsion

Characterization techniques were:

- X-ray diffraction (XRD)
- Inductively coupled plasma – mass spectroscopy (ICP-MS)
- Transmission electron microscopy (TEM)
- X-ray Energy dispersive spectroscopy (X-EDS)
- X-ray photoelectron spectroscopy (XPS)

Electrochemical and electrocatalytic activities were evaluated with:

- Lineal voltammetry
- Rotating disk technique
- Rotating ring-disk electrode technique (some cases)

Furthermore, accelerated degradation tests (ADT) were performed to evaluate the stability of the prepared materials in close-to-real operation.

Contributions and Conclusions:

Ethylene glycol method allowed to obtain Au:Co and Au:Ni nanoalloys. It was demonstrated by X-ray diffraction, where a slight shift of the main diffraction signal towards larger angles was observed due to the contraction of the interplanar distance of gold because of the insertion of smaller atoms. The conditions used in the present work, however, were not ideal since by not adjusting the pH to basic values, the formation of Co and Ni ethylene-glycoxides was not allowed, species that facilitate the reduction of metals; furthermore, at the working pH, the decomposition of the reducing agent, $NaBH_4$, can

occur. Through Vegard's Law calculations, it was estimated that the amounts of Co and Ni alloyed with Au were lower than those theoretically expected; the above was verified by ICP-MS, via determination of the real content of the three metals in the materials. With transmission electron microscopy, it was observed that, by increasing the volume of the precursor solutions of Co and Ni, the particle size decreased, this because the concentration of Au decreased. Additionally, XPS confirmed the formation of the Au:Ni/C 94:6 nanoalloy since the peaks corresponding to Au $4f_{5/2}$ and Au $4f_{7/2}$ core levels shifted towards lower binding energies compared to the pure Au prepared in this work. Considering these series of materials, ORR activities were determined; the best result was obtained with Au:Ni/C 94:6, since high onset potential for ORR (0.833 V vs. RHE) and half-wave potential (0.606 V vs. R) were measured.

Subsequently, the characterization of nanoalloys Au:Fe, Au:Co, and Au:Ni prepared by the stirring method in aqueous medium at room temperature was continued. As expected, by adjusting the pH of the solution to 10, the precipitation of transition metal hydroxides was observed. By X-ray diffraction, it was corroborated that the main diffraction signals shifted towards greater angles in 2θ, the above indicates the alloy between metals. This displacement occurred in a greater way for Au:Co and Au:Ni than for Au:Fe, this phenomena can be explained since Au, Co, and Ni share the same face-centered cubic crystal structure (FCC), while Fe has a body-centered cubic crystal structure (BCC). The presence of oxidized phases of transition metals such as Fe_2O_3 Maghemite, β-$Co(OH)_2$, and $Ni(OH)_2$ was also corroborated. Through calculations with Vegard's Law, it was estimated that the molar percentages of Co and Ni were 0.85% and 0.46%, respectively. TEM and X-EDS techniques allowed to observe that particles obtained by the stirring method were smaller and less agglomerated than those obtained by the ethylene glycol method. However, the atomic distribution was not homogeneous: Au-rich, Co-rich, and Ni-rich zones were observed. Regarding the electrochemical performance, the best electrocatalyst was Au:Ni/C (0.46 molar percentage of Ni) since its onset potential and half-wave potential for ORR were 0.839 V vs. RHE and 0.643 V vs. RHE, respectively.

By observing that aqueous medium allowed to obtain smaller and less agglomerated particles, it was decided to perform the characterization of Au:Fe, Au:Co, and Au:Ni prepared by hydrothermal method. With X-ray diffraction it was observed that the main

diffraction peak of Au shifted towards greater angles in 2θ (proving that Au alloyed with the transition metals), and the presence of oxidized phases of transition metals (Fe_2O_3 Maghemite, β-$Co(OH)_2$, and $Ni(OH)_2$). One interesting phenomenon observed by XRD was that Au diffraction signals decreased in intensity, pointing to a decrease of its crystallinity due to the alloy with the transition metals. With Vegard's Law calculations, it was estimated that molar percentages of Fe, Co, and Ni were 0.04%, 0.49%, and 0.84%, respectively. Again, it was observed that Co and Ni were incorporated in greater proportion than Fe because of the difference in their crystalline structure. As expected, the particle sizes of Au:Co and Au:Ni were smaller compared with the two previous methods, the aforesaid corroborated by TEM. Elemental analysis by X-EDS evidenced the formation of Au-rich, Co-rich, and Ni-rich zones. With XPS, it was observed the negative shift in the binding energies of the Au $4f_{5/2}$ and Au 4 $f_{7/2}$ core levels of Au after alloying it with Fe, Co, and Ni. It has been proven that the above shift produces a change in the center of the d-band concerning the Fermi Level, which favors the adsorption of O_2 on the Au surface, thus increasing its performance as an electrocatalyst of the oxygen reduction reaction. The rotating ring-disk electrode technique allowed to demonstrate that, by alloying Au with metals such as Fe, Co, and Ni by hydrothermal method, its electrocatalytic activity for the ORR increases in alkaline electrolyte, thus fulfilling the hypothesis of this work. The best result was obtained with Au:Ni/C (0.9 molar percentage of Ni), whose onset and half-wave potentials were 0.874 V vs. RHE and 0.663 V vs. RHE, respectively.

Keeping in mind that Au:Ni nanoalloy showed the best electrocatalytic results, it was attempted to look for a way to improve its morphological and structural characteristics. For that reason, carbon-supported Au:Ni nanoalloy was prepared by reverse micelle microemulsion, followed by heat treatment in reducing atmosphere. X-ray diffraction and X-ray photoelectron spectroscopy proved that metals were in alloy form, due to phenomena described in the previous paragraphs. Atomic percentages of Ni were estimated with Vegard’s Law calculations to be 1.2% and 1.3%, respectively before and after the heat treatment; this decrease in Ni content suggests an increase in the long-range order of Au due to heat and reducing conditions. After the heat treatment, the particles suffered a sintering process, which is why their size increased from 4 nm to 5 nm. The half-wave

potential for ORR was more positive after heat treatment, indicating that increasing crystallinity and particle size favor charge-transfer reaction kinetics by decreasing grain boundaries.

RESUMEN

Francisco Jaqueline Acosta Arreazola **Fecha de graduación:** Marzo 2021

Universidad Autónoma de Nuevo León, Facultad de Ciencias Químicas

Communauté Université Grenoble Alpes, École Doctorale I-MEP2

Tesis: "Synthesis and characterization of AuM (M = Fe, Co, Ni) bimetallic nanoalloys electrocatalysts for the oxygen reduction reaction in alkaline fuel cells"

Páginas: 92

Candidato para el grado de Doctor en Ciencias con Orientación en Química de los Materiales

Candidato para el grado de Doctor con especialidad en Materiales, Mecánica, Ingeniería Civil y Electroquímica (2MGE)

Área de estudio: Química de los materiales, y Electroquímica

Propósito y método de estudio:

Las celdas de combustible se han convertido en una alternativa viable hacia la generación de energía limpia, y la disminución del uso de combustibles fósiles. Sin embargo, aún hay un amplio camino que recorrer para su comercialización. Uno de los principales retos es la Reacción de Reducción de Oxígeno, ORR por sus siglas en inglés, reacción que se lleva a cabo en el cátodo de la celda, y que generalmente se lleva a cabo a velocidades de reacción bajas. Con el fin de eficientizar la reacción anterior, los electrodos están compuestos por materiales electrocatalizadores. A la fecha, el principal electrocatalizador utilizado para un gran número de reacciones redox es el platino, Pt, sin embargo, este se encuentra limitado en la corteza terrestre por lo que su precio es elevado; además, recientemente se ha demostrado que cuando el platino soportado cobre C es muy inestable en medio alcalino, por lo que es necesario el desarrollo de nuevos materiales electrocatalizadores que puedan llevar a cabo la reacción de reducción de oxígeno, y que sean estables químicamente en el electrolito.

En el presente trabajo se propone la preparación, caracterización, y aplicación como electrocatalizadores de la ORR, nanoaleaciones bimetálicas:

- AuFe

- AuCo
- AuNi

soportadas sobre carbón.

Los sistemas propuestos fueron sintetizados por cuatro métodos de síntesis:

- Estabilización con etilenglicol
- Agitación en medio acuoso a temperatura ambiente
- Método hidrotérmico
- Microemulsión por micelas inversas

Las técnicas de caracterización utilizadas fueron:

- Difracción de rayos X (XRD)
- Espectrometría de masas con plasma acoplado inductivamente (ICP-MS)
- Microscopía electrónica de transmisión (TEM)
- Espectroscopia de energías dispersivas de rayos X (X-EDS)
- Espectroscopia fotoelectrónica de rayos X (XPS)

Las actividades electroquímica y electrocatalítica fueron evaluadas por:

- Voltamperometría cíclica
- Electrodo de disco rotatorio
- Electrodo de disco-anillo rotatorio (en unos casos)

Adicionalmente se realizaron pruebas de degradación aceleradas (ADT) para observar la posible aplicación real de los materiales.

Conclusiones y contribuciones:

El método de etilenglicol permitió la obtención de nanoaleaciones Au:Co y Au:Ni. Lo anterior fue demostrado mediante difracción de rayos X, en donde se observó un ligero corrimiento de la señal de difracción principal hacia ángulos mayores debido a la contracción de la distancia interplanar del oro debido a la inserción de átomos más pequeños. Las condiciones utilizadas en el presente trabajo, sin embargo, no fuero las ideales ya que al no ajustar el pH a valores básicos no se permitió la formación de

etilenglicóxidos de los metales de transición, especies que facilitan la reducción de dicho metal; además, al pH de trabajo puede ocurrir la descomposición del agente reductor $NABH_4$. Mediante cálculos con la Ley de Vegard, se estimó que el contenido de Co y Ni en aleación con Au era más bajo que el esperado teóricamente, esto se comprobó mediante ICP-MS, técnica con la cual se determinó el contenido real de los tres metales. Con microscopia electrónica de transmisión se observó que al incrementar el volumen de las soluciones precursoras de Co y Ni disminuía el tamaño de partícula, esto debido a la disminución de la concentración del Au. De esta serie de materiales, el mejor resultado fue obtenido con Au:Ni/C 94:6 ya que el potencial de inicio para la ORR fue de 0.833 V vs. RHE y el potencial de media onda fue de 0.606 V vs. RHE. Adicionalmente, la técnica de XPS corroboró la formación de la nanoaleación Au:Ni/C 94:6 ya que los picos correspondientes a los niveles Au $4f_{5/2}$ y Au $4f_{7/2}$ se desplazaron hacia energías de enlace menores con respecto al Au puro preparado en este trabajo.

Posteriormente se realizó la caracterización de nanoaleaciones Au:Fe, Au:Co, y Au:Ni preparadas por el método de agitación en medio acuoso a temperatura ambiente. Como era de esperarse, al ajustar el pH de la solución a 10 se observó la precipitación de hidróxidos de los metales de transición. Por difracción de rayos X se corroboró el desplazamiento de las señales de difracción hacia ángulos mayores en 2θ, lo que indica la aleación de los metales. Dicho desplazamiento se dio en mayor proporción para Au:Co y Au:Ni que para Au:Fe, lo anterior puede ser explicado ya que Au, Co, y Ni comparten la misma estructura cristalina cúbica centrada en las caras (FCC), mientras que Fe tiene una estructura cristalina cúbica centrada en el cuerpo (BCC). También se corroboró la presencia de fases oxidadas de los metales de transición como Fe_2O_3 Maghemita, β-$Co(OH)_2$ y $Ni(OH)_2$. Mediante cálculos con la Ley de Vegard se estimó que los porcentajes molares de Co y Ni fueron de 0.85 % y 0.46 %, respectivamente. TEM y X-EDS permitieron observar que las partículas obtenidas por el método de agitación fueron de menor tamaño y menor aglomeración que las obtenidas por el método de etilenglicol, sin embargo, con distribución atómica no homogénea, ya que se observaron zonas ricas en Au y zonas ricas en Co o Ni. Con respecto al desempeño electroquímico, el mejor electrocatalizador fue Au:Ni/C (0.46 % molar de Ni) ya que sus potencial de inicio y potencial de media onda para la ORR fueron de 0.839 V vs. RHE y 0.643 V vs. RHE, respectivamente.

Al observar que realizando la síntesis en medio acuoso el tamaño de partícula disminuyó, se decidió realizar la caracterización de Au:Fe, Au:Co, y Au:Ni preparados mediante método hidrotérmico. Por difracción de rayos X se corroboraron los mismos dos fenómenos observados en el método de agitación, ya que la señal de difracción principal del oro se desplazó hacia ángulos mayores en 2θ (evidenciando la aleación del Au con los metales de transición), y se observó la presencia de fases oxidadas de los metales de transición (Fe_2O_3 Maghemita, β-$Co(OH)_2$, y $Ni(OH)_2$). Otro fenómeno interesante observado por XRD fue la disminución en la intensidad de las señales de difracción del Au debido a la disminución de su cristalinidad por la aleación con los metales de transición. Mediante cálculos con la Ley de Vegard se estimó que los porcentajes molares de Fe, Co, y Ni fueron de 0.04 %, 0.49 %, y 0.84 %, respectivamente. Nuevamente se observa que el Fe se incorpora en menor proporción que el Co y Ni debido a la diferencia en su estructura cristalina. Los tamaños de partícula de Au:Co y Au:Ni fueron menores con respecto a los métodos de etilenglicol y agitación en medio acuoso, lo anterior corroborado por TEM. El análisis elemental por X-EDS evidenció la formación de zonas ricas en Au, y zonas ricas en Co o Ni, estas últimas probablemente compuestas por β-$Co(OH)_2$ o $Ni(OH)_2$, respectivamente. Mediante XPS se observó el corrimiento negativo de las energías de enlace de los niveles Au $4f_{5/2}$ y Au 4 $f_{7/2}$ del Au después de la aleación con Fe, Co, y Ni; está comprobado que dicho corrimiento produce un cambio en el centro de banda-d con respecto al Nivel de Fermi, lo que favorece la adsorción de O_2 sobre la superficie del Au, incrementando así su desempeño como electrocatalizador de la reacción de reducción de oxígeno. La técnica del electrodo de anillo-disco rotatorio permitió demostrar que, aleando Au con metales como Fe, Co, y Ni por método hidrotérmico, se incrementa su actividad electrocatalítica frente a la reacción de reducción de oxígeno en electrolito alcalino, cumpliéndose así la hipótesis de este trabajo. El mejor resultado fue obtenido con Au:Ni/C (0.9 % molar de Ni) cuyos potenciales de inicio y media onda fueron 0.874 V vs. RHE y 0.663 V vs. RHE, respectivamente.

Teniendo en mente que la aleación Au:Ni presentó los mejores resultados electrocatalíticos, y con el fin de mejorar sus características morfológicas y estructurales, dicho material se preparó por el método de microemulsión con micelas inversas, seguido de un tratamiento térmico en atmósfera reductora. La difracción de rayos X y la espectroscopia fotoelectrónica de rayos X, evidenciaron la aleación de los metales debido a los fenómenos

descritos en los párrafos anteriores. Las estimaciones del porcentaje atómico Ni, antes y después del tratamiento térmico, por medio de la Ley de Vegard, fueron de 1.2 % y 1.3 %, respectivamente, este decremento en el contenido de Ni sugiere un incremento en el orden de largo alcance del Au debido a la temperatura y las condiciones reductoras. Posterior al tratamiento térmico, las partículas sufrieron un proceso de sinterizado, razón por la cual su tamaño incrementó de 4 nm a 5 nm. El potencial de media onda para la ORR es más positivo luego del tratamiento térmico, indicando que los incrementos en la cristalinidad y el tamaño de partícula favorecen la cinética de la reacción y la transferencia de los portadores de carga al disminuir las fronteras de grano.

RÉSUMÉ

Francisco Jaqueline Acosta Arreazola

Date de l'obtention du diplôme : Décembre 2021

Universidad Autónoma de Nuevo León, Facultad de Ciencias Químicas

Communauté Université Grenoble Alpes, École Doctorale I-MEP2

Sujet: "Synthesis and characterization of AuM (M = Fe, Co, Ni) bimetallic nanoalloys electrocatalysts for the oxygen reduction reaction in alkaline fuel cells"

Pages: 92

Candidat au grade de Docteur ès Sciences Majeure Chimie des Matériaux

Candidat au grade de Docteur de l'Université Grenoble-Alpes, spécialité Matériaux, Mécanique, Génie Civil, Electrochimie (2MGE)

Domaine d'étude : Chimie des matériaux et électrochimie

But et méthode de l'étude :

Les piles à combustible sont devenues une alternative viable pour générer de l'énergie propre et réduire l'utilisation de combustibles fossiles. Cependant, il reste encore un long chemin à parcourir pour les commercialiser. L'un des principaux défis est la réaction de réduction de l'oxygène, ORR, une réaction qui a lieu à la cathode de la cellule et dont la cinétique de réaction est lente. Afin d'accélérer cette réaction et la rendre plus efficace, les électrodes doivent employer des matériaux électrocatalyseurs. A ce jour, le principal électrocatalyseur utilisé pour un grand nombre de réactions redox (et en particulier l'ORR) est le platine (Pt), cependant, celui-ci est limité dans la croûte terrestre donc son prix est élevé. Par ailleurs, il a été récemment montré que le platine est très instable en milieu alcalin lorsqu'il est nanostructuré et supporté sur carbone ; c'est pourquoi il est nécessaire de développer de nouveaux matériaux électrocatalyseurs capables de réaliser la réaction de réduction de l'oxygène, qui soient (électro)chimiquement stables dans le milieu réactionnel.

Le présent travail propose d'œuvrer en ce sens et concerne la préparation, la caractérisation et l'application comme électrocatalyseurs d'ORR, de nanoalliages bimétalliques à base d'or supporté par le carbone :

- AuFe

- AuCo
- AuNi

Les systèmes proposés ont été synthétisés par quatre méthodes de synthèse :

- Stabilisation à l'éthylène glycol
- Agitation en milieu aqueux à température ambiante
- Hydrothermale
- Microémulsion par micelles inverses

Les techniques de caractérisation utilisées étaient :

- Diffraction des rayons X (XRD)
- Spectrométrie de masse à plasma à couplage inductif (ICP-MS)
- Microscopie électronique à transmission (MET)
- Spectroscopie à rayons X à dispersion d'énergie (X-EDS)
- Spectroscopie photoélectronique aux rayons X (XPS)

Les activités électrochimiques et électrocatalytiques ont été évaluées par :

- Voltamétrie cyclique
- Electrode tournante à disque
- Electrode tournante disque-anneau (dans certains cas)

De plus, des tests de dégradation accélérée (ADT) ont été réalisés pour observer la stabilité des matériaux en conditions proches de celle de leur utilisation réelle.

Conclusions et contributions :

La méthode à l'éthylène glycol a permis d'obtenir des nanoalliages Au:Co et Au:Ni. Cela a été démontré par diffraction des rayons X, où un léger décalage du signal de diffraction principal vers des angles plus grands a été observé (par rapport au signal de Au) en raison de la contraction de la distance interplanaire de l'or due à l'insertion d'atomes plus petits. Les conditions utilisées dans le présent travail n'étaient cependant pas idéales puisqu'en n'ajustant pas le pH à des valeurs basiques, la formation d'éthylène glycoxydes des métaux de transition n'était pas favorisée, ces espèces facilitant la réduction dudit métal. De plus, au

pH de travail, la décomposition de l'agent réducteur $NaBH_4$ peut se produire. Grâce à des calculs avec la loi de Vegard, il a été estimé que la teneur en Co et Ni dans l'alliage avec Au était inférieure à ce qui était théoriquement attendu, ce qui a été vérifié par ICP-MS, une technique avec laquelle la teneur réelle des trois métaux a été déterminée. En microscopie électronique à transmission il a été observé qu'en augmentant le volume des solutions précurseurs de Co et Ni, la taille des particules diminuait, ceci en raison de la diminution de la concentration en Au. De plus, la technique XPS a corroboré la formation du nano-alliage Au:Ni/C 94:6 puisque les pics correspondant aux niveaux Au $4f_{5/2}$ et Au $4f_{7/2}$ se sont déplacés vers des énergies de liaison plus faibles par rapport à l'Au pur préparé dans ce travail. De cette série de matériaux, le meilleur résultat a été obtenu avec Au:Ni/C 94:6 puisque le potentiel de départ pour l'ORR était de 0,833 V vs. RHE et le potentiel demi-onde était de 0,606 V vs. RHE.

Par la suite, la caractérisation des nanoalliages Au:Fe, Au:Co et Au:Ni préparés par la méthode d'agitation en milieu aqueux à température ambiante a été poursuivie. Comme attendu, en ajustant le pH de la solution à 10, la précipitation d'hydroxydes de métaux de transition a été observée. Par diffraction des rayons X, le déplacement des signaux de diffraction vers des angles supérieurs en 2θ a été corroboré, ce qui indique l'alliage des métaux. Ce déplacement s'est produit dans une plus grande proportion pour Au:Co et Au:Ni que pour Au:Fe, ce qui peut s'expliquer par le fait que Au, Co et Ni partagent la même structure cristalline cubique à faces centrées (FCC), tandis que Fe a une structure cristalline cubique centrée (BCC). La présence de phases oxydées de métaux de transition tels que Fe_2O_3 Maghémite, β-$Co(OH)_2$ et $Ni(OH)_2$ a également été corroborée. Par des calculs avec la loi de Vegard, il a été estimé que les pourcentages molaires de Co et Ni étaient respectivement de 0,85% et 0,46%. Le MET et l'X-EDS nous ont permis d'observer que les particules obtenues par la méthode par agitation étaient plus petites et moins agglomérées que celles obtenues par la méthode à l'éthylène glycol, avec cependant une distribution atomique inhomogène, puisque des zones riches en Au et des zones riches en Co ou Ni. Concernant les performances électrochimiques, le meilleur électrocatalyseur était Au:Ni/C (0,46% molaire Ni) puisque son potentiel de départ et son potentiel demi-vague pour l'ORR étaient de 0,839 V vs. RHE et 0,643 V vs. RHE, respectivement.

En observant qu'en travaillant en milieu aqueux il y avait une diminution de la taille des particules, il a été décidé d'effectuer la caractérisation de Au:Fe, Au:Co et Au:Ni préparés par méthode hydrothermale. Par diffraction des rayons X, les deux mêmes phénomènes observés dans la méthode d'agitation ont été corroborés: le signal principal de diffraction de l'or s'est déplacé vers des angles supérieurs en 2θ (montrant l'alliage d'Au avec les métaux de transition), et la présence de phases oxydées de métaux de transition (Fe_2O_3 Maghémite, β-$Co(OH)_2$ et $Ni(OH)_2$). Un autre phénomène intéressant observé par XRD était la diminution de l'intensité des signaux de diffraction de l'Au due à la diminution de sa cristallinité, due à l'alliage avec les métaux de transition. Grâce à des calculs avec la loi de Vegard, il a été estimé que les pourcentages molaires de Fe, Co et Ni étaient respectivement de 0,04%, 0,49% et 0,84%. Encore une fois, on observe que Fe est celui qui est incorporé dans une proportion plus faible que Co et Ni en raison de la différence de leur structure cristalline. Comme prévu, les tailles de particules de Au:Co et Au:Ni étaient plus petites par rapport aux deux méthodes précédentes, ce qui a été corroboré par MET. L'analyse élémentaire par X-EDS a de nouveau mis en évidence la formation de zones riches en Au, et de zones riches en Co ou Ni, ces dernières probablement composées de β-$Co(OH)_2$ ou $Ni(OH)_2$, respectivement. En XPS, le décalage négatif des énergies de liaison des niveaux Au $4f_{5/2}$ et Au 4 $f_{7/2}$ d'Au a été observé pour alliage avec Fe, Co et Ni ; ce décalage produit un changement du centre de la bande d par rapport au niveau de Fermi, ce qui favorise l'adsorption d'O_2 sur la surface de Au, augmentant ainsi ses performances en tant qu'électrocatalyseur de la réaction de réduction de l'oxygène. La technique de l'électrode à disque tournant a permis de démontrer qu'en alliant Au avec des métaux tels que Fe, Co et Ni par la méthode hydrothermale, son activité électrocatalytique augmente vis-à-vis de la réaction de réduction de l'oxygène dans l'électrolyte alcalin, confirmant ainsi l'hypothèse initiale de ce travail. Le meilleur résultat a été obtenu avec Au:Ni/C (0,9% molaire Ni) dont les potentiels initial et demi-vague étaient de 0,874 V vs. RHE et 0,663 V vs. RHE, respectivement.

Sachant que l'alliage Au:Ni présentait les meilleurs résultats électrocatalytiques, une voie a été recherchée pour améliorer ses caractéristiques morphologiques et structurelles, pour laquelle ledit matériau a été préparé par la méthode de la microémulsion avec des micelles inverses, suivie d'un traitement thermique sous atmosphère réductrice. La diffraction des

rayons X et la spectroscopie photoélectronique des rayons X ont montré l'alliage des métaux dû aux phénomènes décrits dans les paragraphes précédents. Les estimations du pourcentage atomique de Ni, avant et après traitement thermique, par la loi de Vegard étaient respectivement de 1,2% et 1,3%, cette diminution de la teneur en Ni suggère une augmentation de l'ordre à longue distance de l'Au, due au traitement thermique. Après le traitement thermique, les particules ont subi un processus de frittage, c'est pourquoi leur taille est passée de 4 nm à 5 nm. Le potentiel de demi-vague pour l'ORR est plus positif après traitement thermique, indiquant que l'augmentation de la cristallinité et de la taille des particules favorise la cinétique de réaction de transfert de charge en diminuant les joints de grains.

TABLE OF CONTENTS

LIST OF FIGURES

LIST OF TABLES

LIST OF EQUATIONS

CHAPTER 1: INTRODUCTION AND BACKGROUND

INTRODUCTION

The International Energy Agency (IEA), in 2017, published its global energy perspective[1] and predicted that the world population would increase from 7.4 billion in 2016 to 9.1 billion people by 2040. One year later, in 2018, the IEA published its World Energy Outlook[2] and examined trends of how the global energy system needs to change, from growing electrification to the expansion of renewables sources, globalization of natural gas markets, etc.

The excessive use of fossil fuels has generated significant environmental problems. Although developed countries have energy policies and have obtained positive results, the biggest challenge for the coming years is their implementation on a large scale and move from a fossil fuels energy system to a sustainable energy model based on renewable energy sources[3].

Fuel cells are electrochemical devices that directly convert the chemical energy of a fuel to electrical energy. When the fuel is hydrogen, the only reaction products are electricity, water, and heat [4]. These devices have anodic and cathodic electrodes, which are separated by a selective membrane that allows the transfer of ions. At the anode, hydrogen is oxidized to produce electrons and protons (Equation 1) that are transferred to the cathode through an external circuit and the membrane, respectively. At the cathode, oxygen reacts with the protons to be reduced and to form water (Equation 2).

$$H_2 \rightarrow 2H^+ + 2e^-$$ Equation 1

$$\frac{1}{2}O_2 + 2H^+ + 2e^- \rightarrow H_2O$$ Equation 2

The theoretical voltage of the general reaction is 1.23 V. In a fuel cell, the apparent voltage comes from the difference of the thermodynamic potential at the two electrodes, each of them being altered by the activation overpotential, the ohmic overpotential and the mass-transport overpotential. The thermodynamic potential is governed by the Nernst equation. The activation potential depends on the electrode kinetics (current flow) and the overpotential associated with the catalyst intrinsic activity (slow mainly for the oxygen reduction reaction, ORR). The accessibility to reactants (mass-transfer) drives the mass-transport overpotential. Finally, the ohmic overpotential is governed by the insufficient conductivity of the electrolyte membrane, but also to the contacts resistances and bulk conductivities between/of the electrode and current collector materials.

In a proton exchange membrane fuel cell (PEMFC), the overpotential for the ORR represents a loss of up to 20% of the theoretical maximum efficiency for hydrogen/air fuel cells. The kinetic limitation in the ORR represents another problem for the fuel cells operating at low temperatures, generally lower than 100°C because the rate of breaking the O=O bond to form water depends strongly on their interaction with the active adsorption sites of the electrocatalyst[5]. At present, the main electrocatalyst used to carry out this reaction is platinum supported on carbon as nanoparticles. The platinum catalyst can be poisoned during fuel cell operation (either by air impurities or if H_2

comes from reformate) and is, of course, a rare, expensive, and poorly-available material.

Unlike in PEMFCs, electrocatalysts with less or no platinum content can be used in alkaline fuel cells (AFC), owing, among others, to the fact that electrocatalysts usually show enhanced (electro)chemical stability in this environment[6-7]. Additionally, alkaline conditions also improve the kinetics of ORR, because the adsorption energy of spectator anions is lower when the pH increases, resulting in activation overpotential decreases[8].

An interesting strategy to increase the stability and activity of electrocatalysts is the synthesis of alloys at a nanometric scale [9]. These materials have a high surface area and, in most cases, the combination of electronic properties of their components generates a positive synergistic effect for catalysis.

The aim of this project is to obtain non-platinum-based ORR catalysts that can be used at the cathode of alkaline fuel cells; the targeted materials are gold-based bimetallic nanoalloys supported in a carbon structure.

BACKGROUND

A noble metal can be alloyed with some no-noble transition metal, regardless of its texture. Nevertheless, one usually witnesses an increase in its catalytic activity when the above is carried out at a nanometric scale, and this has been practically demonstrated for several reactions; the oxygen electrode reactions are typical examples where great catalytic enhancements have been observed.

An alloy is a combination of two or more metals. It may be either a solid solution of metal elements with characteristics of a single or partial phase, or a segregated solid solution with two or more phases[10]. Nanoalloys (NA) differ from bulk alloys in several significant aspects in terms of mixing patterns and geometric shapes[11]. Nanoalloys can be classified according to their mixing pattern, as described in Figure 1.

a) Completely phase-segregated NA, where the different phases share either an extended interface or a very limited number of heterometal bonds.
b) Mixed NA with chemical ordered or random structures.
c) Core-shell NA with single or multiple shell structures.

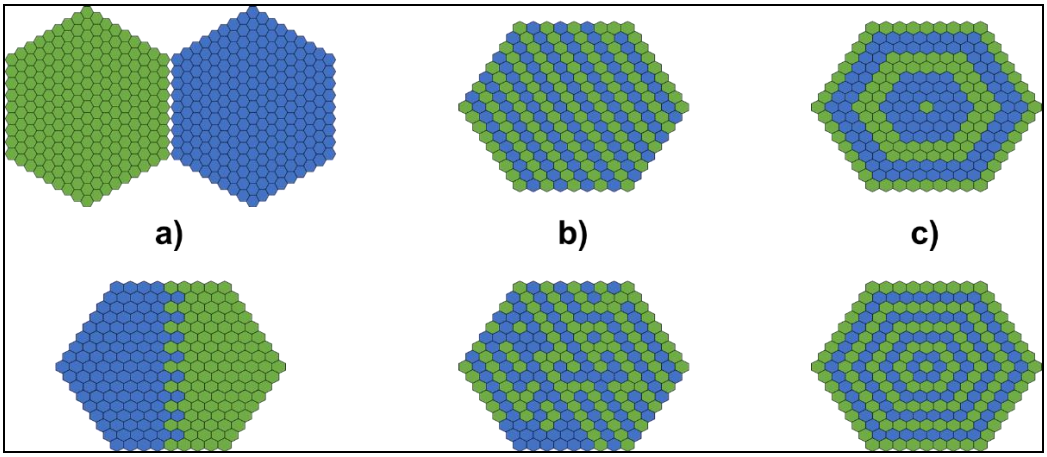

Figure 1. Schematic illustration of NAs for binary systems

The level of segregation, mixing, and atomic ordering depends on several factors. Those include the relative forces of homoatomic versus heteroatomic bonds, surface energies, differences in atomic size, charge transfer between metals and binding forces of supports.

The heterogeneous noble-metal-based electrocatalysts exhibit superior performances as compared to the non-noble-metal-based ones in electrochemical reactions in terms of activity and durability[12].

Based on thermodynamic aspects, Bard and collaborators proposed guidelines for the design of multimetal systems with application in ORR[13].

The mechanism for ORR is complicated and involves certain intermediate species. In a fuel cell, the direct 4-electron reduction pathway is desirable. It starts with a dissociative chemisorption that involves the breaking of the O=O bond to produce adsorbed oxygen atoms (O •), as shown in equation 3.

$$2M + O_2 \rightarrow 2MO$$ Equation 3

After that, adsorbed oxygen atoms are reduced to water (equation 4), via a series of elementary steps. It can be considered as the metal direct oxidation, followed by the oxide reduction.

$$2MO + 4H^+ + 4e^- \rightarrow 2M + 2H_2O$$ Equation 4

Figure 2 presents the Gibbs free energy data for equation 3 (oxygen chemisorption) against the standard reduction potential for equation 4 for several metals/metal oxides in 2^+ oxidation state.

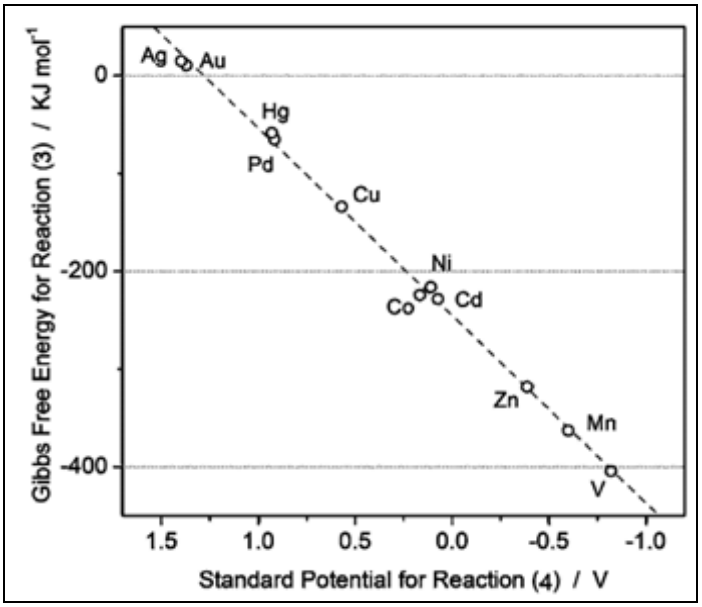

Figure 2. Graph of Gibbs free energy for equation 3 against the standard reduction potential for equation 4

Figure 2 shows that metals found in the lower right corner stabilize the M-O bond (equation 3) too strongly, so the overpotential to carry out the ORR (equation 4) increases, shifting the electrode potential to more negative values. On the other hand, for the metals in the upper left, reaction 3 is not favorable and the M-O bond is not stable. Because of this, even if the reaction 4 is favored thermodynamically, giving a more

positive reduction potential, the overall process is limited by the inexistence of MO species. In practice, a good catalyst should favor fast MO formation but also fast MO reduction into water, which is of course a matter of compromise, known as the Sabatier[92]. This usually leads to so-called Volcano plots.

To optimize this compromise, Bard and collaborators proposed to combine a metal that favors the breaking of the O=O bond (equation 3), with a second metal that is more efficient to carry out the reduction of the chemisorbed oxygen (equation 4), a strategy that was later demonstrated by Rodriguez and Koper for the example of $AuCu_3$ alloys[93].

The increase in the catalytic activity of many alloys can be explained by the d-band center modifications in the metals that is induced their alloying[14-17]. The essential of this theory is that the binding energy of an adsorbate to a metal surface is strongly influenced by the electronic structure of the surface[18].

When a molecule such as O_2 is chemisorbed onto a platinum surface, and according with the Molecular Orbital theory, the metal d-band hybridizes with the bonding (σ) orbital of the adsorbate to form a filled, low-lying (d-σ) bonding molecular orbital, and a partially-full (d-σ)* antibonding molecular orbital, as shown in figure 3[19]. The extent of filling of the antibonding orbitals is determined by the electronic structure of the metal at the surface. The more the (d-σ)* state is filled, the larger the destabilization of the metal-adsorbate interaction. The location of the d-band center matches with the extent of filling of the antibonding molecular orbital (d-σ)*.

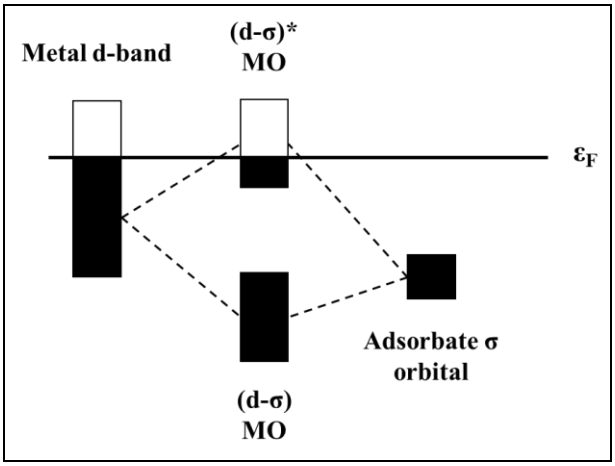

Figure 3. Representation of the metal d-band/adsorbate σ orbital interaction, and formation of (d-σ) and (d-σ)* molecular orbitals.

According to this model, a higher d-band center, with respect to the Fermi level, coincides with an increase in energy and the decrease in the filling of the (d-σ)* state, and a stronger metal-adsorbate bonding. On the contrary, lower d-band center (larger filling of the antibonding energy) leads to a weaker bonding.

Considering a core-shell system, the d-band center on the surface of the alloy is altered by the adjacent nucleus due to the action of geometrical and ligand effects.

1) The geometric effect can be understood in terms of increasing the overlapping of orbitals if the surface is compressed. This overlapping decreases the d-band center and the adsorption energy of adsorbates[20-21]. The tension in the shell would lead to the opposite effect, to a smaller overlapping and increase in the band-d center, which gives as a result a greater adsorption energy.
2) The ligand effect results from the difference in electronegativity between the core and the shell[22]. Electrons can migrate towards or away from the shell depending on the difference in electronegativity and as a result, the occupancy of the local

d-band may vary with the associated change in the adsorption energy of the adsorbates.

Thanks to its catalytic and chemical properties, platinum has been used, over the years, as a catalyst for many chemical and electrochemical reactions. The oxygen reduction reaction is not an exception, in fact, many scientific reports are based on morphological, structural, and electronic modifications of platinum and its alloys[102]. However, this metal is limited in the earth's crust, which is why in recent years, great efforts have been made to reduce and even replace platinum with other transition metals such as palladium, silver, and copper. Although these metals have given good electrochemical results, it has been proven that they are unstable in alkaline medium.

Due to its chemical nature, gold has excellent electrical conductivity, is stable in alkaline media, and has good catalytic properties. Thanks to the above, this work aims the synthesis of gold-based nanoalloys for their potential application as electrocatalysts of the oxygen reduction reaction in an alkaline medium.

It is known that platinum binds oxygen too strongly; the above suggests that its d-band center is too high. By alloying platinum with transition metals (TM) moves down the d-band center, so the oxygen-containing species binds on the alloy surface weakly, overall resulting in larger ORR activity for Pt-TM alloys[94].

To increase the activity against the oxygen reduction reaction of C-supported PtAu nanoalloys, Park and collaborators, in 2013, subjected PtAu/C catalysts to thermal treatments at 150°C under CO or Ar atmospheres[23]. After CO treatment, the Pt surface content of the PtAu nanoalloy enhanced from 66% to 74%, resulting in ORR mass activity enhancement of the PtAu-CO surface by 75.6% (33.2 A/g_{Pt}) with respect to 18.9

A/g_{Pt} for PtAu. The authors attributed this to the Pt atoms segregation on the surface of the electrocatalyst, which weakens the adsorption of OH^- ions.

Following this trend, in 2017, Liu and collaborators prepared PtCu nanoalloys and studied their application as bifunctional catalysts for ORR and ethanol oxidation reaction (EOR)[24]. The synthesis was carried out by one-step hydrothermal process. They obtained polyhedrons with sizes around 5 nm, atoms with low coordination number and many defects like edges and corners, which serve as active sites for electrocatalysis. The Tafel graphs showed that $Pt_{68}Cu_{32}$ nanoalloy presented higher catalytic activity than the commercial Pt/C catalyst since it has a lower slope.

In 2015, Han and collaborators indicated that stability and activity against the ORR of PtM (Fe, Co, Ni, Cu, Ru, Pd, and Ir) nanoalloys are related to the dissolution potential of the second metal[25]. When the dissolution potential of the non-noble metal tends to negative values, there is an increase in the electrocatalytic activity, but low chemical stability since it dissolves, leaving a Pt-rich surface. Of the non-noble metals tested, the best specific activities were obtained by alloying platinum with Fe, Co, and Ni. This could be explained as a function of the band-d center. The previous metals have lower electronegativities than Pt, which generates greater compression in the noble metal shell and a greater ligand effect, which decreases the d-band center of Pt, increasing its electrocatalytic activity.

In 2014, Yan and collaborators tried to diminish the amount of Pt of electrocatalyst for ORR by synthetizing Pt_xFe nanoalloys with a glycerol-stabilized $NaBH_4$ reduction method[26]. XRD showed a slight shift of the diffraction peaks towards higher angles, due to Fe incorporation into the Pt lattice. Electrochemical test showed that a slight

incorporation of Fe increases the Pt activity for ORR, which is noticed in Pt's mass activity (A/mg_{Pt}): PtFe/C: 0.08, Pt/C: 0.17, Pt_2Fe: 0.30, and Pt_3Fe: 0.33.

Table 1 summarizes some reports on the synthesis and application of PtM nanoalloys as electrocatalysts for the oxygen reduction reaction.

Table 1. Summary of PtM nanoalloys publication for ORR

Year	**Material**	**Contribution**	**Ref**
2015	PtNi/C	Synthesis of hollow PtNi/C nanocrystallites via galvanic replacement. The Pt's mass activity (A/mg_{Pt}) increased when it was alloyed with different portions of Ni: Pt/C: 12, PtNi(1:1)/C: 47, PtNi(1:2)/C: 62	[27]
2015	PtNi/N-doped carbon core/shell	Synthesis of a highly durable and active PtNi nanoparticles coated with a N-doped carbon shell by thermal annealing. The Pt's specific activity increased 11.4 times after the alloying and thermal annealing: Pt/C: 0.14 A/cm^2, PtNi/C: 1.6 A/cm^2	[28]

2016	PtNi/C nanostructures	Nanometer-sized PtNi/C (low Ni content) with different structures and grain boundaries. Electrochemical tests showed that highly defective nanostructures enhance the ORR specific activity. Pt/C commercial: 21 A/mg_{Pt} Hollow PtNi/C: 61 A/mg_{Pt} Sea sponge PtNi: 122 A/mg_{Pt}	[29]
2017	PtNi/C	Hydrothermal synthesis of PVP-stabilized PtNi supported on hollow carbon nanospheres. The authors emphasize that annealing and CO-stripping treatments enhance the catalytic towards the ORR, which was demonstrated with a more positive onset and peak potential compared with PtNi-not treated and Pt/C catalysts.	[30]
2017	PtNi	Synthesis of PtNi/Pt(111) by thermal annealing of Ni^{2+} on Pt(111). The nanoalloy annealed at 450 °C showed the best ORR activity (more positive onset potential and highest current). By increasing the temperature, electroactivity decreases, indicating that Ni sublimates or migrate to the bulk.	[31]

2017	PtFe/N-doped carbon	Synthesis of PtFe nanoalloy supported on N-doped porous carbon via thermolysis. The prepared material exhibited a more positive half-wave potential and high mass activity compared with commercial catalyst. PtNi/N-C: 0.92 V, 0.533 A/mg_{Pt} Pt/C: 0.88 V, 0.175 A/mg_{Pt}	32
2018	P-doped PtNi	Synthesis of P-doped PtNi (P-PtNi). The presence of phosphorous increases the electron density of Pt compared with PtNi, which contributes to the stabilization of the electronic structure and restrain the excessive HO_2^- species produced on the surface. The P-PtNi showed about 2 times enhancement for ORR compared to PtNi and Pt/C, respectively.	33
2019	PtFe/C PtCo/C PtNi/C	Low temperature impregnation-reduction method to synthetize C-supported PtM (M = Fe, Co, Ni). The PtNi/C (10 wt) exhibited the highest ORR performance compared even with commercial Pt/C (20 %) because of its electronic structure. Maximal activity was achieved with Pt:Ni atomic ratio 0.8/0.2 the material was also methanol tolerant.	34

2019	Pt_3Co	Electro-deposition of Pt_3Co on carbon fiber paper. Time of electro-deposition plays a crucial role in the characteristics of obtained Pt_3Co@CFP, the material prepared at 10 min exhibited the best ORR activity, following four electron pathway, an onset potential of 0.85 V *vs.* RHE at 1.0 mA/cm^2 and a Tafel slope of 63 mV/dec.	[35]
2019	Au-PtFe/C	Highly ordered Au-PtFe intermetallic structure entrapped in porous carbon. The optimal Au-PtFe/C exhibited initial specific and mass activities 9 times higher than the commercial Pt/C catalyst for the ORR. The presence of little amounts of gold gives a higher electrochemical stability.	[36]
2019	PtM_3: $Pt(Fe, Co, Ni)_3$	Synthesis of $Pt(Fe, Co, Ni)_3$/C through spray dehydration and annealing. Electrochemical characterization showed that nanoalloys annealed at 600 and 700 °C carried out the ORR via four electrons. The onset potentials for ORR were: Pt(Fe, Co, Ni)/C-600 1.031 V, Pt(Fe, Co, Ni)/C-700 1.019 V, and Pt/C 1.003 V.	[37]
2019	CoPt/C	C-supported Co95Pt5 nanocatalyst prepared via deposition-precipitation and CO annealing.	[38]

		Best results were obtained with the material treated at 470 K under CO atmosphere, because the onset potential for ORR were more positive compared with commercial Pt/C. Even tough, the synthesis procedure did not allow to obtain secondary phase free catalysts.	

Platinum and palladium belong to the same family, so they share similar electronic structures. Because palladium is more abundant in the Earth's crust than Pt, some researchers targeted Pd as a base metal to elaborate more efficient (and available) ORR catalysts. In this seek, one must consider that palladium is quite reactive versus Pt, and that it combines (more) strongly with oxygen, which results in non-negligible extent of Pd-oxides coverage when the potential is increased, which can adversely affect the oxygen reduction reaction kinetics. Like for platinum, the electrocatalytic activity of palladium can be improved by alloying it with other metals on the nanometer scale[39-42].

The design of bimetallic nanoalloys is relevant, because the less active metal increases the activity of the more active one. Slanac et al., in 2012, reported the synthesis of Ag-rich AgPd nanoalloys[43]. The resulting nanoparticles were crystalline and uniformly alloyed. In the high-Ag nanoalloys ($Ag_{>4}Pd$), the surface contained palladium atoms surrounded by silver, this morphology being favorable for the oxygen reduction reaction, since the combination of the electronic structures of both metals favors the breakage of the O=O bond and the desorption of the reaction intermediates.

In 2014, Liu and collaborators reported the synthesis of C-supported PdM (M= Co, Ni) nanoalloys by reduction and annealing in H_2 or N_2 atmosphere[44]. By increasing the

temperature, the lattice constant of the nanoalloys becomes smaller and their particle size got bigger. With lineal sweep voltammetry measurements, it was demonstrated that better activity towards ORR were achieved by increasing the nanoalloys particle size and by contracting their lattice, a similar effect as for Pt-based ORR catalysts.

Following this trend, in 2015, Wu and co-workers published the synthesis of PdCu/C nanoalloys prepared by two chemical methods[45]. Stability and synergy of the materials were depending on size, composition, phase and surface properties. For both methods, $Pd_{54}Cu_{46}$ gave better results towards the ORR, since the onset potential were very similar to that of Pt/C. The above can be explained because of the tendency of Cu to leach, which leaves a Pd-rich surface, increasing the electrochemical active area (ECA), and probably yielding to strained Pd surfaces, which (if they behave like Pt surfaces in acidic conditions) should be more active for the ORR[95-96].

Next year, in 2016, Holade and colleagues addressed the synthesis of PdM/C (M= Fe, Mn) nanoalloys for the oxygen reduction reaction in alkaline medium via bromide exchange[46]. The best results were achieved with PdFe/C because it reached a limit current density of -6.5 mA/cm^2 at 0.5 V *vs.* RHE, which was bigger than that achieved with PdMn/C nanoalloy. The improvement in the electrocatalytic activity, in comparison with others Pd based nanoalloys, were attributed to the absence of any organic contaminants or ligands on the surface of the material following their methodology of synthesis.

In 2017, Abo and Ibrahem used a modified polyol reduction method to prepare C-supported PdNi nanoalloys[47]. TEM characterization revealed spherical particles with diameters between 20-50 nm, distributed in non-homogeneous manner with some agglomerations. They used the RDE technique to study the electrocatalytic properties of

those materials. It was concluded that the nanoalloy calcined at low temperature (300°C) was the one with the highest activity against the oxygen reduction reaction thanks to its smaller particle size and greater electroactive surface.

The development of more active and stable nanoalloys for the ORR is desirable for the commercial application of fuel cells technology. In 2017, Zhang and collaborators reported the synthesis of PdCo nanoparticles encapsulated in N-doped porous carbon[48]. The support effectively prevented the agglomeration and dissolution of the nanoalloys particles during fuel cell operation. The peak potential for the ORR in the PdCo/N-dopped carbon were slightly more positive (0.902 V *vs.* RHE) than that of commercial Pt/C (0.899 V *vs.* RHE). Authors attributed the excellent electrocatalytic performance to the synergistic effect between structures and chemical composition.

Silver and its alloys are stable and active against the oxygen reduction reaction in alkaline medium. In addition, the price of silver is more than 50 times less than that of platinum, which makes it an attractive candidate. The improvement of the catalytic activity of silver alloying it in the nanometric scale has taken great relevance to minimize the cost of batteries and alkaline cells. Like the previous materials, silver alloys usually present a synergistic effects between their components[49-50].

Nanoparticles of AgAu alloys partially capped with 1-dodecine were synthesized in 2015 by Hu *et. al*[51]. The AgAu nanoalloy with 33.5% of gold showed a higher activity for the ORR, due to the higher onset potential, number of electrons transferred and kinetic current. The above is attributed to a better adsorption of oxygen on the catalyst surface.

In addition to the previously mentioned metals, silver has also been alloyed with non-noble metals such as Co[52-53] and Ni[54], giving comparable results to the Pt/C electrode as electrocatalysts for the ORR.

Since its discovery, gold catalysts have received an increasing interest and they enabled to successfully carry out many (electro)chemical reactions[55-56]. It is known that gold, either alone or in combination with other metals, is an excellent electrocatalyst in redox reactions, thanks to its great chemical stability in the water potential window and its resistance to the formation of oxides. Gold is also ca. 10 times more abundant than Pt and Pd in the Earth's crust and under less pressure of usage than Ag[97]. Even though, of course, alloying gold to other elements has multiple assets.

There are reports about the synthesis of gold bimetallic nanoalloys in combination with metals such as Pt[57-58] and Pd[59], which have presented good catalytic activities against the ORR. In addition, the synthesis of bimetallic nanoparticles on a carbon support can be carried out in a single step[60]. However, using a combination of these two noble metals increases the cost of the resulting material.

Since oxygen is not absorbed so strongly on gold's surface, this metal is usually alloyed with other low-cost metals to modify its electronic structure and enhance the ORR activity. Unlike Pt-based nanoalloys, for Au-based nanoalloys the aim is to increase the d-band center with respect to the Fermi level, to promote the chemisorption of oxygen-containing species on the surface of the material.

In 2016, Jiali and collaborators prepared AuNi dendrites by combining electrodeposition and electrochemical dealloying methods. They concluded that the presence of nickel into the gold lattice leads to a positive shift in the d-band center versus the Fermi level, which favors the absorption of oxygen species and enhances the

electrochemical activity towards the ORR. The half-wave potential of the AuNi dealloyed electrocatalyst exhibits a positive shift of 27 mV with respect to the commercial Pt/C[61].

Next year, in 2017, Jiali and colleagues improved the distribution and composition of Au and Ni by developing a one-pot method to prepare dealloyed AuNi nanodendrites. The as-synthetized material showed a half-wave potential and a specific activity (at 0.85 V *vs.* RHE) 81 mV more positive and 3.1 times higher than Pt/C[62].

In 2018, Gong and collaborators performed the synthesis, via one-pot hydrothermal process of CuO-supported AuNi nanoalloy[63]. To see the electrocatalytic activity of the composite, rotating disk electrode tests were made. The AuNi-CuO composite exhibited a half-wave potential of 0.82 V *vs.* RHE, which was the same of commercial Pt/C. Kinetic activity was determined with Tafel plots, the AuNi-CuO catalyst had a Tafel slope of 64.8 mV/dec, lower than Pt/C (80.4 mV/dec).

In 2018, Wang and colleagues reported, for the first time, the synthesis of AuCu aerogels and their application as electrocatalysts in the oxygen reduction reaction[64]. The material with proportions $Au_{52}Cu_{48}$ presented specific and mass activities 4.5 and 6.3 times higher than those obtained with the Pt/C, as well as stability after 10,000 cycles. The synergistic effect in the material was attributed to the change in the gold band-d center because of the insertion of copper.

Another proof of this was published in 2018, when Kohei and collaborators synthetized an AuIr solid solution nanoalloy via chemical co-reduction[65]. X-ray measurements showed that lattice constant linearly decreased with increasing Ir content, following Vegard's Law. To investigate the activity towards the ORR of this nanoalloy, rotating disk electrode tests were made. $Au_{0.5}Ir_{0.5}$ catalyst began to catalyze the reaction

at 1.0 V *vs.* RHE, which is comparable to the onset potential of the commercial Pt/C, however, the kinetic current density was a little lower on $Au_{0.5}Ir_{0.5}$ than that on Pt/C. Tafel slopes on $Au_{0.5}Ir_{0.5}$ and Pt/C were similar, 61.7 and 64.2 mV/dec, respectively.

These strategies demonstrate that AuM nanostructures can outperform Pt for alkaline ORR. However, it is no secret that dendritic and aerogel-based nanostructures are not easy to implement in real fuel cell electrodes without substantial loss of apparent activity, as demonstrated for Pt-based PEMFC electrodes[66]. So, it is wise, also, to search for advanced carbon-supported Au-based electrocatalysts, that could substitute Pt-based ones.

As mentioned, to improve the electron transfer kinetics in the oxygen reduction reaction it is necessary to use electrocatalysts capable of carrying out this reaction with a lower overpotential. However, most of these materials are made from platinum, which raises the important issues of the cost of the devices and the availability of its constitutive materials. Functional materials have taken special attention because they combine the properties offered by their components. They generally consist of a support on which an electrocatalyst is deposited.

The catalyst must be electrochemically active for the oxygen reduction reaction and chemically stable in the reaction medium. The nanoalloys with noble and non-noble metals have shown to satisfy the above requirements to be applied as cathodes in fuel cells. Most of the research have been focused on the combination of noble metals such as Pt, Pd, and Ag with non-noble metals such as Fe, Co, and Ni. The application of Au-based bimetallic nanoalloys to the ORR is low. However, gold having a greater electronegativity than platinum, it would be expected a greater binding effect to be

alloyed with the previous non-noble metals, increasing its activity towards the oxygen reduction reaction, not to speak from its 10 times larger availability in the Earth's crust.

Considering the above, this work proposes the synthesis and characterization of AuM nanoalloys (M = Fe, Co, and Ni) supported on carbon black, and its application as electrocatalyst for the oxygen reduction reaction in alkaline electrolyte.

HYPOTHESIS

For this work, we postulate that the presence of Fe, Co, and Ni increases the catalytic activity of the gold for the oxygen reduction reaction. This hypothesis will be tested hereafter.

OBJECTIVES

GENERAL OBJECTIVE

Synthesize and characterize AuM bimetallic nanoalloys (M = Fe, Co, and Ni) supported on carbon black, and evaluate their electrocatalytic activity for the oxygen reduction reaction in alkaline fuel cells.

SPECIFIC OBJECTIVES

1. Synthesize Carbon-supported AuM bimetallic nanoalloys (M = Fe, Co, and Ni).
2. Characterize morphologically, chemically and crystallographically the materials synthesized by transmission electron microscopy (TEM), energy dispersive X-ray spectroscopy (X-EDS), inductively coupled plasma-mass spectroscopy (ICP-MS), X-ray photoelectron spectroscopy (XPS), and X ray diffraction (XRD).
3. Determine the electrocatalytic activity of the AuM/C composites (M = Fe, Co and Ni) towards the oxygen reduction reaction by cyclic and linear voltammetry with rotating disk electrode.
4. Perform stability tests on AuM/C composites (M = Fe, Co, and Ni) by accelerated degradation tests.

CHAPTER 2: MATERIALS AND METHODS

2.1 Project development location

This project was carried out at the Universidad Autónoma de Nuevo León (UANL-Mexico), and the Université Grenoble Alpes (UGA-France). Most of the synthesis procedures and crystallographic characterization were made in the Laboratory of Materials II: Energy Storage and Conversion of the School of Chemistry (FCQ, UANL). Most of the electrochemical, chemical, electronic microscopy, and morphological characterizations were made in the Laboratory of Electrochemistry and Physical-Chemistry of Materials and Interfaces (LEPMI, UGA).

The description of the reagents used, the equipment, as well as analytical and experimental procedures followed in this investigation are detailed in this section, to clearly describe the conditions and purposes in each stage.

2.2 Materials and methods

2.2.1 Reagents

Gold(III) chloride ($AuCl_3$ 99%, Sigma-Aldrich, Saint Louis, MO, USA), iron(III) chloride ($FeCl_3$ Reagent grade 97%, Sigma-Aldrich, Saint Louis, MO, USA), cobalt(II) nitrate hexahydrate ($Co(NO_3)_2$-$6H_2O$ ACS reagent ≥98%, Sigma-Aldrich, Saint Louis, MO, USA), nickel(II) nitrate hexahydrate ($Ni(NO_3)_2$-$6H_2O$ 99.99%, Sigma-Aldrich, Saint Louis, MO, USA), ethylene glycol (ReagentPlus ≥99%, Sigma-Aldrich, Saint Louis, MO, USA), Carbon black (C_{black} acetylene, 99.9%, S. A. 80 m^2 g^{-1}, Alfa Aesar, Ward Hill, MA, USA), ethanol (Absolute, CTR Scientific, Monterrey, N. L., Mexico), Nafion® 117 (5% p/p isopropanol, Sigma-Aldrich, Saint Louis, MO, USA), isopropanol (ACS 99.5%, Alfa Aesar, Ward Hill, MA, USA), potassium hydroxide (KOH 99.98%, Alfa Aesar, Ward Hill, MA, USA), dioctyl sulfosuccinate sodium salt (AOT 96%, Thermo Fisher Scientific, Waltham, MA, USA), and n-Heptane (<99%, Sigma-Aldrich, Saint Louis, MO, USA) were used as-received without further treatment. Gas mixture H_2 2% /Ar (Air Liquide, Paris, France) was used for heat treatments. Ultrapure Ar (99.999%, Air Liquide, Paris, France) and O_2 (≥ 99.999%, Air Liquide, Paris, France) were used to deaerate the electrolyte solution for experiments in supporting electrolyte, and saturate the electrolyte for oxygen reduction reaction experiments, respectively.

2.2.2 Preparation of carbon-supported Au:Co and Au:Ni nanoalloys by ethylene glycol-stabilization method

Au:Co/C-EG and Au:Ni/C-EG catalysts were prepared by the so-called ethylene glycol-stabilization method (EG) at room temperature, and varying the volume of the Co and Ni solutions. For this purpose, 10 mL of 0.001 M $HAuCl_4$/EG and 3.3, 5 or 10 mL of 0.001 M $CoCl_2 \cdot 6H_2O$/EG or 0.001 M $NiCl_2 \cdot 6H_2O$/EG were mixed under stirring. Then, appropriate amounts of C_{black} and $NaBH_4$ were added to the solution under vigorous stirring. The molar ratio of metals:$NaBH_4$ was fixed to 1:20 (which corresponds to a large excess of the reducer). It is worth mentioning that the pH of the solution was expected to be slightly acidic because the addition of 1 mL of 0.1 M HCl for the dissolution of $HAuCl_4$ salt. After 4 h, black powders were collected by centrifugation, washed several times with water:ethanol 1:1 mixture, and dried at 80°C overnight.

2.2.3 Preparation of carbon-supported Au:Fe, Au:Co and Au:Ni nanoalloys by stirring method

Au:Fe/C-S, Au:Co/C-S and Au:Ni/C-S catalysts were prepared by the so-called stirring method (S) at room temperature. To carry it out, 15 mL of 0.001 M $HAuCl_4$ and 3 mL of 0.006 M $FeCl_3$, $CoCl_2 \cdot 6H_2O$ or 0.006 M $NiCl_2 \cdot 6H_2O$ aqueous solutions were mixed under stirring, and the pH was adjusted to 10 by adding drops of a NaOH solution. Then, appropriate amounts of carbon black (C_{black}) and $NaBH_4$ were added to the solution under vigorous stirring. To promote further reduction of metallic ions, the molar ratio of metals:$NaBH_4$ was fixed to 1:3. After 4 h, black powders were collected by

centrifugation, washed several times with water:ethanol 1:1 mixture, and dried at 80°C overnight.

2.2.4 Preparation of carbon-supported Au:Fe/C, Au:Co and Au:Ni nanoalloys by hydrothermal method

Au:Fe/C-HT, Au:Co/C-HT and Au:Ni/C-HT catalysts were prepared by the so-called hydrothermal method (HT). To do so, 15 mL of 0.001 M $HAuCl_4$ and 3 mL of 0.006 M $FeCl_3$, $CoCl_2 \cdot 6H_2O$ or 0.006 M $NiCl_2 \cdot 6H_2O$ aqueous solutions were placed into a Teflon vessel, and the pH was adjusted to 10. Then, C_{black} and $NaBH_4$ were added. As the reducing agent can decompose at high temperatures, and to boost the reduction of the metal salts, the molar ratio of metals:$NaBH_4$ was fixed to 1:3. The above solution was transferred to a Teflon lined autoclave and heated to 180°C for 4 h (Quincy lab 20GC, Chicago, IL, USA). The resulting black powders were filtrated, washed repeatedly with water:ethanol 1:1 mixture, and dried at 80°C overnight.

To compare the electrocatalytic activity of the materials, Au/C composite was prepared by adding 20 mL of 0.001 M $HAuCl_4$ aqueous solution into a Teflon vessel, and following the procedure described above.

2.2.5 Preparation of carbon-supported Au:Ni nanoalloys by reverse microemulsion

Au:Ni/C-MO catalysts were prepared by the so-called reverse microemulsion method (MO) at room temperature. The synthesis started with two solutions:

- Solution A: 200 µL of 0.1 M $HAuCl_4$ and 200 µL of 0.1 M of $NiCl_2 \cdot 6H_2O$ aqueous solutions dispersed in 0.1 M AOT dissolved in n-heptane.

- Solution B: $NaBH_4$ dispersed in 0.1 M AOT dissolved in n-heptane. The molar ratio of metals:$NaBH_4$ was equal to 1:30.

Equal volumes of solutions A and B were mixed under vigorous stirring for 30 min. Then, an appropriate amount of C_{black} was added to the solution and stirred for 2 h. The resulting black powders were filtrated, washed repeatedly with water and ethanol, and dried at 80°C overnight.

Different surfactant molar ratios (R-w) were tested by varying the volume of solutions A and B as showed below.

R-w	**$V_{solution\ A}$ (mL)**	**$V_{solution\ B}$ (mL)**
5	25	25

The materials were subjected to heat treatments under H_2 2%/Ar atmosphere at 250°C (Nabertherm RS 80/300/13 Tube furnace, Bremen, Germany) during 2 h.

2.3 Characterization techniques

2.3.1 X-ray diffraction (XRD)

Crystallographic studies and phase determination were made by X-ray diffraction (XRD) using two equipment.

- For EG, S and HT materials: XRD (Bruker 2D Phaser, Billerica, Massachusetts, USA) at room temperature, using Cu–Kα (λ = 1.5418 Å) radiation. X-ray scans were carried out from 5° to 90° in 2θ, in steps of 0.5° and time of 0.5 s. Also, a fluorescence filter was applied to the detector.
- For MO materials: XRD (PANalytical X'Pert PRO, Malvern, Worcestershire, UK) at room temperature. X-ray scans were carried out from 10° to 100° in 2θ, in steps of 0.039°.

Vegard's law calculations were made to estimate the molar fraction of Fe, Co, and Ni present on the nanoalloys, while Scherrer equation was used to estimate the crystallite size.

2.3.2 Transmission electron microscopy with energy-dispersive X-ray spectroscopy

The obtained carbon-supported nanoparticles shape, size, size distribution, and local chemical analysis were studied with a transmission electron microscope, TEM (JEOL 2010 TEM, 200 kV, point to point resolution 0.19 nm), coupled with an energy-dispersive X-ray spectroscopy detector, X-EDS (INCA Energy TEM 100X). For this purpose, one drop of the catalyst slurry (same ink as used for electrochemical

experiments, see hereafter) was placed on a copper TEM grid, followed by drying at room temperature.

2.3.3 Inductively coupled plasma mass spectrometry

Inductively coupled plasma mass spectrometry, ICP-MS (NexION 2000, PerkinElmer, Waltham, MA, USA), was used to determine the catalysts composition, analyzes were made in standard mode with calibration using an internal standard (Rh-103). For that purpose, 3 mg of the catalysts materials were previously digested in 10 mL of *aqua regia,* with the help of a microwave digestion system. The obtained solutions were appropriately diluted for the measurements.

2.3.4 X-ray photoelectron spectroscopy

X-ray photoelectron spectroscopy, XPS patterns were obtained using a Thermo Scientific K-alpha spectrometer with a monochromate Al X-ray source ($h\nu$ = 1486.6 eV; spot size 400 μm). Pass energies of 30 and 100 eV were used to record the core level and the survey spectra, respectively. All spectra were acquired using an electron flood gun to compensate possible positive charge accumulation during measurements. The obtained spectra were de-convoluted and fitted using Thermo Scientific Advantage Software.

2.3.5 Electrochemical measurements

Electrochemical tests were carried out in a standard three-electrode cell connected to an electrochemical station (VMP2, BioLogic Science Instruments, Seyssinet-Pariset, France) with a glassy carbon plate as the counter electrode and a Hg/HgO (0.1 M KOH)

as the reference electrode; all the potential values are nevertheless expressed on the reversible hydrogen electrode (RHE) scale (equation 5).

$$E_{RHE} = E_{Hg/HgO} + \left(E^{o}{}_{Hg/HgO} - E^{0}{}_{RHE}\right) = E_{Hg/HgO} + 0.932\ [=]\ V \qquad \text{Equation 5}$$

The whole cell (and any glassware used for the experiments) was previously soaked in concentrated Caro's acid overnight and thoroughly rinsed with ultrapure water (18.2 MΩ cm, < 3ppb total organic carbon) prior any experiment. The working electrode was a glassy-carbon rotating ring-disk electrode (GCE, diameter: 5 mm, area: 0.2 cm^2) from Pine instruments, onto which a thin-film of the desired electrocatalyst was formed. To that goal, all the synthesized materials were ultrasonically dispersed, along with an amount of Nafion® 117 (powder:Nafion 1:1 mass ratio), in ethanol:water (90:10 volume ratio) solution. Afterward, two drops of 5 µL of this ink were deposited onto the surface of the glassy carbon electrode. The total metal loading of each nanoalloy on the galssy-carbon electrode was fixed at 10 µg cm^{-2}.

2.3.6 Cyclic voltammetry

The electrochemical behavior of the carbon-supported nanoalloys was tested by cyclic voltammetry (CV) in Ar-saturated 0.1 M KOH from 0.032 to 1.032 V *vs.* RHE, at a scan rate of 50 mV s^{-1}, from which the electrochemical surface area (ECSA) of the electrocatalysts were determined. For this purpose, the Au-oxide reduction peak coulometry is integrated, and the ECSA is calculated as follows (equation 6),

$$ECSA = \frac{Q}{(0.386)(X_{Au})} \cdot 100[=]\ m^2 g^{-1}{}_{Au} \qquad \text{Equation 6}$$

where Q is the total charge for the reduction of Au-oxide (mC), 0.386 is a constant assuming that a monolayer of Au oxides was formed (mC cm^{-2}), X_{Au} is the mass of Au loading (μg), and 100 is a conversion factor.

2.3.7 Rotating ring-disk electrode technique

The electrocatalytic performance towards ORR was measured by cyclic voltammetry in O_2-saturated 0.1 M KOH from 1.032 to 0.032 V *vs.* RHE, at 5 mV s^{-1} and rotation speeds of 225, 400, 625, 900, 1225, and 1600 rpm. From this data, kinetic markers of the ORR were determined: the onset potential and the half-wave potential of ORR. The onset potential was determined as the potential measured for a faradaic current density of -0.1 mA cm^{-2} on the ORR polarization plot recorded at 1600 rpm. The half-wave potential was determined as the potential when the current is the half of the limiting current (also on the plot at 1600 rpm). The ring electrode was subjected to chronoamperometry at 1.032 V *vs.* RHE, to detect HO_2^- anions possibly formed at the Au-M/C disk.

2.3.8 Accelerated degradation test

Finally, the electrocatalytic stability of the materials was tested. For this purpose, the electrocatalysts were subjected to an accelerated degradation test (ADT), consisting of 5,000 continuous cycles of CV between 0.5 and 1 V *vs.* RHE with a scanning rate of 100 mV s^{-1} in an O_2-saturated 0.1 M KOH, at room temperature. ECSAs and ORR

polarization curves at 1600 rpm of the materials before and after the potential cycling were measured to evaluate the fate of each electrocatalyst upon the AST.

2.4 Disposal of the generated waste

The disposal of all waste, both chemical substances and disposable material, generated throughout this work was done in accordance with current regulations of the School of Chemistry, UANL, and of the Laboratory of Electrochemistry and Physical-Chemistry of Materials and Interfaces, UGA.

CHAPTER 3: RESULTS

In this chapter will be presented the results obtained during the research project. For a better understanding of them, the samples of developed materials will be identified as follows:

- AuNi/C-EG-3.3: carbon-supported AuNi nanoalloy prepared via ethylene glycol stabilization method, using 3.3 mL of Ni precursor.
- AuNi/C-EG-5: carbon-supported AuNi nanoalloy prepared via ethylene glycol stabilization method, using 5 mL of Ni precursor.
- AuNi/C-EG-10: carbon-supported AuNi nanoalloy prepared via ethylene glycol stabilization method, using 10 mL of Ni precursor.
- AuCo/C-EG-3.3: carbon-supported AuCo nanoalloy prepared via ethylene glycol stabilization method, using 3.3 mL of Co precursor.
- AuCo/C-EG-5: carbon-supported AuCo nanoalloy prepared via ethylene glycol stabilization method, using 5 mL of Co precursor.
- AuCo/C-EG-10: carbon-supported AuCo nanoalloy prepared via ethylene glycol stabilization method, using 10 mL of Co precursor.

- AuFe/C-S: carbon-supported AuFe nanoalloy prepared via aqueous solution stirring method at room temperature.
- AuCo/C-S: carbon-supported AuCo nanoalloy prepared via aqueous solution stirring method at room temperature.
- AuNi/C-S: carbon-supported AuNi nanoalloy prepared via aqueous solution stirring method at room temperature.

- Au/C-HT: carbon-supported Au via hydrothermal method.
- AuFe/C-HT: carbon-supported AuFe nanoalloy prepared via hydrothermal method.
- AuCo/C-HT: carbon-supported AuCo nanoalloy prepared via hydrothermal method.
- AuNi/C-HT: carbon-supported AuNi nanoalloy prepared via hydrothermal method.

- AuNi/C-MO-ap: carbon-supported AuNi nanoalloy prepared via reverse microemulsion Rw-5 as prepared.
- AuNi/C-MO-2h: carbon-supported AuNi nanoalloy prepared via reverse microemulsion Rw-5 with heat treatment at 250°C for 2 h.

3.1 Carbon-supported nanoalloys prepared via ethylene glycol stabilization method

The carbon-supported AuCo and AuNi nanoalloys prepared by ethylene glycol stabilization method were firstly characterized by powder X-ray diffraction. In Figure 4, it is possible to see that all samples crystallized in a typical face-centered cubic structure (FCC). The diffraction peaks located at 38.17°, 44.37°, 64.55°, 77.53°, and 81.69° in 2θ are assigned to {111}, {200}, {220}, {311}, and {222} crystallographic planes of Au. The signal at 26.6° in 2θ corresponds to the {002} family of planes of graphite. There are no diffraction peaks different from those of Au in Figures 4a and 4b; so, no crystalline secondary phases of the co-metals or impurities are discarded for the EG-stabilization method (some could be present in amorphous state, though).

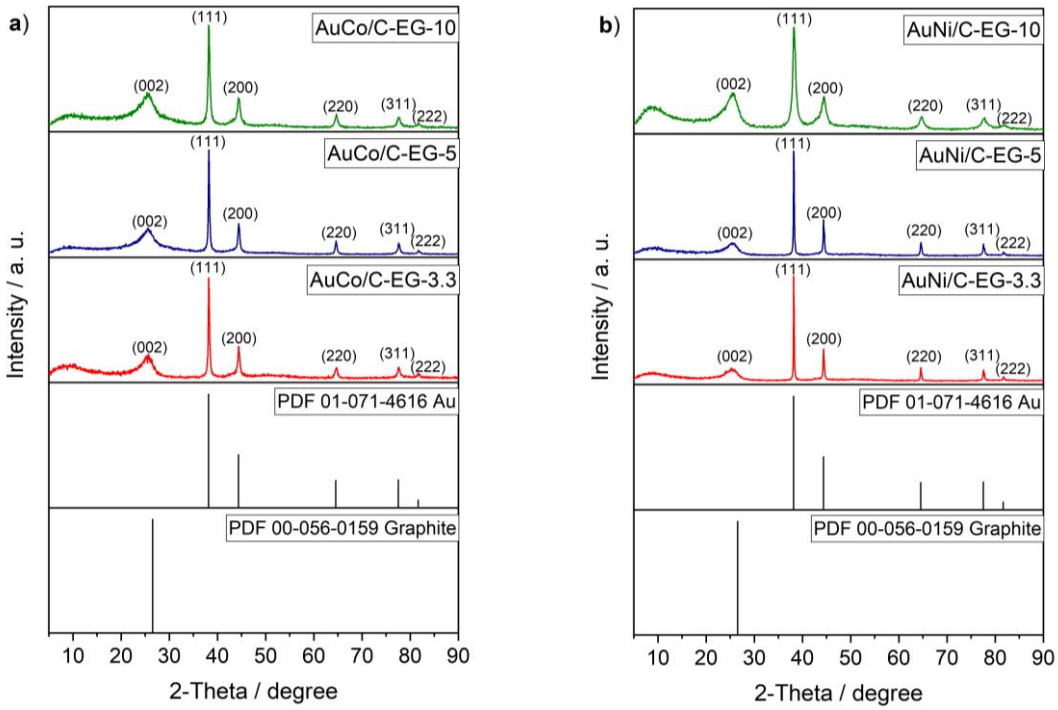

Figure 4. X-ray diffraction patterns of a) AuCo/C-EG and b) AuNi/C-EG nanoalloys prepared using different volume of Co or Ni precursor, respectively.

Making an approaching between 36° and 40° in 2θ, figure 5b show that the diffraction peak angle for the (111) family of planes of AuNi/C-EG-10 were slightly higher compared to pristine Au. This can be explained because nickel (1.62 Å) has atomic ratio smaller than gold (1.79 Å). A wider diffraction peak is also observed for this material, indicating that the long-range order decreased due to the presence of Ni. For AuCo/C-EG-3.3, AuCo/C-EG-5, AuCo/C-EG-10, AuNi/C-EG-3.3 and AuNi/C-EG-5, the two previous phenomena are not observed, a possible indication that the alloying of the metals was carried out in a lesser way.

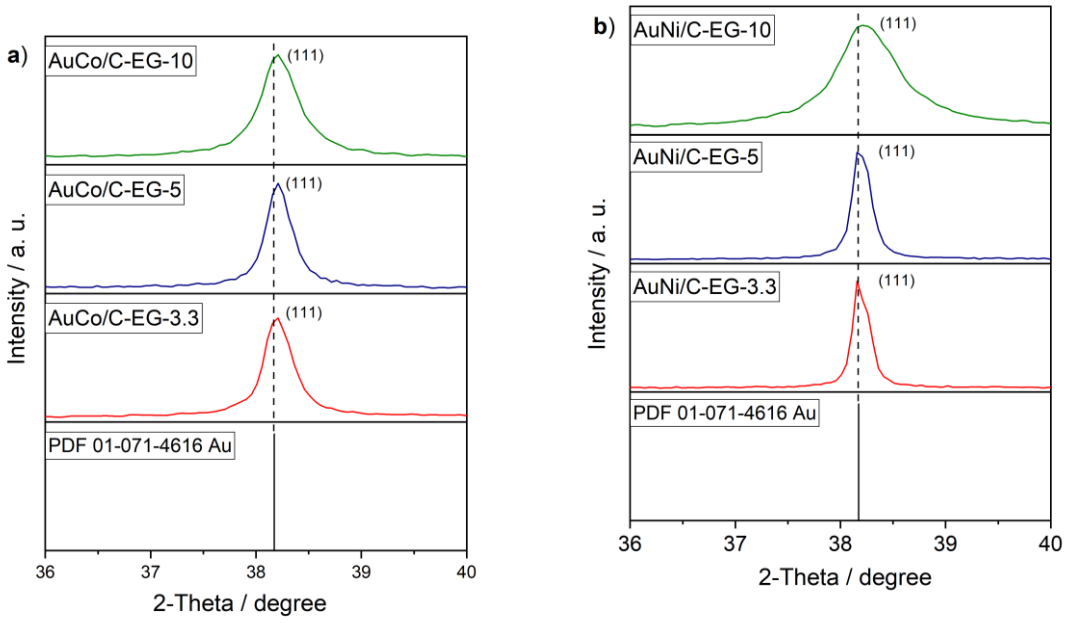

Figure 5. Zoom of X-ray diffraction patterns of a) AuCo/C-EG and b) AuNi/C-EG nanoalloys prepared using different volume of Co or Ni precursor, respectively.

Bragg's Law (equation 7) is a well-studied principle that provides the condition for a plane wave to be diffracted by a family of lattice planes:

$$n\lambda = 2d_{hkl}\sin\theta$$ Equation 7

Where d_{hkl} is the interplanar spacing, θ is the angle between the incident plane and the lattice planes, λ is the wavelength, and *n* is the order of the reflection. It is possible to calculate the interplanar space of the nanoalloys with Equation 7.

Vegard's law (equation 8) is an approximate empirical rule. It establishes a lineal relation between the crystal lattice constant of an alloy and the concentration of the constituent elements, if the temperature is constant.

$$a_{A_{(1-x)}B_x} = (1-x)a_A + xa_B$$ Equation 8

Where $a_{A_{(1-x)}B_x}$ is the lattice constant of the alloy $A_{(1-x)}B_x$, a_A is the lattice constant of the metal A, a_B is the lattice constant of the metal B, and x is the molar fraction of metal B incorporated into the crystal lattice of A.

An approximation of the molar fraction of metals (Fe, Co, Ni) that was incorporated into the Au lattice was made with equation 8. Those results are summarized in table 2.

Inductively coupled plasma – mass spectrometry (ICP-MS) was performed to quantitatively determine the global Au, Co, and Ni contents of the materials on the carbon support. These results are summarized in Table 2. The concentration of Co and Ni is lower than the expected; this can be explained by two phenomena. As the pH of the solution was not fixed to 10, the $NaBH_4$ added could have been discomposed, avoiding the reduction of the transition metals. Also, as the pH was slightly acidic, within the system could not be generated monoanions of ethylene glycol that form cobalt/nickel ethylene glycoxides, and allow to reduce the Co(II) and Ni(II) ions[72].

Table 2. Metal content determined by Vegard's Law calculations, and ICP-MS

	Vegard's Law		ICP-MS					
	Atomic percent (%)		Atomic percent (%)			Weight percent (%)		
Material	**Co**	**Ni**	**Au**	**Co**	**Ni**	**Au**	**Co**	**Ni**
AuCo/C-EG-3.3	0.2		99.6	0.4		9.0	0.01	
AuCo/C-EG-5	0.4		99.5	0.5		9.3	0.01	
AuCo/C-EG-10	0.6		99.3	0.7		9.2	0.02	
AuNi/C-EG-3.3		-	99.7		0.3	9.8		0.01
AuNi/C-EG-5		0.2	99.6		0.4	9.7		0.01
AuNi/C-EG-10		0.8	93.6		6.4	9.6		0.19

*For the atomic percentage by ICP-MS, only the proportion of metals was considered. In the percentage by weight, the carbon support was also considered.

As shown in table 2, all the atomic percent calculated with Vegard's Law are lower than the atomic percent determined by ICP-MS. What is true is the trend, that is, by using a greater volume of solution, the fraction of Co or Ni that is incorporated into the Au network increases. As expected, only the AuNi/C-EG-10 sample has a non-negligible amount of Ni that was incorporated to the lattice of gold. These results agree with the behavior seen by X-ray diffraction.

Scherrer equation (equation 9) is a useful mean to estimate the crystallite size of polycrystalline materials[91].

$$\tau = \frac{K\lambda}{\beta \cos\theta} \qquad \text{Equation 9}$$

where, τ is the mean size of the crystal, K is a shape factor, λ is the X-ray wavelength, β is the line broadening at half the maximum intensity, and θ is the Bragg angle. In this work, only the diffraction signal at 38.18° in 2θ was used to calculate the crystallite size. The results of the crystallite size will be presented, and discussed, along with the data obtained with transmission electron microscopy.

Shape, size, and particle size distribution of the catalysts onto the carbon support were investigated by TEM. As it is seen, in figure 6, all the electrocatalyst showed rather large particles (several 10 nm in diameter) with near-spherical morphology. The large size of the particles can in part be associated with the rather low specific area of the C_{black} used (80 m^2 g^{-1}) compared to "classical" carbon black substrates used in electrocatalysis (e.g. Vulcan XC72: 240 m^2 g^{-1}).

Figures 6a correspond to the TEM micrograph of AuCo/C-EG-3.3, and 6c of AuCo/C-EG-5; in both cases, 66% of nanoparticles have diameters lower than 60 nm, and an average of 49 ± 23 nm and 57 ± 18 nm, respectively. With Scherrer calculations, the mean crystallite sizes were 31 nm and 32 nm for AuCo/C-EG-3.3 and AuCo/C-EG-5, respectively. The results agree with the fact that the crystallite size usually is smaller to the particle size, which indirectly shows that some individual crystallites can be agglomerated into bigger (polycrystalline) particles, or that the individual crystallites can be surrounded by amorphous caps. From figure 6e, it is possible to determine that 66% of the AuCo/C-EG-10 particles have diameters lower than 30 nm, with a mean of 32 ± 21 nm. The Scherrer-calculated crystallite size was 23 nm, again, smaller that the particle size.

In comparison, figures 6b and 6d show micrographs of AuNi/C-EG-3.3 and AuNi/C-EG-5, respectively; in these cases, the average diameters are 257 nm ± 112 nm (48 nm by Scherrer), and 97 nm ± 37 nm (44 nm by Scherrer), respectively. Finally, figure 6f displays that 20% of AuNi/C-EG nanostructures are smaller than 30 nm, with an average of 44 ± 22 nm (14 nm by Scherrer).

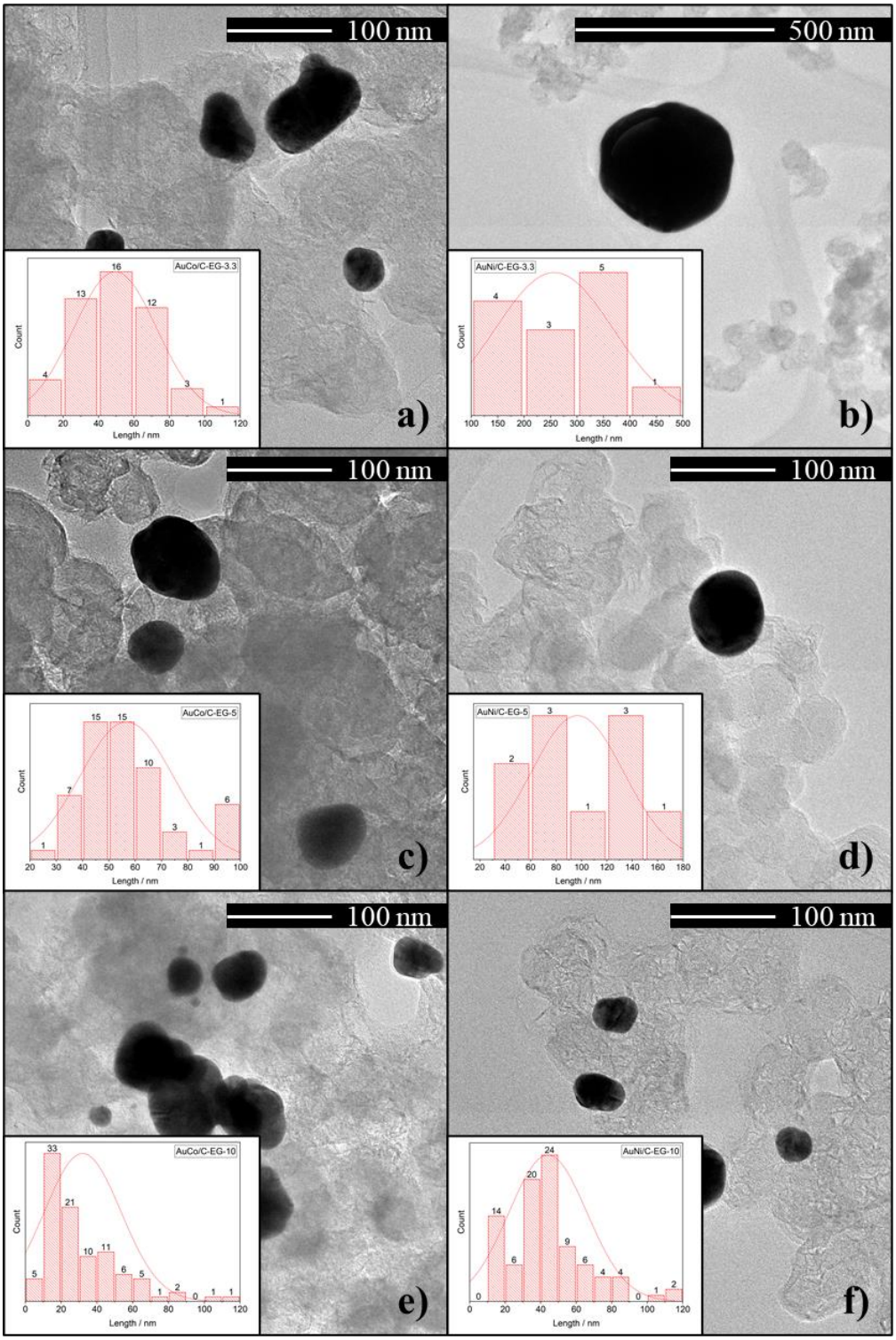

Figure 6. TEM images and particle size distribution of a) AuCo/C-EG-3.3, b) AuNi/C-EG-3.3, c) AuCo/C-EG-5, d) AuNi/C-EG-5, e) AuCo/C-EG-10, and f) AuNi/C-EG-10.

The decrease in the diameters of the particles is linked to the increase of the volume of the precursor solution, as in that case, the concentration of the ions decreases[73]. Ethylene glycol is a polyalcohol with three hydroxyl groups that can act as stabilization agents avoiding the nanoparticle stacking[74]. That is why, even though the materials obtained with EG-stabilization synthesis have large average sizes, they are not so agglomerated.

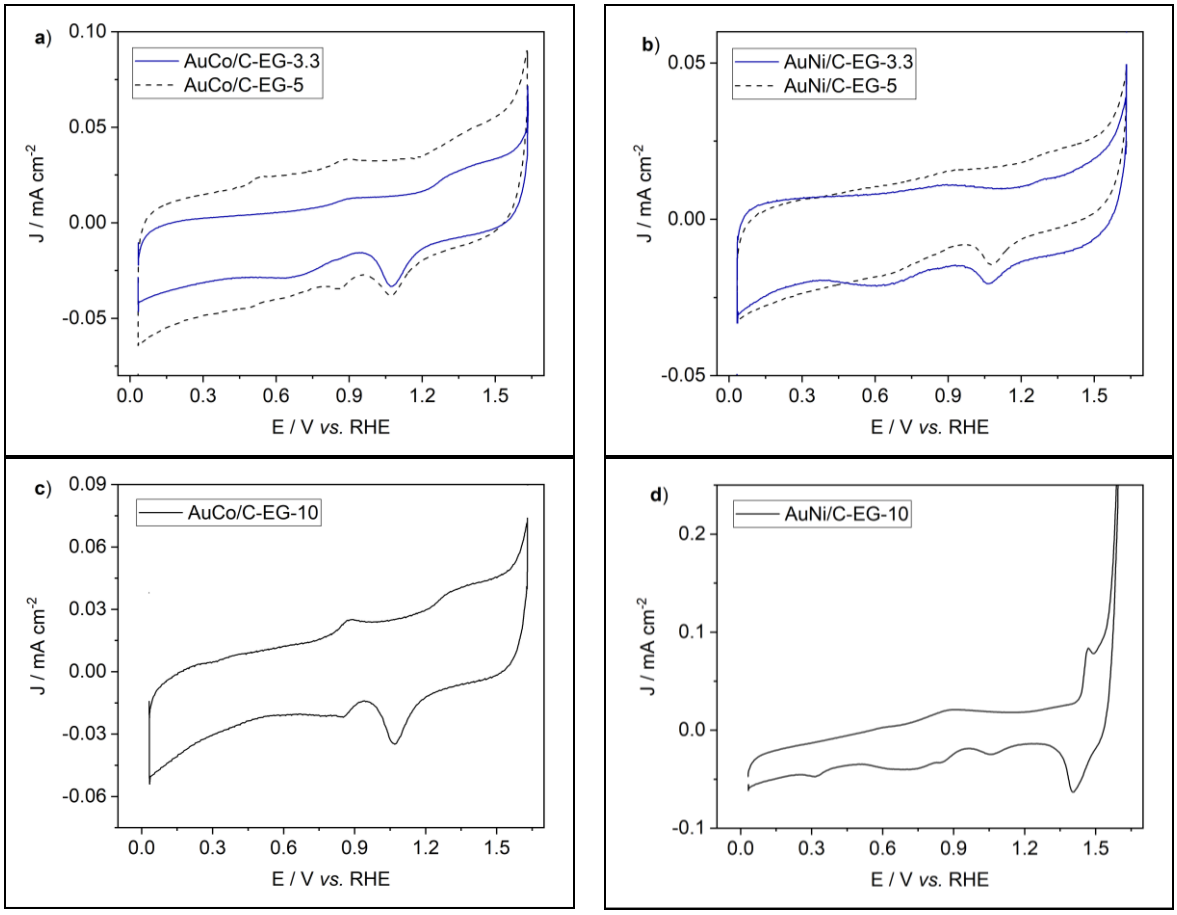

Figure 7. Cyclic voltammograms of a) AuCo/C-EG-3.3 (blue line) and AuCo/C-EG-5 (dashed black line), b) AuNi/C-EG-3.3 (blue line) and AuNi/C-EG-5 (dashed black line), c) AuCo/C-EG-10, and d) AuNi/C-EG-10. Recorded in Ar-saturated 0.1 M KOH at 50 mV s^{-1}.

The electrochemical behavior of the electrocatalyst was first tested in three-electrode cell configuration. Figure 7 displays the cyclic voltammogram recorded in alkaline

media. In all cases, it is feasible to notice current peaks corresponding to gold oxidation on the forward (positive) scan (a broad and slight peak at 1.29 V *vs.* RHE), and its reduction on the reverse (negative) scan at around 1 V *vs.* RHE.

In figures 7a and 7c it can also be noticed the presence of current peaks located at 0.53 V and 0.89 V *vs.* RHE, that are assigned to cobalt species on the surface. In addition, figure 7d shows a pair of redox peaks at 1.55 V *vs.* RHE in the forward scan related to the conversion of β-$Ni(OH)_2$ to NiOOH, and its reduction at 1.41 V *vs.* RHE in the reverse scan. This shows that for this material, the amount of Ni present is sufficient to have surface nickel atoms on the AuNi particles, the Ni atoms being in the form of (oxy)hydroxides.

Integrating the area of the gold oxide reduction (around 1 V *vs.* RHE) enables the determination of gold ECSA (in these calculations, it was considered that the particles had a density close to that of pure gold, which seems reasonable admitting their Au-rich composition – Table 3).

Table 3 shows that the active areas oscillate between 1.54 and 3.92 $cm^2\ g^{-1}_{Au}$, somewhat smaller than for other works[61-64], in agreement with the large particles size (and/or non-negligible extent of agglomeration, for some samples).

To evaluate the ethylene glycol-prepared material's electrocatalytic activity towards the ORR, hydrodynamic polarization plots were acquired in the rotating disk electrode setup. Figure 8 displays the RDE polarization curves in alkaline media at 5 $mV\ s^{-1}$. It is possible to notice a faradic reaction starting at different potentials (around 0.8 V *vs.* RHE), corresponding to the oxygen reduction reaction. The curves for the various revolution rates of the RDE show well-defined limiting currents, highlighting that the ORR at these catalysts is mass-transport limited at sufficiently large overpotential

values; on the contrary, at low overvoltage, the curves are all superposed, signing the charge transfer limitation, which enables accessing the intrinsic ORR kinetics of the materials.

Table 3 summarizes the values of the two kinetics markers chosen in this work: the onset potential (potential measured for a faradaic current density of -0.1 mA cm^{-2} on the ORR polarization plot recorded at 1600 rpm), and half-wave potential (potential when the current is the half of the limiting current, on the plot at 1600 rpm).

As it is known, the onset potential (E_{onset}) and the Gibbs free energy are closely related. The more positive the starting potential, the more negative the Gibbs free energy[75]. Table 3 highlights that the ORR is thermodynamically favored in the following descending order: AuNi/C-EG-10 > AuCo/C-EG-10 > AuCo/C-EG-3.3 > AuCo/C-EG-5 > AuNi/C-EG-5 > AuNi/C-EG-3.3.

The half-wave potential ($E_{1/2}$) is also a good marker of the ORR kinetic activity, its value being independent of the analyte concentration. Table 3 indicates that the AuCo/C-EG-10 has the most positive value of $E_{1/2}$: 0.612 V *vs.* RHE among the EG-synthesized materials. The materials, in descending order of the $E_{1/2}$, are AuCo/C-EG-10 > AuNi/C-EG-10 > AuCo/C-EG-3.3 > AuCo/C-EG-5 > AuNi/C-EG-5 > AuNi/C-EG-3.3.

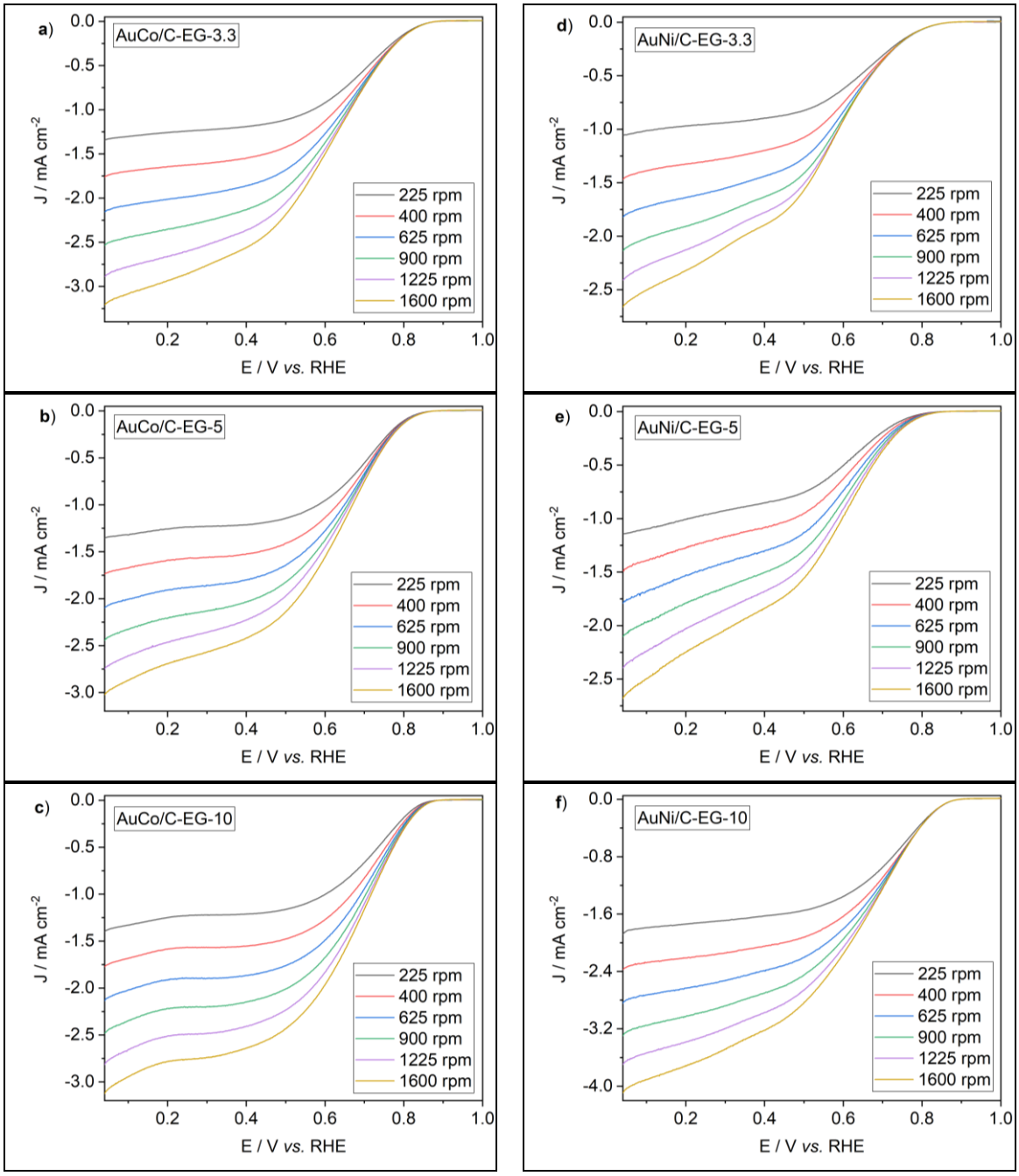

Figure 8. RDE polarization curves of a) AuCo/C-EG-3.3, b) AuCo/C-EG-5, c) AuCo/C-EG-10, d) AuNi/C-EG-3.3, e) AuNi/C-EG-5, and f) AuNi/C-EG-10 at different rotating speeds. Recorded in O_2-saturared 0.1 M KOH at 5 mV s^{-1}.

Table 3 Summary of ECSA ($cm^2\ g^{-1}Au$), Eonset (V), and $E_{1/2}$ (V) *vs.* RHE with standard deviation of EG-synthesized materials

Electrocatalyst	ECSA / $cm^2\ g^{-1}_{Au}$ ± SD	E_{onset} / V *vs.* RHE ± SD	$E_{1/2}$ / V *vs.* RHE ± SD
AuCo/C-EG-3.3	3.02 ± 0.15	0.824 ± 0.008	0.582 ± 0.001
AuCo/C-EG-5	2.95 ± 0.14	0.783 ± 0.005	0.566 ± 0.011
AuCo/C-EG-10	3.92 ± 0.33	0.827 ± 0.006	0.612 ± 0.006
AuNi/C-EG-3.3	1.67 ± 0.19	0.745 ± 0.015	0.556 ± 0.006
AuNi/C-EG-5	1.54 ± 0.11	0.768 ± 0.027	0.565 ± 0.013
AuNi/C-EG-10	3.38 ± 0.29	0.833 ± 0.004	0.606 ± 0.006

The electrocatalytic stability of the materials is also an essential parameter for practical applications. Figure 9 shows the CV and ORR polarization curves at 1600 rpm, before and after the ADT of AuCo/C-EG-10 and AuNi/C-EG-10. As shown in figures 9a and 9c, the current peaks related to the redox pairs of Co and Ni suffered a loss in intensity, indicating leaching of these transition metals. Besides, it was observed losses of 12% and 21% in the active areas (of gold) of AuCo/C-EG and AuNi/C-EG, respectively, signing a possible corrosion of the particles upon the ADT.

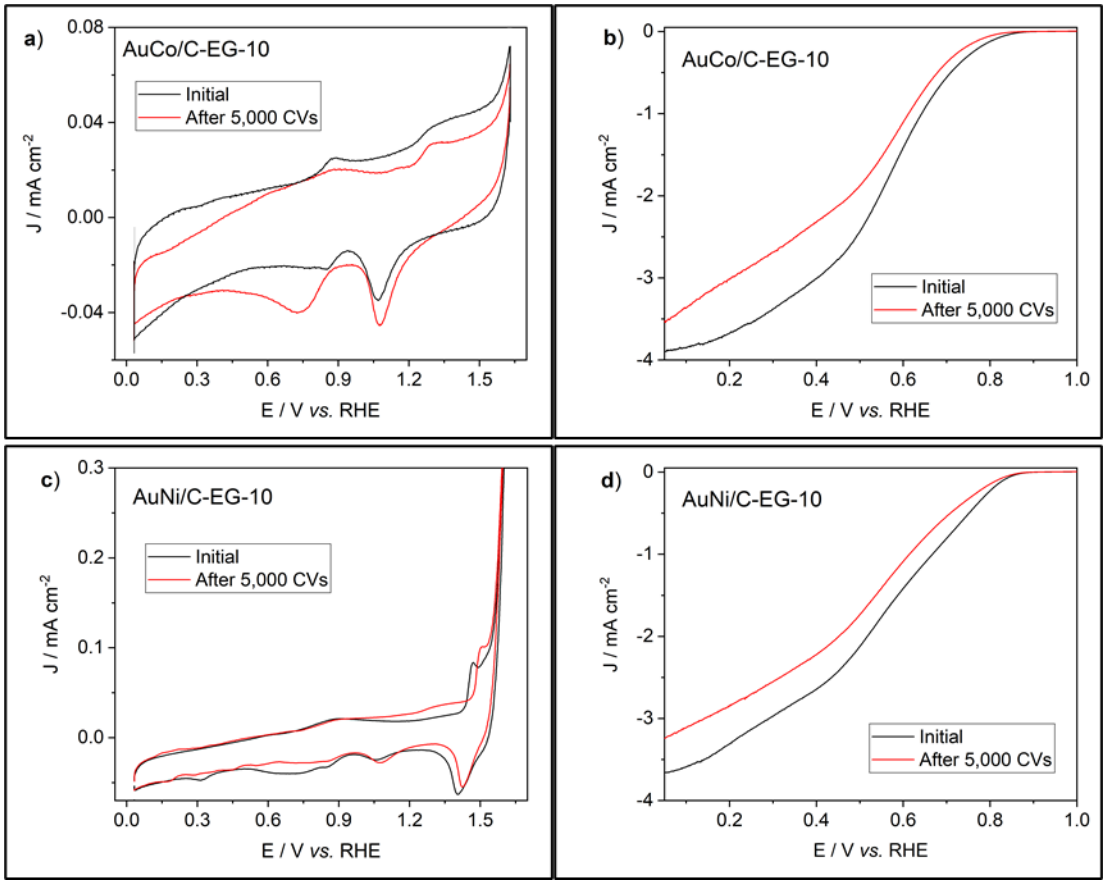

Figure 9. Comparison of ORR activities of AuCo/C-EG-10 and AuNi/C-EG-10 before and after 5,000 CVs; a) CV curves of AuCo/C-EG-10, b) RDE polarization curves at 1600 rpm of AuCo/C-EG-10, c) CV curves of AuNi/C-EG-10, d) RDE polarization curves at 1600 rpm of AuNi/C-EG-10.

*All CVs were recorded in Ar-saturated 0.1 M KOH at sweep rate of 50 mV s^{1}. All RDE polarization curves were recorded in O_2-saturated 0.1 M KOH at sweep rate of 5 mV s^{-1}.

As illustrated in Figure 9b, after the 5,000 cycles of ADT, the AuCo/C-EG-10 material does not well retain its catalytic activity: it shows 54 and 43 mV negative shifts for E_{onset} and $E_{1/2}$, respectively. On the other hand, as shown in Figure 9d, the AuNi/C-EG electrocatalyst better keeps its catalytic activity; it presented negative shifts of 16 and 32 mV for E_{onset} and $E_{1/2}$, respectively. This enhanced stability of the Ni-containing sample

originates from the considerably more positive Nernst potential for Ni than for Co, making Ni more stable to corrosion[76].

Figure 10 shows the 4f core-level (CL) spectra of AuNi/C-EG-10 initial, and AuNi/C-EG-10 after 5,000 cycles of ADT. Pure gold (red-dashed line, see figure 24) displays a doublet at binding energies of 88.1 and 84.5 eV, which are assigned to Au $4f_{5/2}$ and Au $4f_{7/2}$, respectively, and both corresponds to zero-valent Au^0 [77-78]. After the alloying with Ni, the AuNi/C-EG-10 CL spectrum shows two sharp peaks located at binding energies of 88.0 and 84.3 eV related to Au $4f_{5/2}$ and Au $4f_{7/2}$, respectively. This negative shift in the binding energy proves that the AuNi/C-EG-10 exists in nanoalloy form[79]. More critical, previous works showed that these shifts in the binding energy indicate a change in the d-band structure of Au[80-81]. When the CL shifts to lower values, the d-band center presents a positive shift of the Fermi level, which will result in a better adsorption of oxygen-containing species onto the gold surface and better electrocatalytic activity towards the ORR[82-83], being admitted that pure Au does not bind oxygen enough strongly to be really ORR active. After the 5,000 cycles of ADT, the CL of AuNi/C-EG shifted to more positive values than those for AuNi/C-EG, explaining the decrease in the electrocatalytic activity.

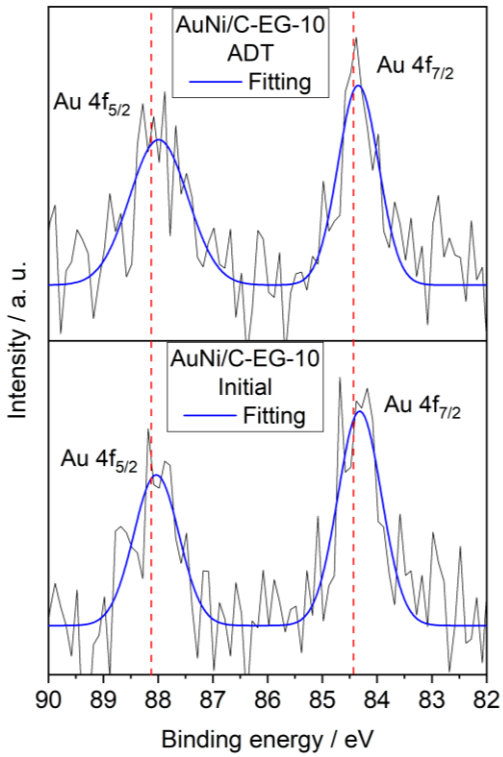

Figure 10. XPS Au 4f spectra of AuNi/C-EG-10 initial, and AuNi/C-EG-10 after 5,000 cycles of ADT. The red-dashed line corresponds to the binding energies of the Au/C-HT.

At this point, it is possible to see that best results were achieved with the AuNi/C-EG-10, the nanoalloy with the largest content of transition metal. That is why it was decided to continue with the characterization of the materials with a theoretical similar amount of transition metal than the above nanoalloy.

3.2 Carbon-supported nanoalloys prepared via stirring method

Starting with the crystallographic characterization, the picture changes for the stirring method. In figure 11a (AuFe/C-S) it is possible to distinguish a diffraction signal located at 35.77° in 2θ that is indexed with the {311} family of planes of Fe_2O_3 Maghemite (red arrow); this phase could have been formed, because in the synthesis the appropriate conditions were applied: alkaline media and oxidizing atmosphere (before adding the reducing agent). Also, the Fe precursor was in high concentration[84-85].

Figure 11b (AuCo/C-S) displays a reflection at 18.97° in 2θ that is indexed with the {001} family of planes of β-$Co(OH)_2$. Figure 11c (AuNi/C-S) highlights a diffraction peak at 19.14° in 2θ that corresponds to the {001} crystallographic planes of $Ni(OH)_2$. Due to the pK_s values for $Co(OH)_2$ and $Ni(OH)_2$ (14.8 and 14.7, respectively[86]), those phases are susceptible to being formed when the pH of the solution is adjusted to alkaline values, this to prevent the $NaBH_4$ from forming H_2 gas.

Besides the above signals, in all samples it is possible to notice a diffraction peak at 26.6° in 2θ that corresponds to the {002} family of planes of graphite. As expected, all samples crystallized in a typical face-centered cubic structure (FCC), and have the reflections located at 38.17°, 44.37°, 64.55°, 77.53°, and 81.69° in 2θ that are assigned to {111}, {200}, {220}, {311}, and {222} crystallographic planes of Au.

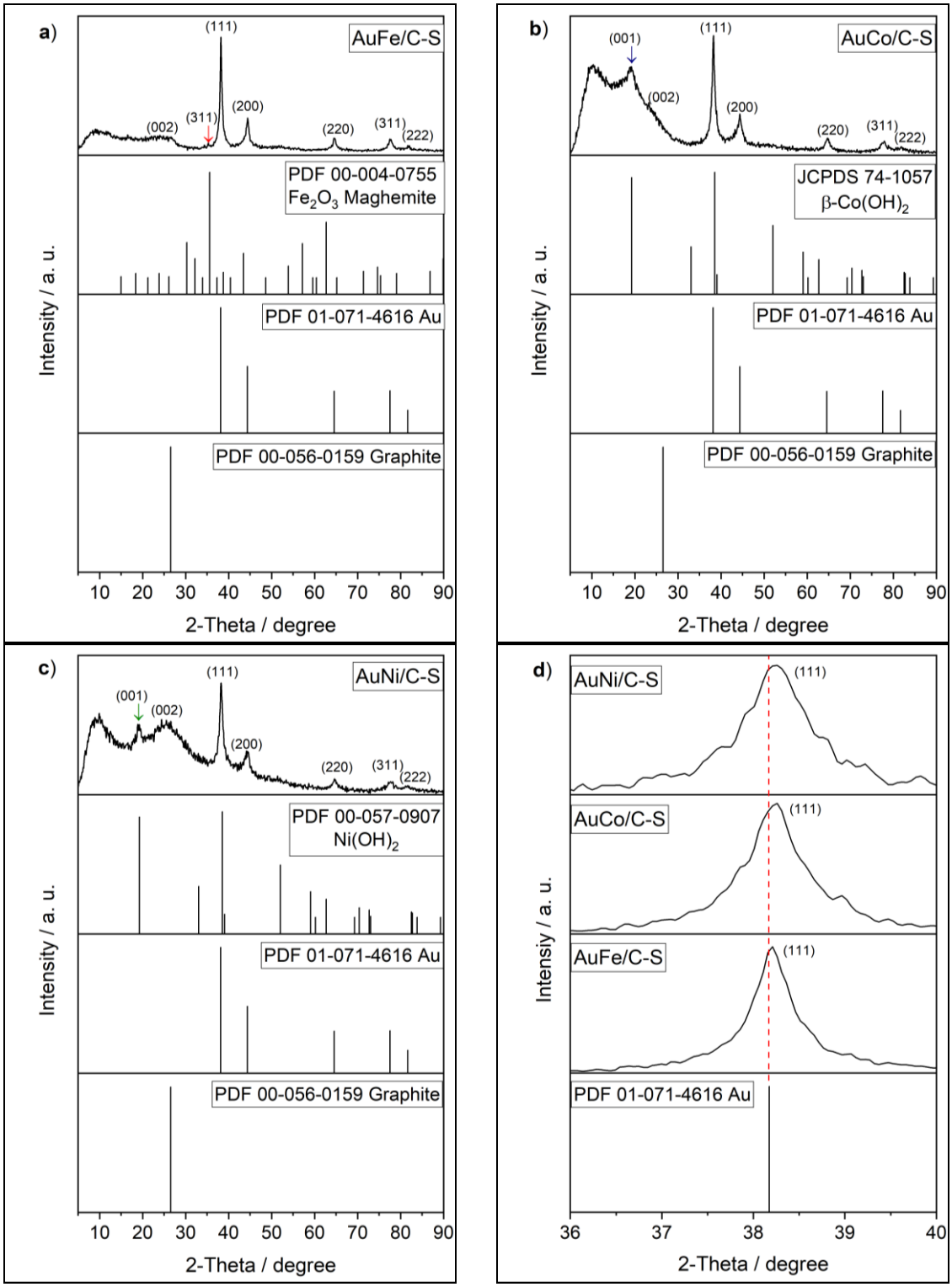

Figure 11. X-ray diffraction patterns of a) AuFe/C-S, b) AuCo/C-S, and c) AuNi/C-S nanoalloys prepared; and d) zoom of the diffraction patterns.

Zooming between 36° and 40° in 2θ (figure 11d) shows that the diffraction peak angles for the (111) family of planes in AuFe/C-S, AuCo/C-S, and AuNi/C-EG-10 were slightly higher compared to pristine Au. This can be explained because iron (1.72 Å), cobalt (1.67 Å), and nickel (1.62 Å) have atomic ratio smaller than gold (1.79 Å). Also, wider peaks are observed for AuCo/C-S and AuNi/C-S than that for AuFe/C-S, indicating that the crystallinity decreased more due to the presence of Co and Ni than Fe. The above situation can be explained because Au, Co, and Ni have face-centered cubic structure, while Fe has body-centered cubic structure[87].

Vegard's Law calculations revealed that Au:Fe/C-S 99.09:0.01, Au:Co/C-S 99.1:0.9, and Au:Ni/C-S 99.5:0.5 nanoalloys were formed.

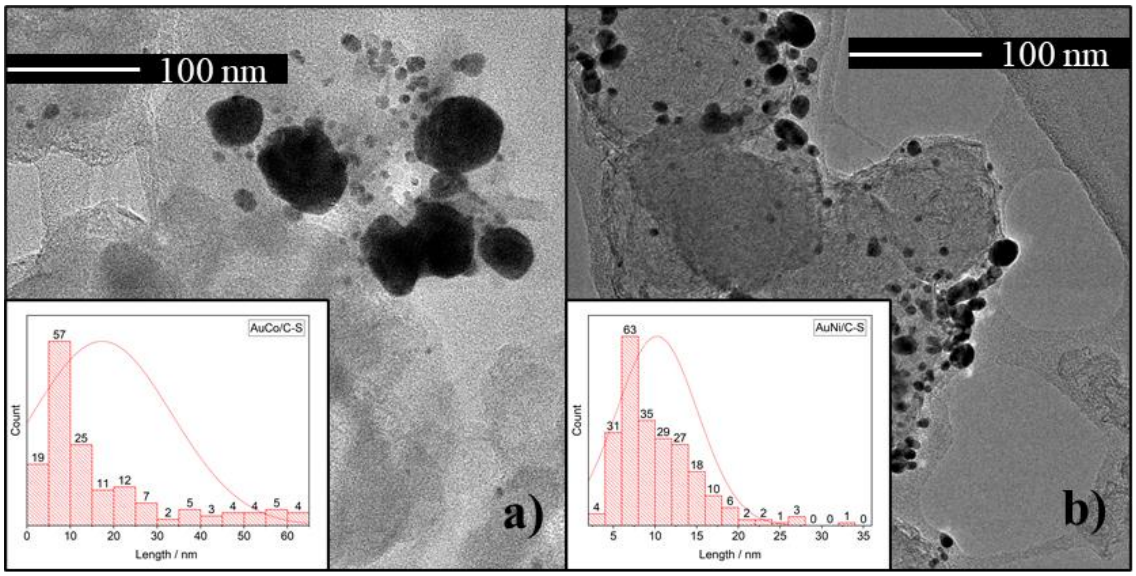

Figure 12. TEM images and particle size distribution of a) AuCo/C-S, b) AuNi/C-S.

Figure 12 shows TEM micrographs of AuCo/C-S and AuNi/C-S. The nanoparticles have a near-spherical morphology, and some agglomerates. In figure 12a it is noticed that 64% of the AuCo/C-S particles have significant lower diameters: less than 15 nm, with mean of 17 nm ± 16 nm (15 nm by Scherrer). On the other hand, figure 12b displays that

89% of the AuNi/C-S particles have diameters less than 15 nm, and an average of 10 nm ± 5 nm (13 nm by Scherrer).

X-EDS chemical analysis (not shown here) revealed that chemical compositions are not homogeneous for the samples, the smallest particles correspond to Co-rich or Ni-rich phases, and the largest to Au-rich phases. These M-rich phases are probably composed by β-$Co(OH)_2$ or $Ni(OH)_2$ in majority, in agreement with the XRD data presented above.

Figure 13 presents the electrochemical profiles of the materials prepared via stirring at room-temperature. All the voltammograms showed a current peak at around 1 V *vs.* RHE in the reverse scan, related with the reduction of gold oxide.

In figure 13a (AuFe/C-S), it is feasible to notice a wide peak at 0.2 V *vs.* RHE that some authors relate with a pre-oxidation of the material. Figure 13b (AuCo/C-S) shows a current peak at 1.29 V *vs.* RHE, which is related to the conversion of $Co(OH)_2$ to CoOOH. Finally, in figure 13c (AuNi/C-S) it is possible to see a pair of redox peaks at 1.54 V *vs.* RHE in the forward scan related to the conversion of $Ni(OH)_2$ to NiOOH, and its reduction at 1.41 V *vs.* RHE in the reverse scan.

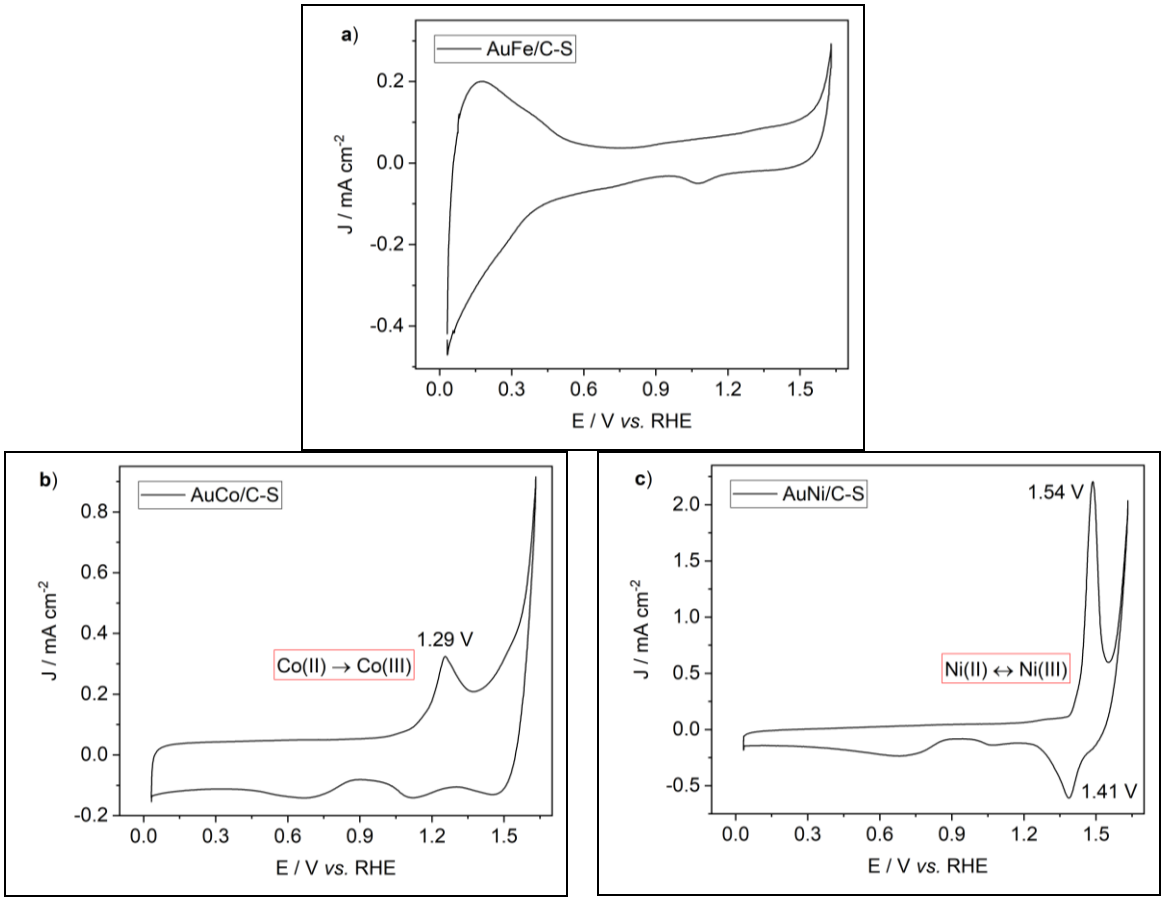

Figure 13. Cyclic voltammograms of a) AuFe/C-S, b) AuCo/C-S, and c) AuNi/C-S. Recorded in Ar-saturated 0.1 M KOH at 50 mV s^{-1}.

The next step was to evaluate the activity of the electrocatalyst towards the oxygen reduction reaction. For that, Figure 14 shows the RDE polarization curves recorded in O_2-saturated 0.1 M KOH at different rotating speeds. All the materials showed the typical behavior, and three regions can be distinguished: the non-faradaic region, the mixed region, and the mass-transport limited region.

Figure 14d is a comparison between the onset potentials for the ORR, and the values are enlisted in the table 4.

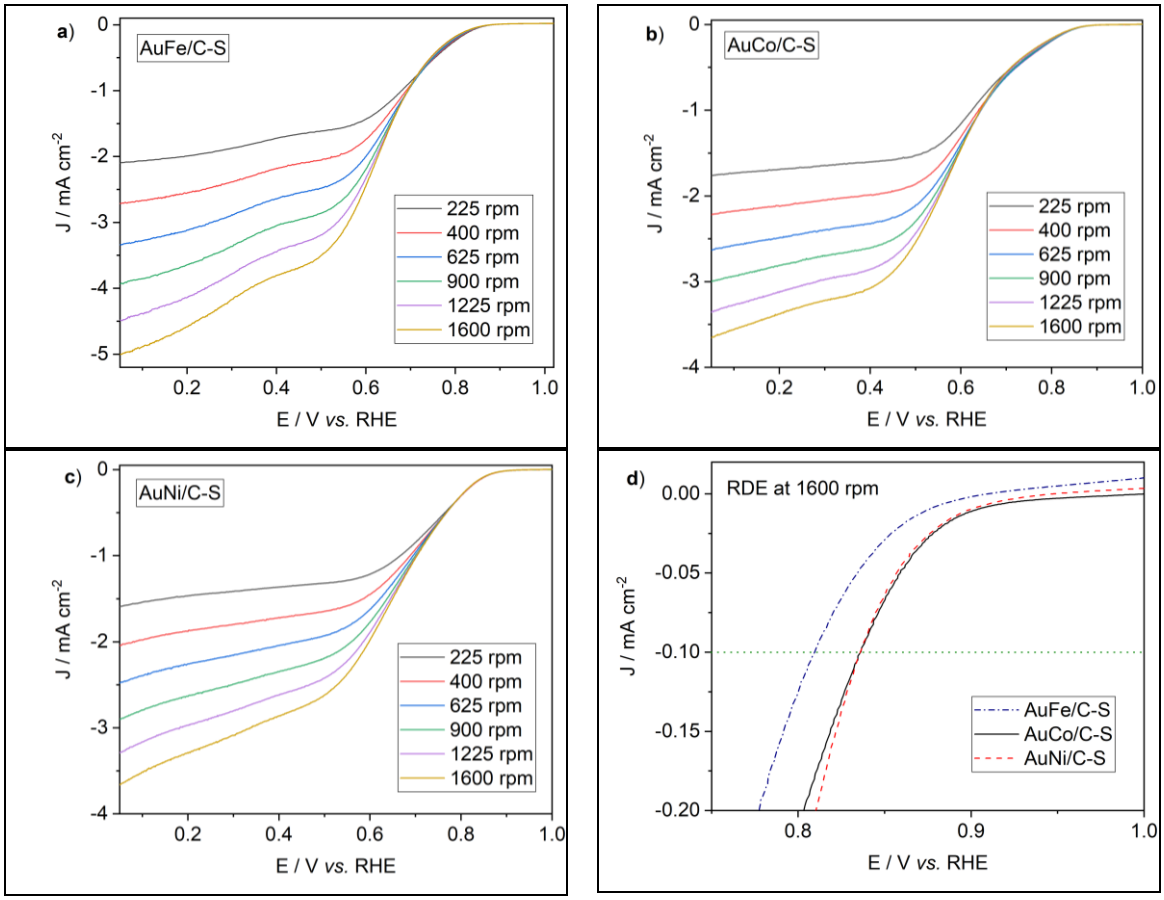

Figure 14. RDE polarization curves of a) AuFe/C-S, b) AuCo/CS, and c) AuNi/C-S at different rotating speeds. d) zoom of the RDE at 1600 rpm. Recorded in O_2-saturared 0.1 M KOH at 5 mV s^{-1}.

By comparing the onset potentials, it is feasible to observe that the thermodynamical ORR activity decreases in the following order: AuNi/C-S ≥ AuCo/C-S > AuFe/C-S.

If now the half-wave potentials are compared, the picture changes a bit since the kinetic ORR activity decreases in the following order: AuNi/C-S > AuFe/C-S > AuCo/C-S.

Table 4. Summary of active area (cm^2), E_{onset} (V), and $E_{1/2}$ (V) *vs.* RHE with standard deviation of S-synthesized materials

Electrocatalyst	Active area / cm^2 ± SD	E_{onset} / V *vs.* RHE ± SD	$E_{1/2}$ / V *vs.* RHE ± SD
Au:Fe/C-S 99.09:0.01	0.090 ± 0.009	0.807 ± 0.003	0.618 ± 0.009
Au:Co/C-S 99.1:0.9	0.485 ± 0.023	0.835 ± 0.009	0.580 ± 0.006
Au:Ni/C-S 99.5:0.5	0.291 ± 0.011	0.839 ± 0.004	0.643 ± 0.001

To have a better comparison of the electrocatalytic activity between the materials, Koutecky-Levich graphs were built (figure 15a, 15b, and 15c) by plotting the inverse of the current values as function of the inverse of the square root of the rotation speed, at different values of potential.

By lineal regression, it is possible to determine the intercept which is equal to the inverse of the kinetic density current. Then, the J_k (mA cm^{-2}) can be calculated. Figure 15d shows the J_k *versus* potential variation. With all the information so far, it is possible to observe that the ORR electrocatalytic activity decreases in the following order: AuNi/C-S > AuFe/C-S > AuCo/C-S.

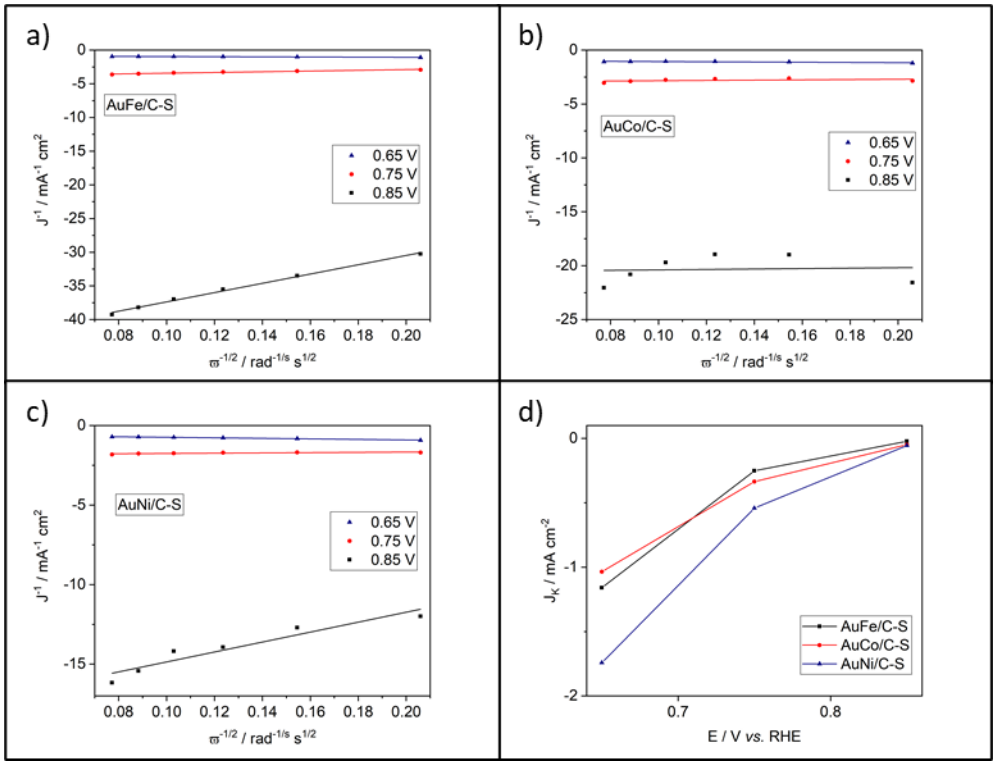

Figure 15. Koutecky-Levich plots at different potentials of a) AuFe/C-S, b) AuCo/C-S, and c) AuNi/C-S. d) Kinetic current (J_K) at different potentials of the above materials.

After making the accelerated degradation tests, as shown in figures 16a, 16c, and 16e, the current peaks related to the pre-oxidation of Fe, as well as the redox pairs of Co and Ni suffered losses in intensity, indicating leaching of these transition metals.

Figure 16b showed that AuFe/C-S did not suffer appreciable losses in terms of onset potential and half-wave potential. On the other hand, in figure 16d it is possible to see that AuCo/C-S lost 43 mV of its onset potential, and 32 mV of its half-wave potential. Finally, AuNi/C-S (figure 16f) lost 78 mV of its onset potential and 34 mV of its half wave potential.

These results show that all the materials have poor electrocatalytic activity towards the oxygen reduction reaction. Also, if their performance is compared against the Au/C-HT electrocatalyst (figure 21, and table 5 in the next section), none of them surpassed it.

With the above in mind, in the next section, it was decided to carry out the characterization of carbon-supported AuFe, AuNi, and AuNi nanoalloys prepared via the hydrothermal method.

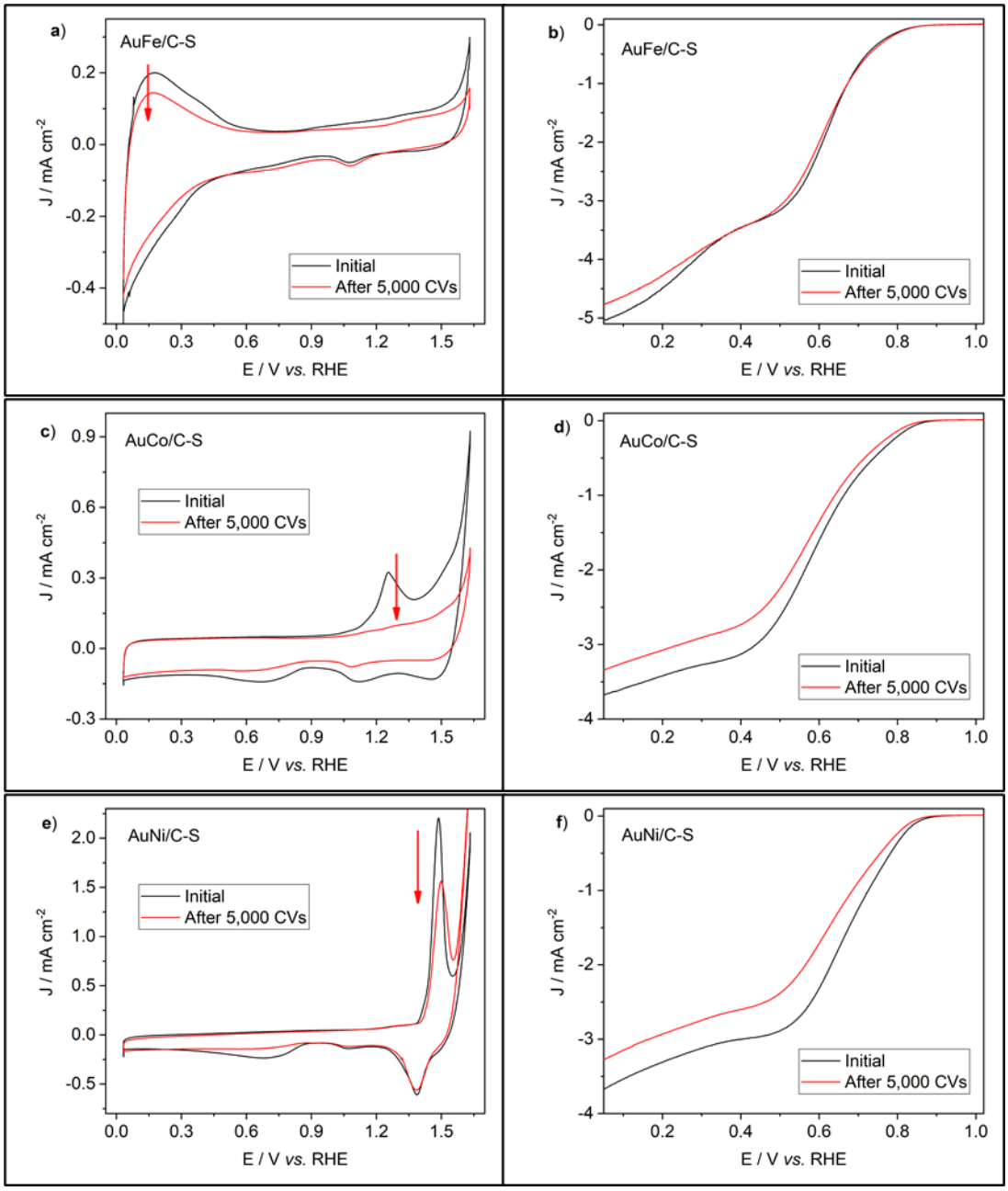

Figure 16. Comparison of ORR activities before and after 5,000 CVs of: a) CV curves of AuFe/C-S, b) RDE polarization curves at 1600 rpm of AuFe/C-S. c) CV curves of AuCo/C-S, d) RDE polarization curves at 1600 rpm of AuCo/C-S. e) CV curves of AuNi/C-S, f) RDE polarization curves at 1600 rpm of AuNi/C-S.

*All CVs were recorded in Ar-saturated 0.1 M KOH at sweep rate of 50 mV s^{-1}. All RDE polarization curves were recorded in O_2-saturated 0.1 M KOH at sweep rate of 5 mV s^{-1}.

3.3 Carbon-supported nanoalloys prepared via hydrothermal method

To have a reference point and compare the electrocatalytic activity of all materials, Au/C was synthesized via the hydrothermal method.

Figure 17 shows the C-supported nanoalloys prepared via hydrothermal. First, in figure 17a it is feasible to observe that Au/C-HT crystallized in the typical FCC-structure, and almost all the diffraction signals are attributed to pure gold, which indicates that no impurities are present (at least not above at 5 wt.%). The only reflection other than gold is the peak at 26.6° in 2θ that corresponds to the {002} family of planes of graphite from the carbon support.

Figures 17b, 17c, and 17d present the same reflections mentioned above. In addition, they show the diffraction signals related to Fe_2O_3 Maghemite (figure 17b), β-$Co(OH)_2$ (figure 17c), and $Ni(OH)_2$ (figure 17d). All the signals are indexed with the corresponding card.

It is worth to notice that in the case of hydrothermal prepared materials, the diffraction signals corresponding to gold and oxidized secondary phases of the transition metals are more intense than those on the stirring room-temperature prepared materials. The above may be due to the pressure and temperature conditions reached in the hydrothermal reactor, that favored the crystallinity.

Zooming between 36° and 40° in 2θ, as it is shown in figure 18, it is possible to notice that the diffraction peak angles for the (111) family of planes were slightly higher compared to pristine Au. This phenomenon was explained before. In a similar way to the intensity of signals, the shift towards higher angles was greater in the hydrothermal-prepared materials than the stirring-prepared materials.

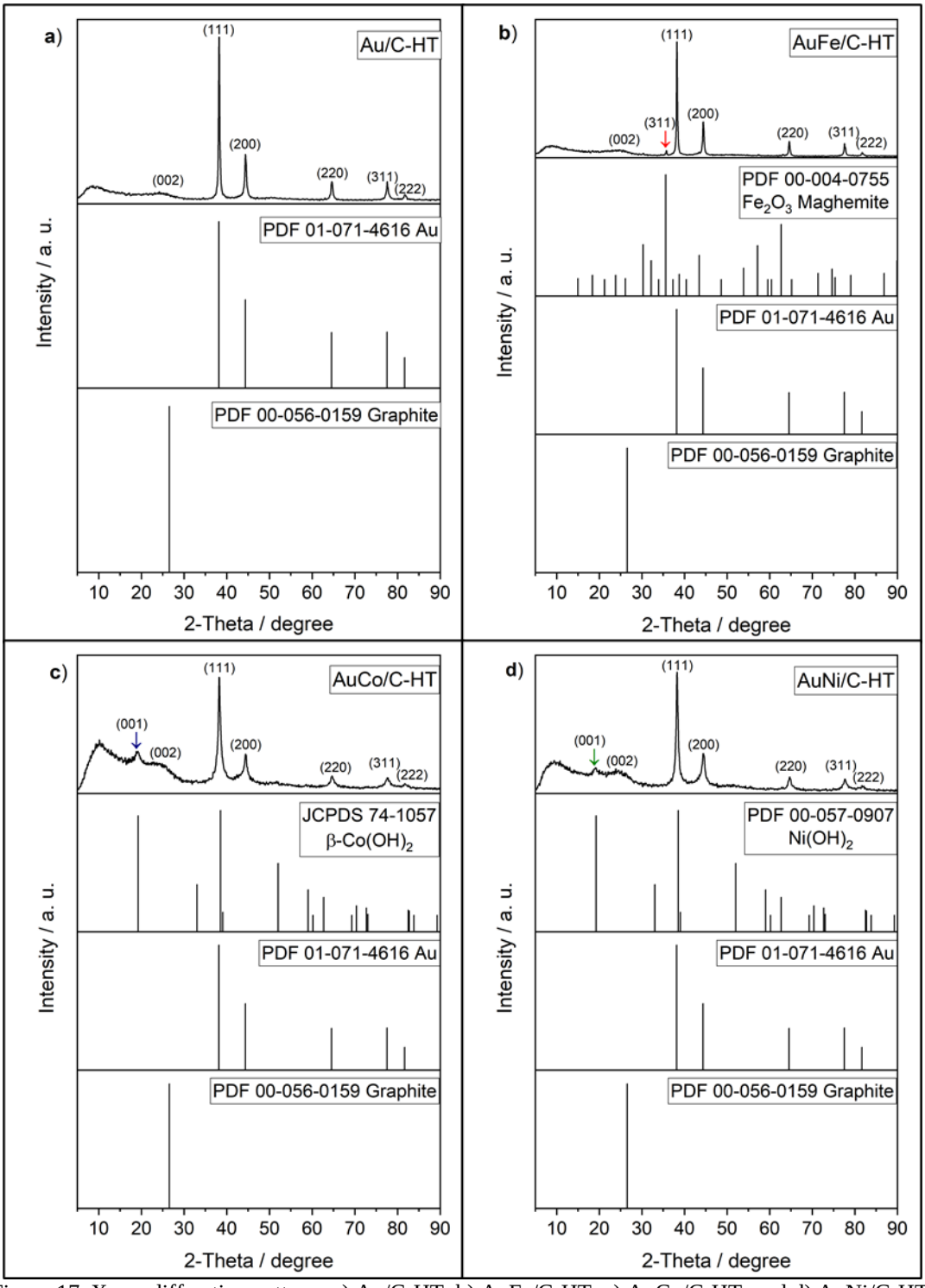

Figure 17. X-ray diffraction patterns a) Au/C-HT, b) AuFe/C-HT, c) AuCo/C-HT, and d) AuNi/C-HT.

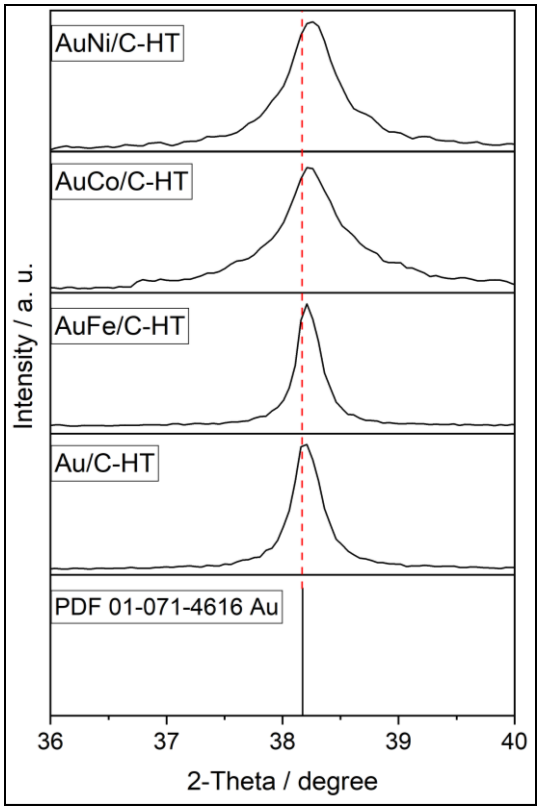

Figure 18. X-ray diffraction patterns of Au/C-HT, AuFe/C-HT, AuCo/C-HT, and AuNi/C-HT

With Vegard's Law calculations, Au:Fe/C-HT 99.05:0.05, Au:Co/C-HT 99:5:0.5, and Au:Ni/C-HT 99.1:0.9 nanoalloys were prepared. As discussed before, Fe has a BCC-type structure, while Au, Co, and Ni have FCC-type structure, that is why Fe was the least incorporated metal into Au's lattice (and with the least positive Nernst reduction potential). Ni, having the more positive Nernst reduction potential, among the transition metals used here, was the metal most incorporated into Au's lattice.

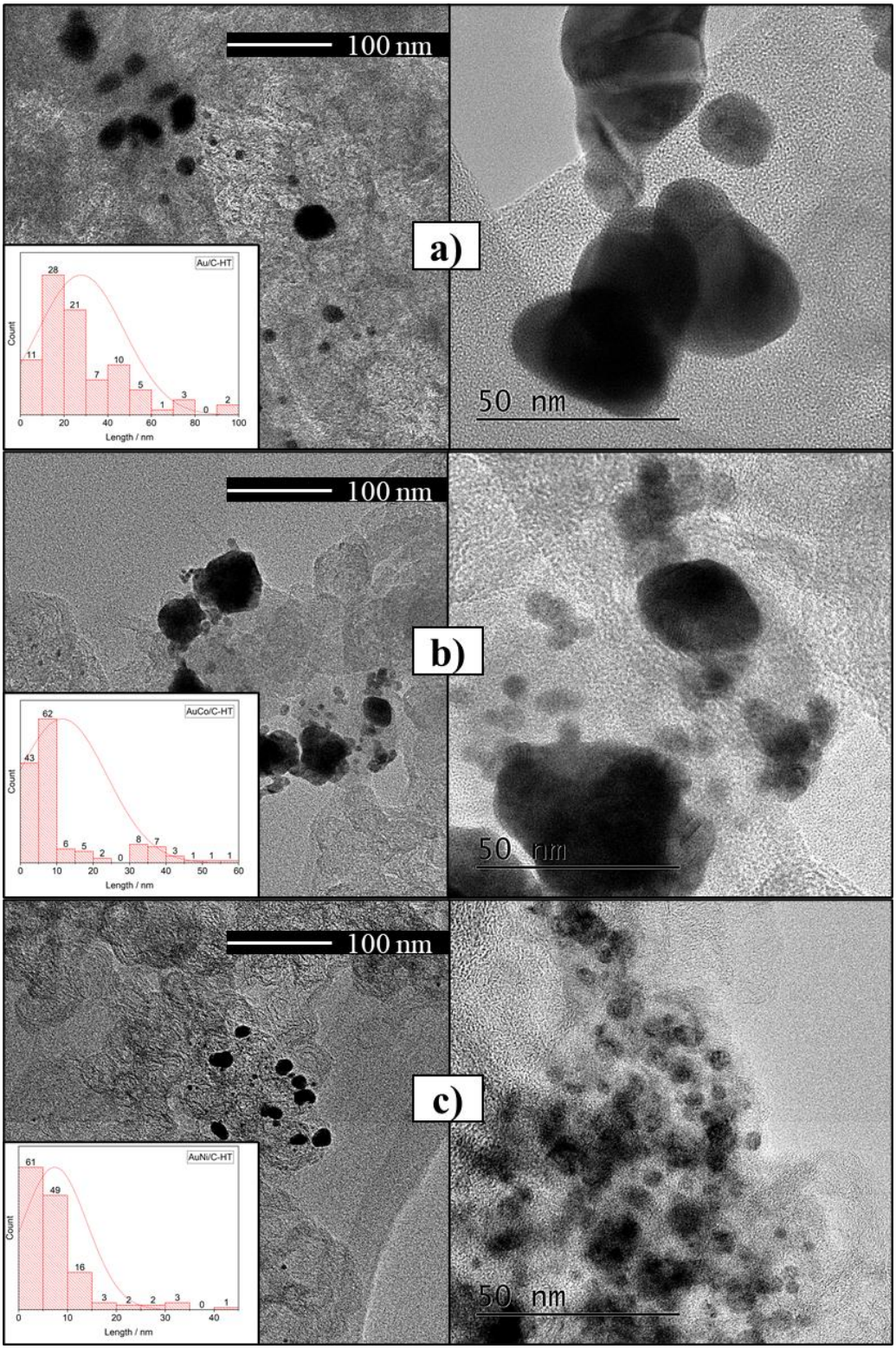

Figure 19. TEM images and particle size distribution a) Au/C-HT, b) AuCo/C-HT, c) AuNi/C-HT.

Morphological characterization of Au/C-HT, AuCo/C-HT, and AuNi/C-HT materials were carried out by transmission electron microscopy coupled with energy dispersive X-ray spectroscopy.

As shown in figure 19, all the particles have a near-spherical morphology, and there is some agglomeration. Figure 19a is the micrograph of Au/C-HT, where it is feasible to see that 66% of the particles have diameters lower than 30 nm, with an average of 28 nm ± 20 nm (32 nm by Scherrer). Even though the average particle size measured with TEM is smaller than the average crystallite size calculated with Scherrer equation, if compared along with the standard deviation, the diameter distribution is larger.

Figure 19b shows larger and darker particles, around which there are smaller and lighter particles. The average diameter was determined to be 17 nm ± 16 nm (18 nm by Scherrer). X-EDS analysis (not shown here) shows that the larger particles are Au-rich, and the smaller ones are Co-rich (probably composed mainly of β-$Co(OH)_2$).

Something similar is observed in figure 19c, most of the diameters are smaller than 10 nm, with a mean of 7.4 nm ± 6.7 nm (19 nm by Scherrer). This discrepancy comes from the fact that there are Au-rich larger and darker particles, and Ni-rich smaller and lighter particles. As it has the lowest particle size, this catalyst material is expected to have good results as electrocatalyst for the ORR.

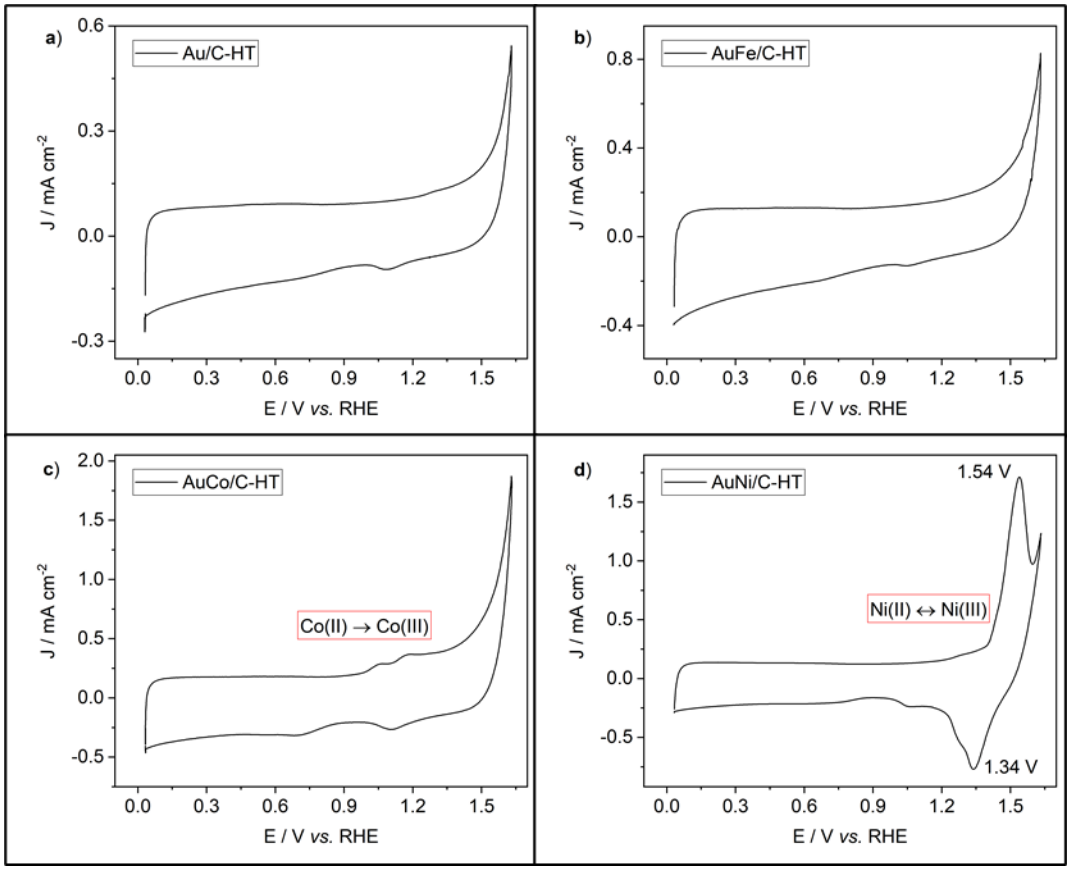

Figure 20. Cyclic voltammograms of a) Au-C-HT, b) AuFe/C-HT, c) AuCo/C-HT, and d) AuNi/C-HT. Recorded in Ar-saturated 0.1 M KOH at 50 mV s^{-1}.

The electrochemical profiles of hydrothermal-synthesized materials are shown in figure 20. The four materials showed the gold-oxide reduction peak at 1 V *vs.* RHE in the reverse scan. As shown in figures 20a and 20b, Au/C-HT and AuFe/C-HT did not show other faradaic events in the potential window used. On the contrary, in figures 20c and 20d it is possible to see current peaks related with the redox pairs Co(II)/Co(III), and Ni(II)/Ni(III), respectively.

Table 5 shows that the HT-prepared materials have larger active area compared with S-prepared materials. The above agrees with the results obtained by TEM.

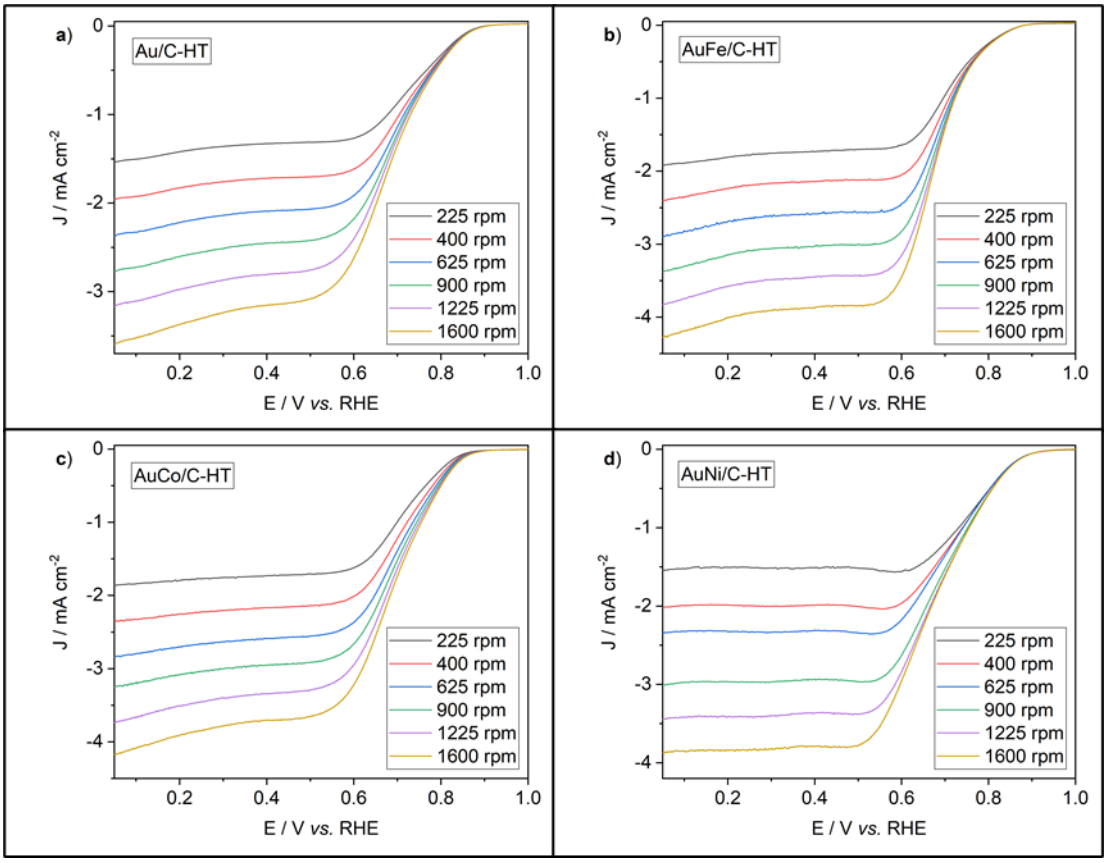

Figure 21. RDE polarization curves of a) Au/C-HT, b) AuFe/C-HT, c) AuCo/C-HT, and d) AuNi/C-HT at different rotating speeds. Recorded in O_2-saturared 0.1 M KOH at 5 mv s^{-1}.

Figure 21 displays the typical hydrodynamic ORR voltammetry. All the plots are near-symmetric sigmoid-shaped waves, with a near-flat limiting current plateau after the wave. This already indicates that these catalysts lead to more evident mass-transfer limitation at large overpotential, sign of their better ORR activity than for the previous samples. Markers of table 5 confirm this qualitative observation: all the nanoalloys have better electrocatalytic activity towards the oxygen reduction reaction than for the previous catalysts and compared with pure gold.

The ORR is thermodynamically favored in the following ascending order: Au/C-HT < AuFe/C-HT < AuCo/C-HT < AuNi/C-HT. Also, the ORR is kinetically favored in the following ascending order: Au/C-HT < AuNi/C-HT < AuFe/C-HT < AuCo/C-HT.

Table 5. Summary of active area (cm^2), E_{onset} (V), and $E_{1/2}$ (V) *vs.* RHE with standard deviation of HT-synthesized materials

Electrocatalyst	Active area / cm^2 ± SD	E_{onset} / V *vs.* RHE ± SD	$E_{1/2}$ / V *vs.* RHE ± SD
Au/C-HT	0.163 ± 0.020	0.847 ± 0.012	0.640 ± 0.004
Au:Fe/C-HT 99.05:0.05	0.125 ± 0.008	0.850 ± 0.007	0.675 ± 0.001
Au:Co/C-HT 99.5:0.5	0.697 ± 0.036	0.864 ± 0.005	0.697 ± 0.010
Au:Ni/C-HT 99.1:0.9	0.509 ± 0.007	0.874 ± 0.007	0.663 ± 0.015

The Koutecky-Levich analysis allows to obtain kinetic parameters for a redox sluggish reaction, as it is the case for the ORR[88]. With data from figure 21, one can plot the current values as a function of the inverse of the square root of the rotation speed, at different values of potential, leading to the Koutecky-Levich plots of figure 22.

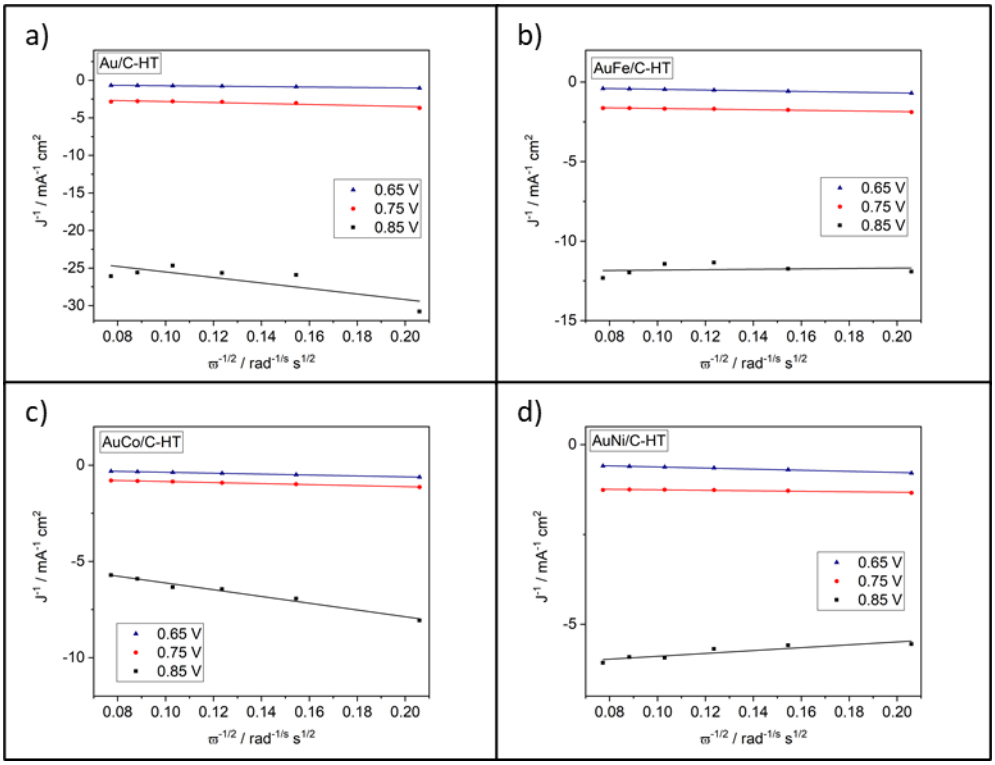

Figure 22. Koutecky-Levich plots at different potentials of a) Au/C-HT, b) AuFe/C-HT, c) AuCo/C-HT, and c) AuNi/C-HT.

Once the K-L plots were obtained, extrapolating the line to 0, which corresponds to a theoretical infinite rotation speed, it enables to evaluate the inverse of the electronic transfer current (kinetic current, J_k), in other words, the current that would be obtained if there was absolutely no limitation by mass-transport. As it can be feasible to see in figure 23a, all nanoalloys presented a larger kinetic density current than pure gold, meaning that the electroreduction of oxygen is kinetically favored on their surface. The best result was obtained with the Co-containing nanoalloy, which is in agreement with the kinetics results observed with the half-wave potential (table 5).

The current on a ring electrode concentric to the disk electrode was also measured, and the following equation was used to calculate the number of electrons transferred during the reaction (equation 9):

$$ne^- = \frac{4|I_D|}{|I_D| + \frac{I_R}{N}}$$ Equation 10

where, $|I_D|$ is the absolute value of the current measured at the disk, I_R is the current measured at the ring, and N is the collection efficiency (the fraction of the material from the disk which flows past the ring electrode). In this work, the collection efficiency prescribed by the supplier was used, which is 0.25.

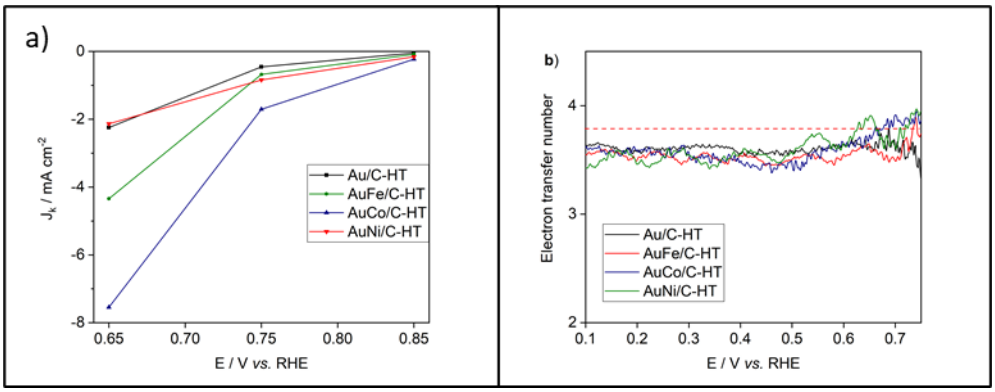

Figure 23. a) Calculated kinetic density currents (J_K) and b) number of electrons transferred of materials prepared via hydrothermal method.

As it is seen in figure 23b, the ORR in all the nanoalloys proceeds via a pseudo-4e- pathway, since the #e- is lower than 3.8. This situation can stem from two mains reasons: (i) the density of nanoparticles at the carbon surface is low (there are large areas of carbon not covered by AuM nanoparticles), carbon leading to a 2-electron ORR[98]; and (ii) the M content of the AuM nanoparticles is low, and the behavior of Au (which leads to 2-electron ORR) is not negligible.

To better understand the enhancement in the electrocatalytic activity of gold by alloying with transition metals, X-ray photoelectron spectroscopy was performed. Figure 24

shows that the binding energies of Au $4f_{5/2}$, and Au $4f_{7/2}$ shifted to lower values after the alloying process (Au/C-HT: Au $4f_{5/2}$ 88.1 eV and Au $4f_{7/2}$ 84.5 eV; Au:Fe/C-HT: Au $4f_{5/2}$ 88.1 eV and Au $4f_{7/2}$ 84.4 eV; Au:Co/C-HT: Au $4f_{5/2}$ 88.2 eV and Au $4f_{7/2}$ 84.2 eV; Au:Ni/C-HT: Au $4f_{5/2}$ 88.0 and Au $4f_{7/2}$ 84.4 eV). As previously explained, this change has been proven to cause a positive shift in the d-band center with respect to the Fermi level, which increases the chemisorption of O-containing species, and enhances the electrocatalytic activity towards the oxygen reduction reaction.

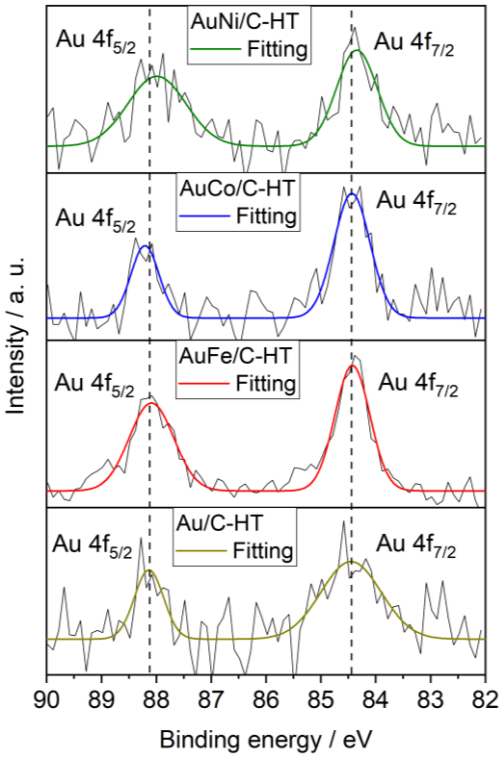

Figure 24. XPS Au 4f spectra of Au/C-HT (black line), AuFe/C-HT (red line), AuCo/C-HT (blue line), and AuNi/C-HT (green line).

Accelerated degradation tests on the hydrothermal-prepared materials were also performed by subjecting them at 5,000 cycles of CV in O_2-saturaed 0.1 M KOH electrolyte. The results are displayed in figures 25 and 26.

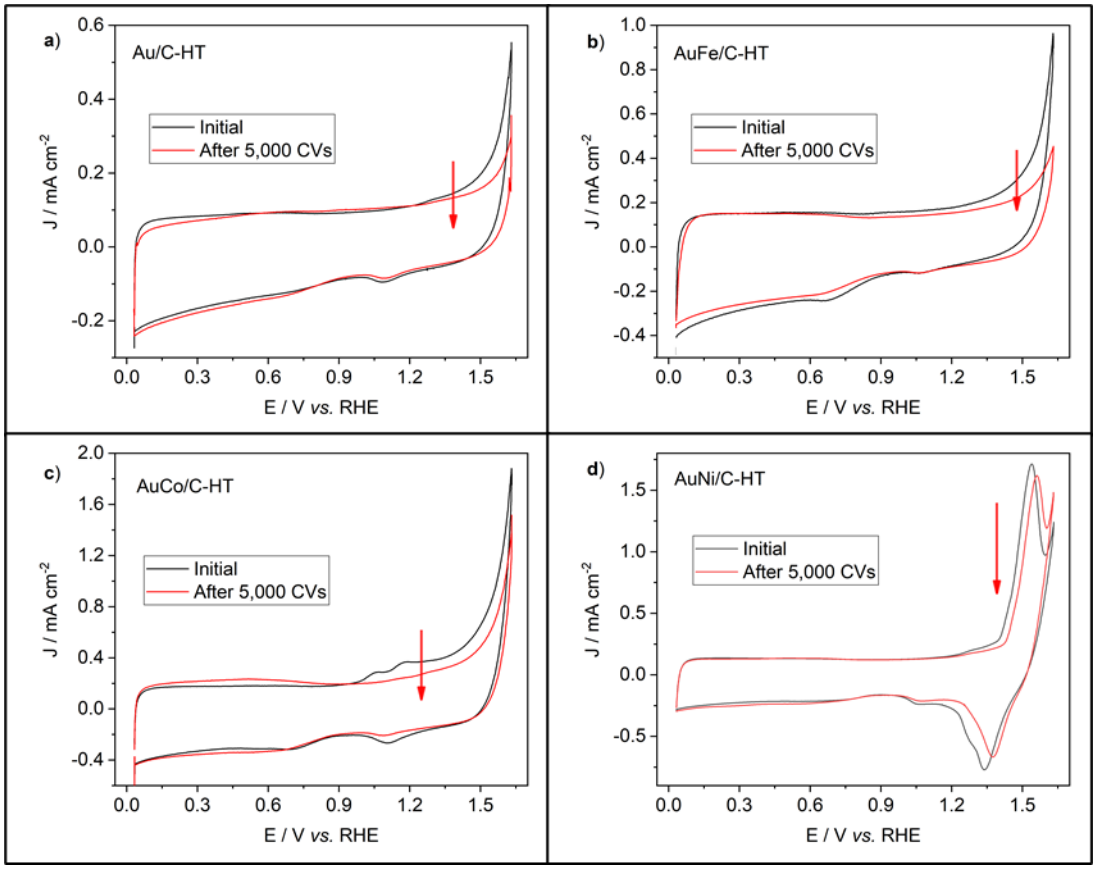

Figure 25. Comparison of electrochemical profiles before and after 5,000 CVs of: a) CV curves of Au/C-HT, b) CV curves of AuFe/C-HT, c) CV curves of AuCo/C-HT, d) CV curves of AuNi/C-HT.

*All CVs were recorded in Ar-saturated 0.1 M KOH at sweep rate of 50 mV s^{-1}.

As seen in figure 25, all the electrochemical profiles suffered losses in intensity after the ADT, which suggests ECSA loss or metal leaching into the solution, hence change in kinetics activity. Despite the metal leaching, as it is shown in figure 25b, AuFe/C-HT did not suffer significant loss of active area of gold. On the other hand, AuCo/C-HT and AuNi/C-HT lost 55 and 6 % of their active area.

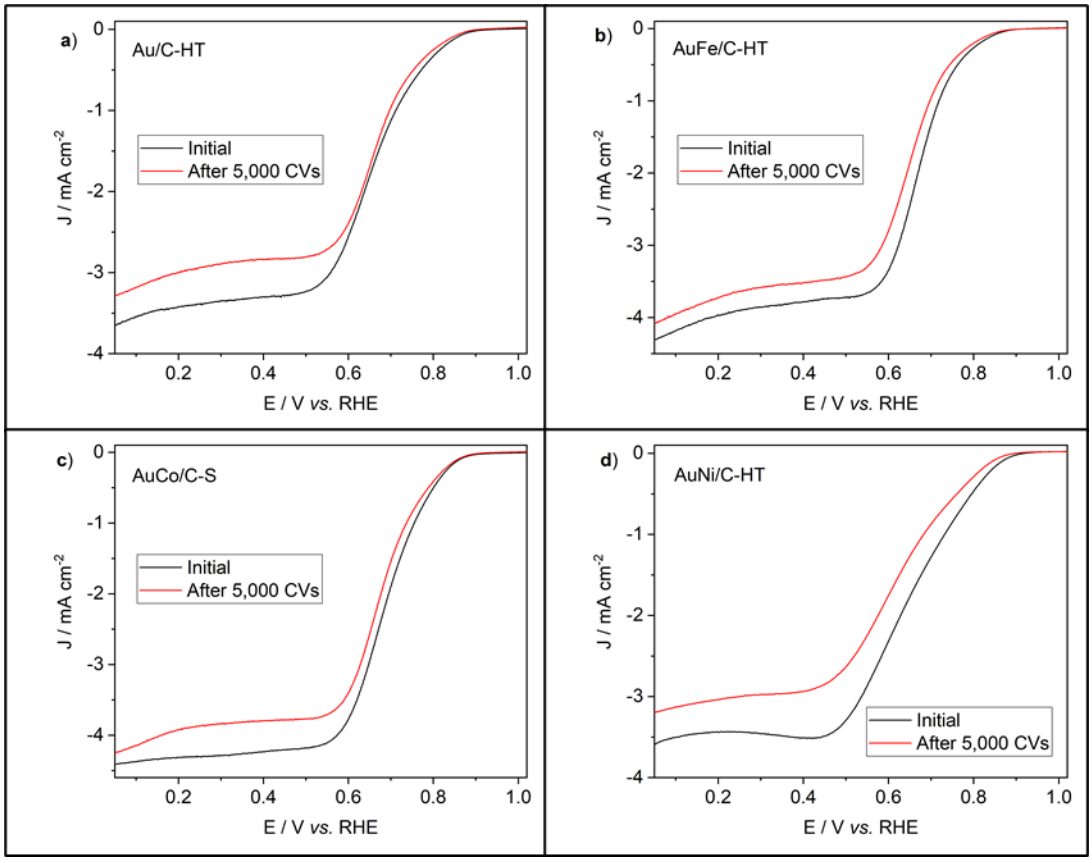

Figure 26. Comparison of ORR activities before and after 5,000 CVs of: a) RDE polarization curves at 1600 rpm of Au/C-HT, b) RDE polarization curves at 1600 rpm of AuFe/C-HT, c) RDE polarization curves at 1600 rpm of AuCo/C-HT, d) RDE polarization curves at 1600 rpm of AuNi/C-HT.

*All RDE polarization curves were recorded in O_2-saturated 0.1 M KOH at sweep rate of 5 mV s^{-1}.

Regarding the activity towards the oxygen reduction reaction, figure 26 shows the RDE polarization curves, at 1600 rpm, before and after the ADT. As expected, all the materials tested suffered negative shifts on their electrocatalytic parameters. To compare electrochemical and electrocatalytic activity of our materials, ADT was performed on a commercial electrocatalyst Pt/C 10 wt. %. These results are shown in figure 27.

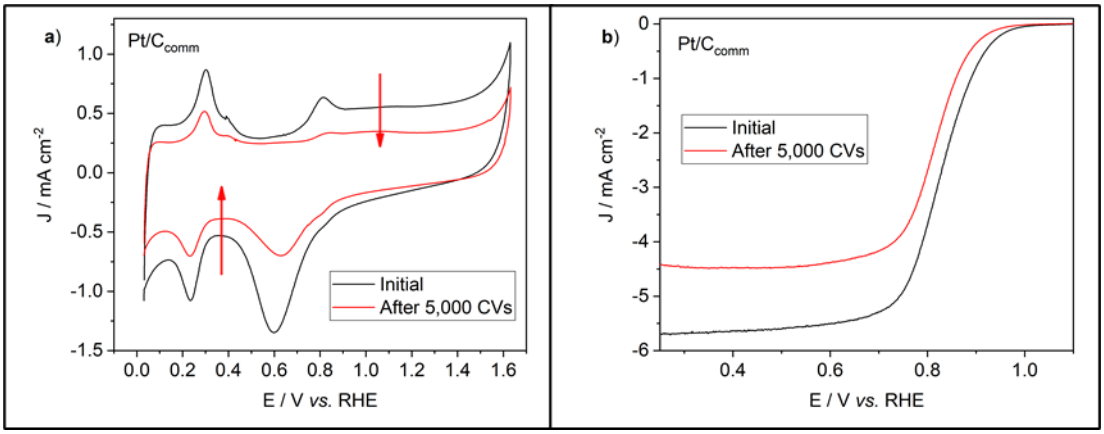

Figure 27. Accelerated degradation tests on Pt/C_{comm}. a) CV curves recorded in Ar-saturated 0.1 M KOH at 50 mV s^{-1}, b) RDE polarization curves at 1600 rpm in O_2-saturated 0.1 M KOH at 5 mV s^{-1}.

Table 6 **.** Summary of negative changes of E_{onset} (V) and $E_{1/2}$ (V) *vs.* RHE after 5,000 cycles of ADT.

Material	Change in E_{onset} (V)	Change in $E_{1/2}$ (V)
Au/C-HT	-0.006	-0.006
Au:Fe/C-HT 99.05:0.05	-0.022	-0.021
Au:Co/C-HT 99.5:0.5	-0.027	-0.025
Au:Ni/C-HT 99.1:0.9	-0.068	-0.044
Pt/C_{comm}	-0.030	-0.013

As it can be seen in table 6, the more stable material is Au/C. Nevertheless, it is also the worst electrocatalyst, between this group, towards the oxygen reduction reaction. The Au's stability probably comes from the fact that oxygen species are poorly chemisorbed on its surface. Even though the Pt/C_{comm} showed the third best stability, in figure 27b it is feasible to notice that the current limit, at 0.5 V *vs.* RHE, decreased around 1 mA cm^{-2}, the largest decrease among this electrocatalysts tested, a sign of non-negligible

degradation of this catalyst, likely by Pt-assisted carbon corrosion and further detachment of the Pt nanoparticles from the carbon surface, in line with earlier observations of Chatenet *et.al*[99-101].

Once it was verified that alloying Au with metals of transition metals has positive effects, and to improve the electrocatalytic activity of this kind on materials through a better morphological control, it was decided to carry out the synthesis of carbon-supported and AuNi nanoalloys via reverse micelle microemulsion. Those results are showed in the next section.

4.4 Carbon-supported nanoalloys prepared via reverse microemulsion method

Figure 28a shows the XRD patterns of AuNi/C-MO-ap and AuNi/C-MO-2h. The diffraction peaks located at around 38.17°, 44.37°, 64.55°, 77.53°, and 81.69° in 2θ are assigned to {111}, {200}, {220}, {311}, and {222} crystallographic planes of Au. The signal at 26.6° in 2θ corresponds to the {002} family of planes of graphite. There are not reflections related to Ni-oxides species. As the samples were analyzed in the form on dry electrochemical inks, the broad diffraction peak at 17° in 2θ corresponds to Nafion[89-90].

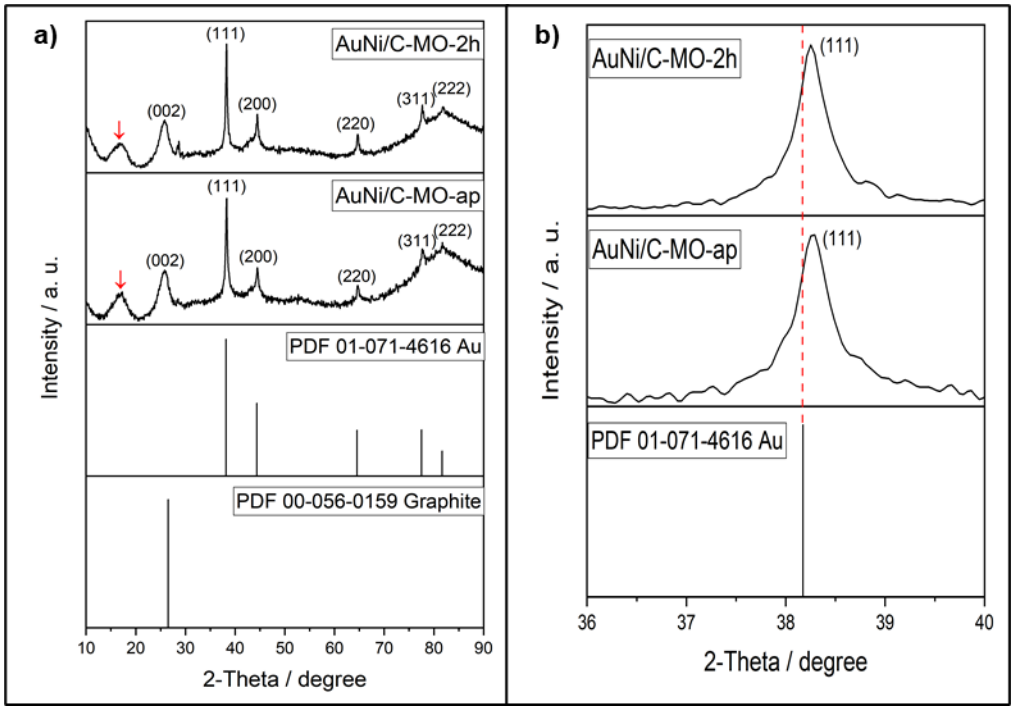

Figure 28. a) X-ray diffraction patterns of AuNi/C-MO-ap and AuNi/C-MO-2h, b) zoom.

As it can be seen in figure 28b, both materials, AuNi/C-MO-ap and AuNi/C-MO-2h suffered a positive shift in the diffraction peak of the {111} family of planes. The angles were 38.28° and 38.25°, respectively. The above indicate that after the heat treatment,

the large-order arrangement of Au got increased, and according to Vegard's Law, Au:Ni/C-MO-ap 98.1:1.9 and Au:Ni/C-MO-2h 98.7:1.3 were prepared.

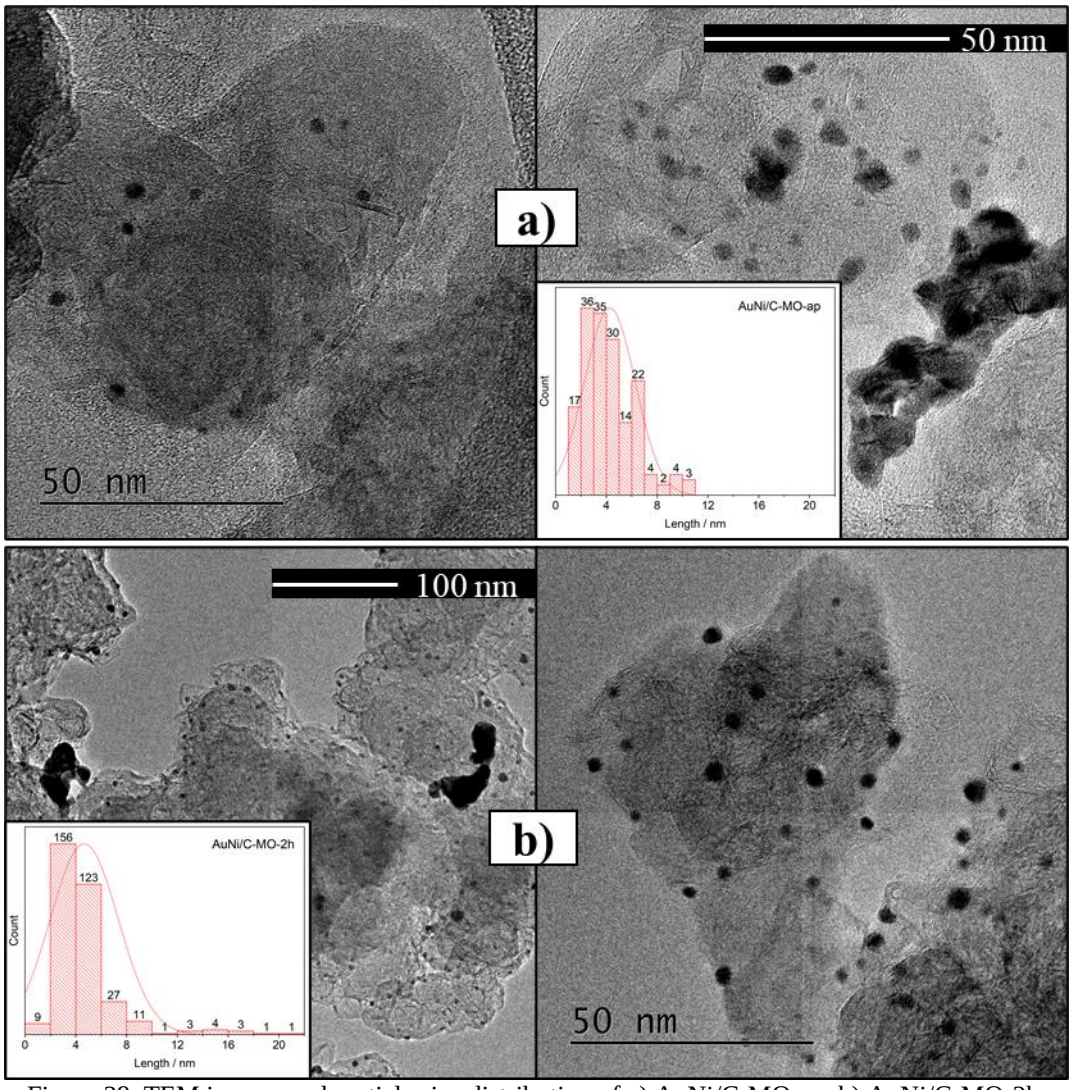

Figure 29. TEM images and particle size distribution of a) AuNi/C-MO-ap, b) AuNi/C-MO-2h.

As expected, the reverse micelle microemulsion method led to the formation of smaller particles with a better size distribution than previous methodologies. As shown in figure 29a, AuNi/C-MO-ap has an average of 4 nm ± 2 nm. In figure 29b it is possible to see that particles of AuNi/C-MO-2h suffered a sintering process after the heat treatment, that is why the average increased to 5 nm ± 3 nm.

Figure 30 displays the 4f core level of AuNi/C-MO-ap and AuNi/C-MO-h. It can be seen that Au $4f_{5/2}$ and Au $4f_{7/2}$ states suffered a negative shift in their binding energies (Au:Ni/C-MO-ap: Au $4f_{5/2}$ 88.1 eV and Au $4f_{7/2}$ 84.4 eV; Au:Ni/C-MO-2h: Au $4f_{5/2}$ 88.1 eV and Au $4f_{7/2}$ 84.4 eV) which indicates, again, that the d-band center of Au shifted to more positive values with respect to the Fermi level, evidencing the formation of the nanoalloy.

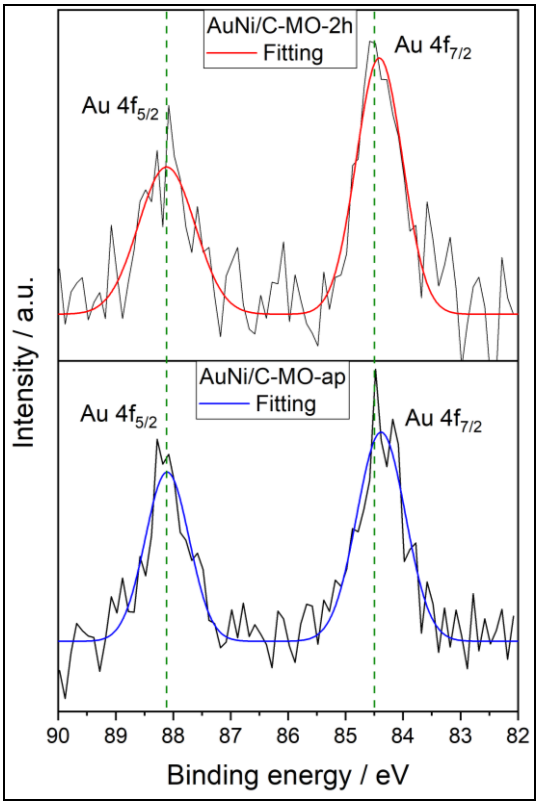

Figure 30. XPS Au 4f spectra of AuNi/C-MO-ap, and AuNi/C-MO-2h. The green-dashed line corresponds to the binding energies of the Au/C-HT.

In the electrochemical profiles, figure 31, it is feasible to see two redox processes. The first is the oxidation/reduction of Au(I) ↔ Au(0). The second redox pair is the conversion of $Ni(OH)_2$ to NiOOH, and vice versa.

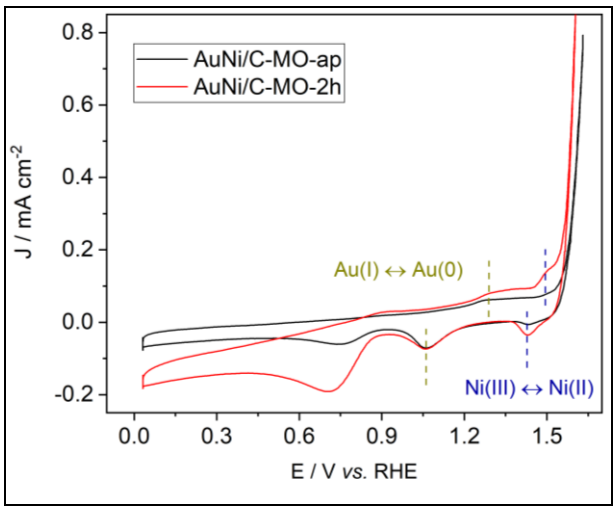

Figure 31. Cyclic voltammograms of AuNi-C-MO-ap and AuNi/C-MO-2h. Recorded in Ar-saturated 0.1 M KOH at 50 mV s^{-1}.

As it can be seen in figure 32 and table 7, the as-prepared AuNi/C nanoalloy have better onset potential than AuNi/C-MO-2h, probably because after the heat treatment the particle size increased, and the Ni content decreased (according to Vegard's Law). Also, after the heat treatment the active area decreased probably because of the increase in the particle size seen by TEM.

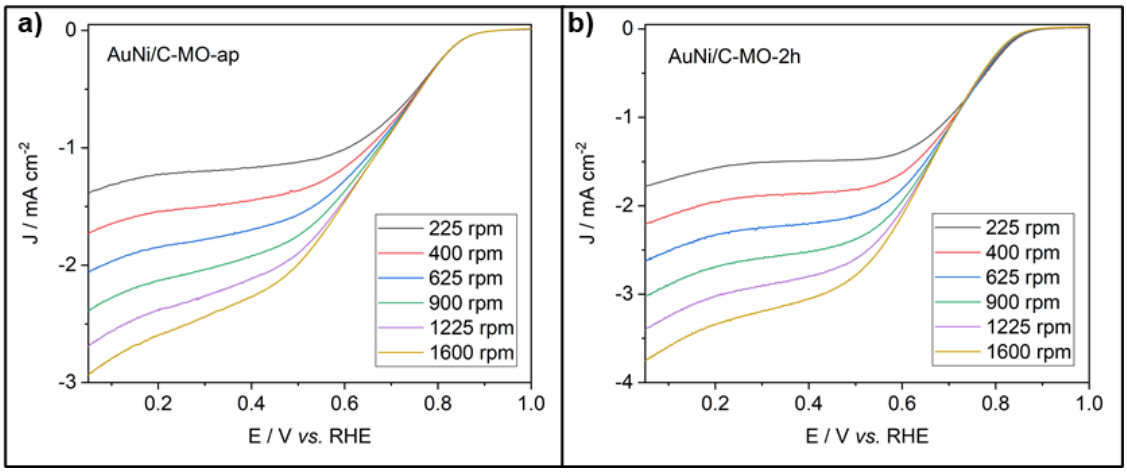

Figure 32. RDE polarization curves of AuNi/C-MO-ap, and AuNi/C-MO-2h. Recorded in O_2-saturared 0.1 M KOH at 5 mV s^{-1}.

Table 7 Summary of active area (cm^2), E_{onset} (V), and $E_{1/2}$ (V) *vs.* RHE with standard deviation of reverse micelle microemulsion-synthesized materials

Material	Active area / cm^2 ± SD	E_{onset} / V *vs.* RHE ± SD	$E_{1/2}$ / V *vs.* RHE ± SD
AuNi/C-MO-ap 98.1:1.9	0.142 ± 0.018	0.843 ± 0.003	0.632 ± 0.010
AuNi/C-MO-2h 98.7:1.3	0.126 ± 0.007	0.836 ± 0.008	0.646 ± 0.035

One interesting phenomenon is that even though the as-prepared AuNi/C-MO-ap nanoalloy has a more positive E_{onset} that AuNi/C-MO-2h, the heat-treated material has larger $E_{1/2}$ and limiting current, the above is probably because the larger particle size enhances the kinetics of charge transfer.

As seen in figure 33a, AuNi/C-MO-2h has larger kinetic currents that AuNi/C-MO-ap which agrees with the half-wave potential values observed. The above probes that the ORR kinetics were favored after the heat-treatment in the region where mass-transport is less limiting.

Figure 33b illustrates that the ORR proceeds via pseudo-four electron in AuNi/C-MO-ap and AuNi/C-MO-2h. Considering the standard deviation, it can be noticed that the reverse micelle microemulsion prepared materials have almost equal electrocatalytic activity towards the oxygen reduction reaction than Au/C-HT.

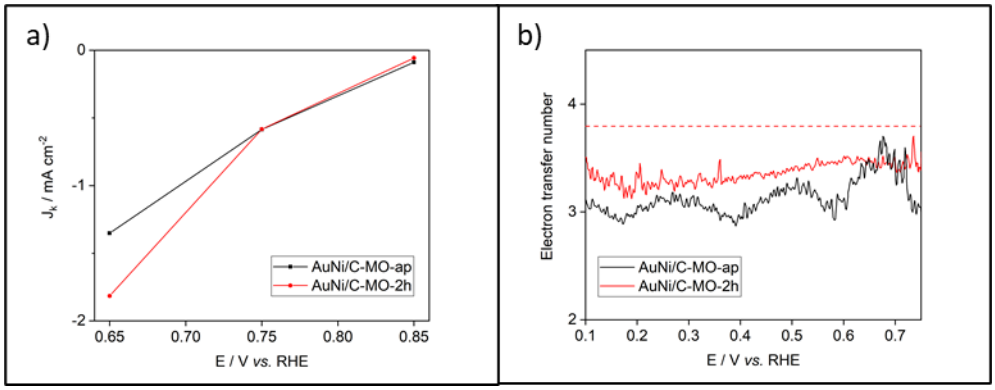

Figure 33. a) Calculated kinetic density currents (J_K) and b) number of electrons transferred of AuNi/C nanoalloys prepared via reverse microemulsion.

CHAPTER 4: CONCUSIONS

Since Au $4f_{5/2}$ and Au $4f_{7/2}$ bonding energies shifted to lower values, with respect to pure carbon-supported Au, it can be said that carbon-supported Au:Ni 94:6 (atomic ratio) nanoalloy was successfully prepared with the ethylene glycol-stabilization method.

To properly carry out the reduction of the metal ions, and form a nanoalloy, it is important to work in alkaline environments. Otherwise, the reducing agent is decomposed, and the TM-ethylene glycoxides (that enhance the reduction of the transition metal) are not formed.

The stirring at room-temperature method allowed to obtain Carbon-supported Au:Fe 99.09:0.01, AuCo 99.1:0.9, and Au:Ni 99.5:0.5 nanoalloys, in agreement with Vegard's Law calculations. The materials presented impurities composed of Fe_2O_3 Maghemite, $Co(OH)_2$, and $Ni(OH)_2$, respectively. Despite not having X-ray photoelectron spectra, it can be said that the materials are in alloy form because the main diffraction signal of Au, the family of planes {111}, shifted to higher angles, indicating a contraction in the interplanar distance caused by insertion of smaller atoms (Fe, Co, Ni) into the Au's lattice.

Working in aqueous media, allowed us to obtain smaller and less agglomerated particles than those obtained in ethylene glycol.

In terms of electrocatalytic performance, the materials prepared via EG-stabilization and stirring at room temperature did not carry out the oxygen reduction reaction better than

pure Au/C-HT. Probably because the pressure and temperature conditions of the hydrothermal method, allow to obtain more crystalline materials, with larger active area.

The hydrothermal method allowed to obtain Carbon-supported Au:Fe 99.05:0.05, Au:Co 99.5:0.5, and Au:Ni 99.1:0.9 nanoalloys, according with Vegard's Law calculations. The above is proven by XPS and XRD, since the bind energies of gold shifted to lower values, and the {111} diffraction signal shifted to higher angles. Nevertheless, the obtained nanoalloys have impurities composed by oxidized phases of the transition metals.

Alloying Au with transition metals such as Fe, Co, and Ni by hydrothermal method, improved its catalytic activity towards the oxygen reduction reaction. Which fulfills the hypothesis of this work.

According with Vegard's Law calculations, the reverse micelle microemulsion method allowed to obtain Carbon-supported Au:Ni/C-MO-ap 98.1:1.9 and Au:Ni/C-MO-2h 98.7:1.3 nanoalloys with particle sizes smaller than ethylene glycol-stabilization, stirring at room temperature, and hydrothermal methodologies, as it was seen by TEM.

The reverse micelle microemulsion method allowed to obtain Carbon-supported Au:Ni/C-MO-ap 98.1:1.9 and Au:Ni/C-MO-2h 98.7:1.3 nanoalloys with a higher molar percent of Ni into the Au's lattice than the other methods, the above according with Vegard's Law calculations.

Despite the above, hydrothermal-prepared materials showed better electrocatalytic activity than the reverse microemulsion-prepared ones. Probably because a synergy between electronic changes, particle size and crystallinity.

As perspectives for future work, the synthesis of nanoalloys by hydrothermal method could be proposed, seeking a better control in the composition of metals. Chelating

agents could be used to limit the precipitation of transition metal hydroxides by adjusting the pH to alkaline values. In addition, vary conditions such as reaction time and amount of reducing agent to optimize the co-reduction of both metals.

Another interesting strategy would be the incorporation of carbonaceous supports with electrocatalytic activity such as functionalized graphene oxides, carbon nanofibers, etc.

CHAPTER 5: REFERENCES

International Energy Agency. World Energy Outlook 2017. Recovered on August 20, 2019 from https://www.iea.org/weo2017/

[2] International Energy Agency. World Energy Outlook 2018. Recovered on August 20, 2019 from https://www.iea.org/weo2018/

[3] Bizon, N., & Thounthong, P. (2018). Fuel economy using the global optimization of the Fuel Cell Hybrid Power Systems. *Energy Conversion and Management*, *173*, 665-678.

[4] Shao, M., Chang, Q., Dodelet, J. P., & Chenitz, R. (2016). Recent advances in electrocatalysts for oxygen reduction reaction. *Chemical reviews*, *116*(6), 3594-3657.

[5] Shan, S., Luo, J., Wu, J., Kang, N., Zhao, W., Cronk, H., ... & Zhong, C. J. (2014). Nanoalloy catalysts for electrochemical energy conversion and storage reactions. *RSC Advances*, *4*(80), 42654-42669.

[6] Zhou, Y., Lu, Q., Zhuang, Z., Hutchings, G. S., Kattel, S., Yan, Y., ... & Jiao, F. (2015). Oxygen reduction at very low overpotential on nanoporous Ag catalysts. *Advanced Energy Materials*, *5*(13), 1500149.

[7] Xin, L., Zhang, Z., Wang, Z., Qi, J., & Li, W. (2013). Carbon supported Ag nanoparticles as high performance cathode catalyst for H_2/O_2 anion exchange membrane fuel cell. *Frontiers in chemistry*, *1*, 16.

[8] Ramaswamy, N., & Mukerjee, S. (2012). Fundamental mechanistic understanding of electrocatalysis of oxygen reduction on Pt and non-Pt surfaces: acid versus alkaline media. *Advances in Physical Chemistry*, *2012*.

[9] Yin, J., Shan, S., Ng, M. S., Yang, L., Mott, D., Fang, W., ... & Zhong, C. J. (2013). Catalytic and electrocatalytic oxidation of ethanol over palladium-based nanoalloy catalysts. *Langmuir*, *29*(29), 9249-9258.

[10] Shan, S., Luo, J., Yang, L., & Zhong, C. J. (2014). Nanoalloy catalysts: structural and catalytic properties. *Catalysis Science & Technology*, *4*(10), 3570-3588.

[11] Ferrando, R., Jellinek, J., & Johnston, R. L. (2008). Nanoalloys: from theory to applications of alloy clusters and nanoparticles. *Chemical reviews*, *108*(3), 845-910.

[12] Yin, H. J., Zhou, J. H., & Zhang, Y. W. (2019). Shaping well-defined noble-metal-based nanostructures for fabricating high-performance electrocatalysts: advances and perspectives. *Inorganic Chemistry Frontiers*.

[13] Fernández, J. L., Walsh, D. A., & Bard, A. J. (2005). Thermodynamic guidelines for the design of bimetallic catalysts for oxygen electroreduction and rapid screening by scanning electrochemical microscopy. M− Co (M: Pd, Ag, Au). *Journal of the American Chemical Society*, *127*(1), 357-365.

[14] Qaseem, A., Chen, F., Wu, X., & Johnston, R. L. (2016). Pt-free silver nanoalloy electrocatalysts for oxygen reduction reaction in alkaline media. *Catalysis Science & Technology*, *6*(10), 3317-3340.

[15] Tan, X., Prabhudev, S., Kohandehghan, A., Karpuzov, D., Botton, G. A., & Mitlin, D. (2015). Pt–Au–Co alloy electrocatalysts demonstrating enhanced activity and durability toward the oxygen reduction reaction. *ACS Catalysis*, *5*(3), 1513-1524.

[16] Wang, G., Huang, B., Xiao, L., Ren, Z., Chen, H., Wang, D., ... & Zhuang, L. (2014). Pt skin on AuCu intermetallic substrate: A strategy to maximize Pt utilization for fuel cells. *Journal of the American chemical Society*, *136*(27), 9643-9649.

[17] Park, S. A., Lim, H., & Kim, Y. T. (2015). Enhanced oxygen reduction reaction activity due to electronic effects between Ag and Mn_3O_4 in alkaline media. *ACS Catalysis*, *5*(7), 3995-4002.

[18] Rossmeisl, J., Karlberg, G. S., Jaramillo, T., & Nørskov, J. K. (2009). Steady state oxygen reduction and cyclic voltammetry. *Faraday discussions*, *140*, 337-346.

[19] Hammer, B., & Norskov, J. K. (1995). Why gold is the noblest of all the metals. *Nature*, *376*(6537), 238-240.

[20] Kim, J. H., Chang, S., & Kim, Y. T. (2014). Compressive strain as the main origin of enhanced oxygen reduction reaction activity for Pt electrocatalysts on chromium-doped titania support. *Applied Catalysis B: Environmental*, *158*, 112-118.

[21] Mohanraju, K., & Cindrella, L. (2014). Impact of alloying and lattice strain on ORR activity of Pt and Pd based ternary alloys with Fe and Co for proton exchange membrane fuel cell applications. *RSC Advances*, *4*(23), 11939-11947.

[22] Tang, W., & Henkelman, G. (2009). Charge redistribution in core-shell nanoparticles to promote oxygen reduction. *The Journal of chemical physics*, *130*(19), 194504.

[23] Park, H. Y., Jeon, T. Y., Jang, J. H., Yoo, S. J., Choi, K. H., Jung, N., ... & Sung, Y. E. (2013). Enhancement of oxygen reduction reaction on PtAu nanoparticles via CO induced surface Pt enrichment. *Applied Catalysis B: Environmental*, *129*, 375-381.

[24] Liu, T., Wang, K., Yuan, Q., Shen, Z., Wang, Y., Zhang, Q., & Wang, X. (2017). Monodispersed sub-5.0 nm PtCu nanoalloys as enhanced bifunctional electrocatalysts for oxygen reduction reaction and ethanol oxidation reaction. *Nanoscale*, *9*(9), 2963-2968.

[25] Han, B., Carlton, C. E., Suntivich, J., Xu, Z., & Shao-Horn, Y. (2015). Oxygen reduction activity and stability trends of bimetallic $Pt_{0.5}M_{0.5}$ nanoparticle in acid. *The Journal of Physical Chemistry C*, *119*(8), 3971-3978.

[26] Yan, Z., Wang, M., Liu, J., Liu, R., & Zhao, J. (2014). Glycerol-stabilized $NaBH_4$ reduction at room-temperature for the synthesis of a carbon-supported Pt_xFe alloy with superior oxygen reduction activity for a microbial fuel cell. *Electrochimica Acta*, *141*, 331-339.

[27] Dubau, L., Asset, T., Chattot, R., Bonnaud, C., Vanpeene, V., Nelayah, J., & Maillard, F. (2015). Tuning the performance and the stability of porous hollow PtNi/C nanostructures for the oxygen reduction reaction. *ACS Catalysis*, *5*(9), 5333-5341.

[28] Chung, D. Y., Jun, S. W., Yoon, G., Kwon, S. G., Shin, D. Y., Seo, P., ... & Mun, B. S. (2015). Highly durable and active PtFe nanocatalyst for electrochemical oxygen reduction reaction. *Journal of the American Chemical Society*, *137*(49), 15478-15485.

[29] Chattot, R., Asset, T., Bordet, P., Drnec, J., Dubau, L., & Maillard, F. (2016). Beyond strain and ligand effects: Microstrain-induced enhancement of the oxygen reduction reaction kinetics on various PtNi/C nanostructures. *Acs Catalysis*, *7*(1), 398-408.

[30] Zhang, C., Zhang, R., Li, X., & Chen, W. (2017). PtNi nanocrystals supported on hollow carbon spheres: Enhancing the electrocatalytic performance through high-temperature annealing and electrochemical CO stripping treatments. *ACS applied materials & interfaces*, *9*(35), 29623-29632.

[31] Kumeda, T., Otsuka, N., Tajiri, H., Sakata, O., Hoshi, N., & Nakamura, M. (2017). Interfacial Structure of PtNi Surface Alloy on Pt (111) Electrode for Oxygen Reduction Reaction. *ACS Omega*, *2*(5), 1858-1863.

[32] Yang, K., Jiang, P., Chen, J., & Chen, Q. (2017). Nanoporous PtFe Nanoparticles Supported on N-Doped Porous Carbon Sheets Derived from Metal–Organic Frameworks as Highly Efficient and Durable Oxygen Reduction Reaction Catalysts. *ACS applied materials & interfaces*, *9*(37), 32106-32113.

[33] Wang, S., Xiong, L., Bi, J., Zhang, X., Yang, G., & Yang, S. (2018). Structural and Electronic Stabilization of PtNi Concave Octahedral Nanoparticles by P Doping for Oxygen Reduction Reaction in Alkaline Electrolytes. *ACS applied materials & interfaces*, *10*(32), 27009-27018.

[34] Liu, J., Lan, J., Yang, L., Wang, F., & Yin, J. (2019). PtM (M= Fe, Co, Ni) Bimetallic Nanoclusters as Active, Methanol-Tolerant, and Stable Catalysts toward the Oxygen Reduction Reaction. *ACS Sustainable Chemistry & Engineering*, *7*(7), 6541-6549.

[35] Jha, S., Bhandary, N., Basu, S., & Ingole, P. P. (2019). Electro-deposited Pt_3Co on Carbon Fiber Paper as Nafion-Free Electrode for Enhanced Electro-catalytic Activity toward Oxygen Reduction Reaction. *ACS Applied Energy Materials*, *2*(9), 6269-6279.

[36] He, Y., Wu, Y. L., Zhu, X. X., & Wang, J. N. (2019). Remarkable Improvement of the Catalytic Performance of PtFe Nanoparticles by Structural Ordering and Doping. *ACS applied materials & interfaces*, *11*(12), 11527-11536.

[37] Wang, S., Luo, Q., Zhu., Y.,Tang, S., & Du, Y. (2019). Facile Synthesis of Quaternary Structurally Ordered $L1_2$-$Pt(Fe, Co, Ni)_3$ Nanoparticles with Low Content of Platinum as Efficient Oxygen Reduction Reaction Electrocatalysts. *ACS Omega*.

[38] Bhalothia, D., Fan, Y. J., Huang, T. H., Lin, Z. J., Yang, Y. T., Wang, K. W., & Chen, T. Y. (2019). Local Structural Disorder Enhances the Oxygen Reduction Reaction Activity of Carbon-Supported Low Pt Loading CoPt Nanocatalysts. *The Journal of Physical Chemistry C*, *123*(31), 19013-19021.

[39] Tzorbatzoglou, F., Brouzgou, A., & Tsiakaras, P. (2015). Electrocatalytic activity of Vulcan-XC-72 supported Pd, Rh and PdxRhy toward HOR and ORR. *Applied Catalysis B: Environmental*, *174*, 203-211.

[40] Antolini, E. (2014). Effect of Structural Characteristics of Binary Palladium–Cobalt Fuel Cell Catalysts on the Activity for Oxygen Reduction. *ChemPlusChem*, *79*(6), 765-775.

[41] Yang, R., Bian, W., Strasser, P., & Toney, M. F. (2013). Dealloyed $PdCu_3$ thin film electrocatalysts for oxygen reduction reaction. *Journal of Power Sources*, *222*, 169-176.

[42] Erikson, H., Sarapuu, A., Kozlova, J., Matisen, L., Sammelselg, V., & Tammeveski, K. (2015). Oxygen electroreduction on electrodeposited PdAu nanoalloys. *Electrocatalysis*, *6*(1), 77-85.

[43] Slanac, D. A., Hardin, W. G., Johnston, K. P., & Stevenson, K. J. (2012). Atomic ensemble and electronic effects in Ag-rich AgPd nanoalloy catalysts for oxygen reduction in alkaline media. *Journal of the American Chemical Society*, *134*(23), 9812-9819.

[44] Liu, L., Samjeske, G., Nagamatsu, S. I., Sekizawa, O., Nagasawa, K., Takao, S., ... & Iwasawa, Y. (2014). Dependences of the oxygen reduction reaction activity of Pd–Co/C and Pd–Ni/C alloy electrocatalysts on the nanoparticle size and lattice constant. *Topics in Catalysis*, *57*(6-9), 595-606.

[45] Wu, J., Shan, S., Luo, J., Joseph, P., Petkov, V., & Zhong, C. J. (2015). PdCu nanoalloy electrocatalysts in oxygen reduction reaction: role of composition and phase state in catalytic synergy. *ACS applied materials & interfaces*, *7*(46), 25906-25913.

[46] Holade, Y., da Silva, R. G., Servat, K., Napporn, T. W., Canaff, C., de Andrade, A. R., & Kokoh, K. B. (2016). Facile synthesis of highly active and durable PdM/C (M=

Fe, Mn) nanocatalysts for the oxygen reduction reaction in an alkaline medium. *Journal of Materials Chemistry A*, *4*(21), 8337-8349.

[47] Zeid, E. A., & Ibrahem, I. A. (2017). Preparation, characterization and electrocatalytic activity for oxygen reduction reaction in PEMFCs of bimetallic PdNi nanoalloy. *Materials for Renewable and Sustainable Energy*, *6*(4), 19.

[48] Zhang, Z., Liu, S., Tian, X., Wang, J., Xu, P., Xiao, F., & Wang, S. (2017). Facile synthesis of N-doped porous carbon encapsulated bimetallic PdCo as a highly active and durable electrocatalyst for oxygen reduction and ethanol oxidation. *Journal of Materials Chemistry A*, *5*(22), 10876-10884.

[49] Ellert, O. G. G., Tsodikov, M. V., Nikolaev, S. A., & Novotortsev, V. M. (2014). Bimetallic nanoalloys in heterogeneous catalysis of industrially important reactions: synergistic effects and structural organization of active components. *Russian Chemical Reviews*, *83*(8), 718.

[50] Dai, Y., Wang, Y., Liu, B., & Yang, Y. (2015). Metallic nanocatalysis: an accelerating seamless integration with nanotechnology. *Small*, *11*(3), 268-289.

[51] Hu, P., Song, Y., Chen, L., & Chen, S. (2015). Electrocatalytic activity of alkyne-functionalized AgAu alloy nanoparticles for oxygen reduction in alkaline media. *Nanoscale*, *7*(21), 9627-9636.

[52] Zafferoni, C., Cioncoloni, G., Foresti, M. L., Dei, L., Carretti, E., Vizza, F., ... & Innocenti, M. (2015). Synergy of Cobalt and Silver Microparticles Electrodeposited on Glassy Carbon for the Electrocatalysis of the Oxygen Reduction Reaction: An Electrochemical Investigation. *Molecules*, *20*(8), 14386-14401.

[53] Jiang, R., Tran, D. T., McClure, J. P., & Chu, D. (2015). Nano-Structured Bio-Inorganic Hybrid Material for High Performing Oxygen Reduction Catalyst. *ACS applied materials & interfaces*, *7*(33), 18530-18539.

[54] Song, X., & Zhang, D. (2014). Bimetallic Ag–Ni/C particles as cathode catalyst in AFCs (alkaline fuel cells). *Energy*, *70*, 223-230.

[55] Freakley, S. J., He, Q., Kiely, C. J., & Hutchings, G. J. (2015). Gold catalysis: a reflection on where we are now. *Catalysis Letters*, *145*(1), 71-79.

[56] Zhang, Y., Gao, F., & Fu, M. L. (2018). Composite of Au-Pd nanoalloys/reduced graphene oxide toward catalytic selective organic transformation to fine chemicals. *Chemical Physics Letters*, *691*, 61-67.

[57] Ganesh, P. A., & Jeyakumar, D. (2014). One pot aqueous synthesis of nanoporous $Au_{85}Pt_{15}$ material with surface bound Pt islands: an efficient methanol tolerant ORR catalyst. *Nanoscale*, *6*(21), 13012-13021.

[58] Joshi, K., & Krishnamurty, S. (2016). Tailoring the structure and electronic properties of platinum and gold–platinum nanocatalysts towards enhanced O_2 activation. *New Journal of Chemistry*, *40*(2), 1336-1346.

[59] Chen, D., Li, J., Cui, P., Liu, H., & Yang, J. (2016). Gold-catalyzed formation of core–shell gold–palladium nanoparticles with palladium shells up to three atomic layers. *Journal of Materials Chemistry A*, *4*(10), 3813-3821.

[60] de Yuso, A. M., Maetz, A., Oumellal, Y., Zlotea, C., Le Meins, J. M., & Ghimbeu, C. M. (2017). Optimization of the synthesis of Pd-Au nanoalloys confined in mesoporous carbonaceous materials. *Journal of colloid and interface science*, *505*, 410-420.

[61] Wang, J., Chen, F., Jin, Y., & Johnston, R. L. (2016). Highly active and stable AuNi dendrites as an electrocatalyst for the oxygen reduction reaction in alkaline media. *Journal of Materials Chemistry A*, *4*(45), 17828-17837.

[62] Wang, J., Chen, F., Jin, Y., Lei, Y., & Johnston, R. L. (2017). One-Pot Synthesis of Dealloyed AuNi Nanodendrite as a Bifunctional Electrocatalyst for Oxygen Reduction and Borohydride Oxidation Reaction. *Advanced Functional Materials*, *27*(23), 1700260.

[63] Gong, H., Lu, S., Strasser, P., & Yang, R. (2018). Highly efficient AuNi-Cu_2O electrocatalysts for the oxygen reduction and evolution reactions: Important role of interaction between Au and Ni engineered by leaching of Cu_2O. *Electrochimica Acta*, *283*, 1411-1417.

[64] Wang, J., Chen, F., Jin, Y., & Johnston, R. L. (2018). Gold–Copper Aerogels with Intriguing Surface Electronic Modulation as Highly Active and Stable Electrocatalysts for Oxygen Reduction and Borohydride Oxidation. *ChemSusChem*, *11*(8), 1354-1364.

[65] Kusada, K., Wu, D., Yamamoto, T., Toriyama, T., Matsumura, S., Xie, W., ... & Kitagawa, H. (2019). Emergence of high ORR activity through controlling local density-of-states by alloying immiscible Au and Ir. *Chemical science*, *10*(3), 652-656.

[66] Ly, A., Asset, T., & Atanassov, P. (2020). Integrating nanostructured Pt-based electrocatalysts in proton exchange membrane fuel cells. *Journal of Power Sources*, *478*, 228516

[67] Geukens, I., & De Vos, D. E. (2013). Organic transformations on metal nanoparticles: controlling activity, stability, and recyclability by support and solvent interactions. *Langmuir*, *29*(10), 3170-3178.

[68] Liu, X. Y., Wang, A., Zhang, T., & Mou, C. Y. (2013). Catalysis by gold: New insights into the support effect. *Nano Today*, *8*(4), 403-416.

[69] Vinayan, B. P., & Ramaprabhu, S. (2013). Platinum–TM (TM= Fe, Co) alloy nanoparticles dispersed nitrogen doped (reduced graphene oxide-multiwalled carbon nanotube) hybrid structure cathode electrocatalysts for high performance PEMFC applications. *Nanoscale*, *5*(11), 5109-5118.

[70] Yuan, L., Jiang, L., Liu, J., Xia, Z., Wang, S., & Sun, G. (2014). Facile synthesis of silver nanoparticles supported on three-dimensional graphene oxide/carbon black composite and its application for oxygen reduction reaction. *Electrochimica Acta*, *135*, 168-174.

[71] Bhat, S. A., Rashid, N., Rather, M. A., Pandit, S. A., Rather, G. M., Ingole, P. P., & Bhat, M. A. (2018). PdAg Bimetallic Nanoalloy-Decorated Graphene: A Nanohybrid with Unprecedented Electrocatalytic, Catalytic, and Sensing Activities. *ACS applied materials & interfaces*, *10*(19), 16376-16389.

[72] Matsumoto, T., Takahashi, K., Kitagishi, K., Shinoda, K., Huaman, J. L. C., Piquemal, J. Y., & Jeyadevan, B. (2015). Dissolution and reduction of cobalt ions in the polyol process using ethylene glycol: Identification of the active species and its role. *New Journal of Chemistry*, *39*(6), 5008-5018.

[73] Kharissova, O. V., Dias, H. R., Kharisov, B. I., Pérez, B. O., & Pérez, V. M. J. (2013). The greener synthesis of nanoparticles. *Trends in biotechnology*, *31*(4), 240-248

[74] Yan, Z., Wang, M., Liu, J., Liu, R., & Zhao, J. (2014). Glycerol-stabilized $NaBH_4$ reduction at room-temperature for the synthesis of a carbon-supported PtxFe alloy with superior oxygen reduction activity for a microbial fuel cell. *Electrochimica Acta*, *141*, 331-339.

[75] Wang, Y., & Balbuena, P. B. (2005). Design of oxygen reduction bimetallic catalysts: ab-initio-derived thermodynamic guidelines. *The Journal of Physical Chemistry B*, *109*(40), 18902-18906.

[76] Han, B., Carlton, C. E., Suntivich, J., Xu, Z., & Shao-Horn, Y. (2015). Oxygen reduction activity and stability trends of bimetallic $Pt_{0.5}M_{0.5}$ nanoparticle in acid. *The Journal of Physical Chemistry C*, *119*(8), 3971-3978.

[77] Naveen, M. H., Gurudatt, N. G., Noh, H. B., & Shim, Y. B. (2016). Dealloyed AuNi dendrite anchored on a functionalized conducting polymer for improved catalytic oxygen reduction and hydrogen peroxide sensing in living cells. *Advanced Functional Materials*, *26*(10), 1590-1601.

[78] Li, X. R., Li, X. L., Xu, M. C., Xu, J. J., & Chen, H. Y. (2014). Gold nanodendrities on graphene oxide nanosheets for oxygen reduction reaction. *Journal of Materials Chemistry A*, *2*(6), 1697-1703.

[79] Duan, H., & Xu, C. (2016). Nanoporous PdCr alloys as highly active electrocatalysts for oxygen reduction reaction. *Physical Chemistry Chemical Physics*, *18*(5), 4166-4173.

[80] Wang, G., Xiao, L., Huang, B., Ren, Z., Tang, X., Zhuang, L., & Lu, J. (2012). AuCu intermetallic nanoparticles: surfactant-free synthesis and novel electrochemistry. *Journal of Materials Chemistry*, *22*(31), 15769-15774.

[81] Yang, T., de Almeida, C. M. R., Ramasamy, D., & Loureiro, F. J. A. (2014). A detailed study of Au–Ni bimetal synthesized by the phase separation mechanism for the cathode of low-temperature solid oxide fuel cells. *Journal of Power Sources*, *269*, 46-53.

[82] Lima, F. H. B., Zhang, J., Shao, M. H., Sasaki, K., Vukmirovic, M. B., Ticianelli, A. E., & Adzic, R. R. (2007). Catalytic activity− d-band center correlation for the O_2

reduction reaction on platinum in alkaline solutions. *The Journal of Physical Chemistry C*, *111*(1), 404-410.

[83] Wu, X., Chen, F., Zhang, N., Lei, Y., Jin, Y., Qaseem, A., & Johnston, R. L. (2017). Activity trends of binary silver alloy nanocatalysts for oxygen reduction reaction in alkaline media. *Small*, *13*(15), 1603387.

[84] Darezereshki, E. (2010). Synthesis of maghemite (γ-Fe_2O_3) nanoparticles by wet chemical method at room temperature. *Materials Letters*, *64*(13), 1471-1472.

[85] Darezereshki, E., Ranjbar, M., & Bakhtiari, F. (2010). One-step synthesis of maghemite (γ-Fe_2O_3) nano-particles by wet chemical method. *Journal of Alloys and Compounds*, *502*(1), 257-260.

[86] Blais, J. F., Djedidi, Z., Cheikh, R. B., Tyagi, R. D., & Mercier, G. (2008). Metals precipitation from effluents. *Practice Periodical of Hazardous, Toxic, and Radioactive Waste Management*, *12*(3), 135-149.

[87] Pepperhoff, W., & Acet, M. (2013). *Constitution and Magnetism of Iron and its Alloys*. Springer Science & Business Media.

[88] BioLogic (2020). Koutecky-Levich analysis: the principles. Got from: https://www.biologic.net/topics/rotating-disk-electrode-how-does-the-koutecky-levich-analysis-work/

[89] Kim, H., Lee, S., Kim, S., Oh, C., Ryu, J., Kim, J., ... & No, K. (2017). Membrane crystallinity and fuel crossover in direct ethanol fuel cells with Nafion composite membranes containing phosphotungstic acid. *Journal of Materials Science*, *52*(5), 2400-2412.

[90] Xu, X., Li, L., Wang, H., Li, X., & Zhuang, X. (2015). Solution blown sulfonated poly (ether ether ketone) nanofiber–Nafion composite membranes for proton exchange membrane fuel cells. *RSC advances*, *5*(7), 4934-4940.

[91] Miranda, M. A. R., & Sasaki, J. M. (2018). The limit of application of the Scherrer equation. *Acta Crystallographica Section A: Foundations and Advances*, *74*(1), 54-65.

[92] Nørskov, J. K., Rossmeisl, J., Logadottir, A., Lindqvist, L. R. K. J., Kitchin, J. R., Bligaard, T., & Jonsson, H. (2004). Origin of the overpotential for oxygen reduction at a fuel-cell cathode. *The Journal of Physical Chemistry B*, *108*(46), 17886-17892.

[93] Chen, H., Nishijima, M., Wang, G., Khene, S., Zhu, M., Deng, X., ... & He, Q. (2017). The ordered and disordered nano-intermetallic AuCu/C catalysts for the oxygen reduction reaction: The differences of the electrochemical performance. *Journal of the Electrochemical Society*, *164*(14), F1654.

[94] Paulus, U. A., Wokaun, A., Scherer, G. G., Schmidt, T. J., Stamenkovic, V., Markovic, N. 2. M., & Ross, P. N. (2002). Oxygen reduction on high surface area Pt-based alloy catalysts in comparison to well defined smooth bulk alloy electrodes. *Electrochimica Acta*, *47*(22-23), 3787-3798.

[95] Chattot, R., Le Bacq, O., Beermann, V., Kühl, S., Herranz, J., Henning, S., ... & Maillard, F. (2018). Surface distortion as a unifying concept and descriptor in oxygen reduction reaction electrocatalysis. *Nature materials*, *17*(9), 827-833.

[96] Yang, R., Leisch, J., Strasser, P., & Toney, M. F. (2010). Structure of dealloyed PtCu3 thin films and catalytic activity for oxygen reduction. *Chemistry of Materials*, *22*(16), 4712-4720.

[97] Vesborg, P. C., & Jaramillo, T. F. (2012). Addressing the terawatt challenge: scalability in the supply of chemical elements for renewable energy. *Rsc Advances*, *2*(21), 7933-7947.

[98] Kinoshita, K. (1992). *Electrochemical oxygen technology* (Vol. 30). John Wiley & Sons.

[99] Zadick, A., Dubau, L., Sergent, N., Berthome, G., & Chatenet, M. (2015). Huge instability of Pt/C catalysts in alkaline medium. *Acs Catalysis*, *5*(8), 4819-4824.

[100] Lafforgue, C., Zadick, A., Dubau, L., Maillard, F., & Chatenet, M. (2018). Selected Review of the Degradation of Pt and Pd-based Carbon-supported Electrocatalysts for Alkaline Fuel Cells: Towards Mechanisms of Degradation. *Fuel Cells*, *18*(3), 229-238.

[101] Lafforgue, C., Maillard, F., Martin, V., Dubau, L., & Chatenet, M. (2019). Degradation of carbon-supported platinum-group-metal electrocatalysts in alkaline media studied by in situ Fourier transform infrared spectroscopy and identical-location transmission electron microscopy. *ACS Catalysis*, *9*(6), 5613-5622.

[102] Wu, D., Shen, X., Pan, Y., Yao, L., & Peng, Z. (2020). Platinum alloy catalysts for oxygen reduction reaction: advances, challenges and perspectives. *ChemNanoMat*, *6*(1), 32-41.